Hydrogen Embrittlement in the overaged aluminium alloy 7040-T7651

A dissertation submitted to the University of Manchester for the degree of

Master of Science by Research

In the Faculty of Science and Engineering

2020

Gissele E. Mosquera Campaña

School of Materials

Table of Contents

Word Count: 27527

List of Figures

List of Tables

Abbreviations

AA	Aluminium Alloys
AIDE	Adsorption-induced dislocation-emission
BSE	Backscattered Electrons
CAMS	Crack-arrest markings
CLSM	Confocal Laser Scanning Microscopy
DF	Depth from fracture Surface
EAC	Environmental Assisted Cracking
EBSD	Electron Backscatter Diffraction
EDM	Electro-discharge machining
EDS	Energy-Dispersive Spectroscopy
FCC	faced centre cubic
GB	Grain Boundary
GP	Guinier-Preston zones
GPB	Grain Boundary Precipitate
HAC	Hydrogen-Assisted Cracking
HE	Hydrogen Embrittlement
HEDE	Hydrogen-enhanced decohesion
HEE	Hydrogen Environment Embrittlement
HELP	Hydrogen-enhanced localised plasticity
IG	Intergranular
IMP	Inter-Metallic Particles

IPF	Inversed Pole Figures
LME	Liquid-Metal Embrittlement
MVC	Microvoid-Coalescence
PFZ	Precipitate-free zone
RH	Relative Humidity
SCC	Stress Corrosion Cracking
SE	Secondary Electrons
SEM	Scanning Electron Microscope
SSRT	Slow Strain Rate Testing
SSSS	Super Saturated Solid Solution
ST	Short Transverse
STM	Static Testing Machine
TEM	Transmission Electron Microscopy
UTS	Ultimate Tensile Strength
XEDS	X-Ray Energy-Dispersive Spectroscopy

Abstract

Hydrogen Embrittlement in Aluminium 7xxx series alloys
Gissele Mosquera Campaña, MSc. by Research Corrosion and Protection, University of Manchester, 2020

Aluminium alloys 7xxx series are widely used in structural components in the aerospace industry as they have high strength at low densities. However, it is well known that in moist-air environments the material fails at lower strengths, and the fracture surface displays macroscopic brittle features attributed to atomic hydrogen, this is known as hydrogen embrittlement. Although many attempts have been made in previous researches, the mechanisms under which atomic hydrogen weakens the material is still not completely understood. The objective of the present research is to characterize the effects of atomic hydrogen in the microstructure and to correlate surface observations to possible hydrogen embrittlement mechanisms which promote premature failure of aluminium alloys when they are exposed to humid air environments. For this objective, the commercial over-aged aluminium alloy AA7040-T7651, which is a new generation 7xxx series alloy, in the "as-received" conditions has been selected for its high strength associated with a high Zn content. After a careful surface preparation, and controlling the experimental conditions during the study to prevent Intergranular Type-1 EIC initiation followed by series of interrupted slow strain rate tensile tests at different humidity compositions (0%, 50% and 90%RH) and two strain rates (10^{-5} and 10^{-6} /s) to compare the embrittlement degree under different conditions (humidity composition and exposure times). The main techniques provided in-situ, and post-mortem high-resolution scanning electron images and EBSD maps that provided qualitative and quantitative data of the microstructure differences when the humidity levels were varied. It was found that atomic hydrogen: i) play an essential role in the nucleation and propagation of voids and cracks, ii) increased deformation and damage at grain boundaries, iii) produce changes in the morphology of voids and cracks diminishing the roundness and increasing the aspect ratio of features, and iv) fracture initiation sites were identified on the surface, which were associated with featureless grain-boundaries separation. Finally, it was concluded that a hybrid hydrogen embrittlement mechanism is responsible for the failure observed, in which the leading mechanism diffuses atomic hydrogen to grain boundaries, crack tips and zones of high hydrostatic stresses ahead of crack tips (HELP) causing featureless grain-boundaries separation by decohesion (HEDE) which act as initiation sites.

Declaration

No portion of the work referred to in the dissertation has been submitted in support of an application for another degree or qualification of this or any other university or other institute of learning.

Copyright Statement

i. The author of this dissertation (including any appendices and/or schedules to this thesis) owns certain copyright or related rights in it (the "Copyright") and s/he has given The University of Manchester certain rights to use such Copyright, including for administrative purposes.

ii. Copies of this dissertation, either in full or in extracts and whether in hard or electronic copy, may be made **only** in accordance with the Copyright, Designs and Patents Act 1988 (as amended) and regulations issued under it or, where appropriate, in accordance with licensing agreements which the University has from time to time. This page must form part of any such copies made.

iii. The ownership of certain Copyright, patents, designs, trademarks and other intellectual property (the "Intellectual Property") and any reproductions of copyright works in the dissertation, for example graphs and tables ("Reproductions"), which may be described in this dissertation, may not be owned by the author and may be owned by third parties. Such Intellectual Property and Reproductions cannot and must not be made available for use without the prior written permission of the owner(s) of the relevant Intellectual Property and/or Reproductions.

iv. Further information on the conditions under which disclosure publication and commercialisation of this dissertation, the Copyright and any Intellectual Property and/or Reproductions described in it may take place is available in the University IP Policy, in any relevant dissertation restriction declarations deposited in the University Library, The University Library's regulations and in The University's policy on Presentation of Dissertations.

Acknowledgements

I would like to sincerely thank my supervisor Professor Philip Withers for his time, guidance and support throughout the duration of my MSc. Program. A special thanks to my Co-Supervisor Dr Timothy Burnett, for your patience, dedication, and compromised, for sharing his knowledge and experience, for his support and understanding through difficult times.

I would like to acknowledge “La Secretaría de Educación Superior, Ciencia Tecnología e Innovación” (SENESCYT) for being the sponsor entity during my MSc. studies.

I would like to extend my thanks to Albert Smith and Jack Donoghue for all the technical and moral support during my experiments. It was a total pleasure to work with you. Thanks, Xu Xu, Alistair Garner, Visweswara Gudla, Ryan Euesden and Berzah Yavuzyegit for your selfless help. All my gratitude to Kenneth Gyves, Stuart Morse, Patrick Hill and Michael Faulkner for the support and training provided with was crucial for the development of this project. I would like to give a huge thanks to Olwen Richert, who helped and guided me, opening me the doors at all times, far beyond her work, I will always remember your kindness and support.

This is a resistance path and wouldn’t be possible without friends by your side. I am particularly grateful to my friends in the BP lab, Phil, Mohammed, Rob, Dom, Raunak, thanks for the happy moments; you are all awesome people. I love you all. Rafa and David thanks for all your advice, my little Spanish community in the office, you are wonderful friends. Thank you, Yasser for being making good coffee and the best “boss” ever. To my girls Ana, Indah, Rewaa and Ying, my flatmate Fernando and my favourite Chilean José; thanks for lightning my days. A huge thanks to my coffee people: Lucy, Rachael, Nathan, George, Tara, Nat, Miriam I’ll miss you all so much. For my UK-Ecuadorian family (Isa, July y Santi), I feel so lucky to have you in my life thanks for all the love, for everything, for making me feel at home. I’ll always have you in my heart and thoughts.

Finally, this would never be possible without all my family support, thanks mom and dad for your sweetest love, Gabito you know how much I love you, Maqui for pulling my ears and being there for me, Pablito you are a part of my heart and to my boyfriend Diego for supporting me at difficult times. This is for you all.

Chapter 1. Introduction

High Strength aluminium alloys (AA) 7xxx series are widely used in aerospace structural applications due to their high strength/density ratio. Aluminium alloys are cast into ingots and then rolled, forged or extruded, facilitating fracture paths as the grains elongate; the alloy 7040-T7651 receives a formal $\sim 2\%$ stretch at room temperature after its solution heat treated, later the material is quenched and it goes through a final ageing heat treatment. Aged hardening processes are performed in Aluminium alloys 7xxx series to increase the material performance, in which some strength is sacrificed to improve the resistance against stress corrosion cracking and hydrogen embrittlement (Wanhill, Byrnes and Smith, 2001; Sprowls and Brown, 1969). [1, 2]

Hydrogen embrittlement (HE) in high strength aluminium alloys consists in the degradation of the material due to the interaction of atomic hydrogen with the material under humid environments causing premature failures. It has been observed that HE do not occur when aluminium alloys 7xxx series are strained under 'dry' hydrogen gas irrespective of the external pressure. (Speidel and Hyatt, 1972) [3] Hydrogen embrittlement (HE) in aluminium alloys has been the subject of many studies, to understand the detrimental effect it has in high strength materials. First, an early model of SCC is given, in which the separation of grain boundaries in high strength aluminium alloys is caused by hydrogen formation at the surface which then propagates through the interior into the grain boundaries. (Gruhl, 1984) [4] In The 1970s collecting evidence of HE was the primary concern in which the grain boundaries (GB) were identified as the preferential crack path for aluminium alloys. (Montgrain and Swann, 1974; Gangloff, 2003) [5, 6] Later, advanced imaging techniques facilitated the observation of hydrogen bubbles at grain boundaries, suggesting that high strength aluminium alloys are embrittled in moist environments when hydrogen penetrates the GB. (Scamans, 1978) [7]. Different Al-Zn-Mg-Cu compositions and heat treatments were also analysed to determine the most optimum manufacturing process for commercial applications, where copper additions play an important role when the alloys are overaged, decreasing the material susceptibility to HE. (Knight, 2008; Lynch, Knight, Birbilis and Muddle, 2009) [8, 9]

Stress Corrosion Cracking (SCC) and HE failure such as cracks and the fracture path in aluminium alloys 7xxx series are mainly intergranular (IG). The crack growth mechanism for 2xxx and 5xxx series aluminium alloys occurs due to anodic dissolution of grain boundary regions. In the last decade, it was controversial if the crack nucleation and growth in 7xxx series aluminium alloys happened due to Hydrogen assisted (HAC) cracking, anodic dissolution assisted cracking or passive rupture film. Nowadays, it is accepted that high strength aluminium alloys failure occurs due to HAC. However, it is still under debate if a reduction in ductility and embrittlement happens due atomic hydrogen ingress into the alloy microstructure. (Sprowls and Brown, 1969; Rao, et al., 2016) [2, 10] Several attempts have been made to correlate the effects of Stress Corrosion Cracking (SCC), and Hydrogen Embrittlement with the alloys microstructure, features as the relationship of GB precipitates size and spacing, precipitate free zone (PFZ) width and grain boundary segregation, concluding: 1) matrix precipitates play a fundamental role in controlling HE when TG occurs; 2) grain boundary precipitates support IG embrittlement and 3) PFZ width plays a minor role. Then Nguyen determines that to be less susceptible to HE, GB precipitates optimum size for aluminium alloys is 30 nm approximately. (Holroyd, 1990; Albrecht, Bernstein, & Thompson, 1982; Nguyen, Thompson, & Bernstein, 1987) [11, 12, 13]

Hydrogen Embrittlement in aluminium alloys is known to exist when the material is exposed to moist environments, and the grade of material damage increases with the humidity levels independent of the gas composition. (Speidel, 1971) [14] Previous research has established that hydrogen tends to concentrate ahead of cracks in zones of high hydrostatic stresses (Lynch, 2011; Westlake, 1969) [15, 16]. Later, based on fractography observations, it was proposed that solute hydrogen promotes the movement of dislocations, causing localised plasticity close to grain boundaries; therefore the fracture is intergranular, and hydrogen will accumulate ahead of crack tips. (Beachem, 1972; Birnbaum, Robertson, Sofronis and Teter, 1996) [17, 18] Although some research has been done about hydrogen embrittlement in aluminium alloys 7xxx series, there is still controversy on HE mechanisms, hydrogen interactions with the alloy microstructure and the effect HE has in dislocations and slips behaviour.

This project aims to analyse and compare the effects of different humidity levels while applying load in the most susceptible direction of AA 7xxx series at constant slow strain rates and correlate surface observations with the hydrogen embrittlement mechanisms responsible for the materials failure. In the present research, the loading direction employed is along the short transverse axis, as in this direction is easier for the crack to propagate along the grain boundaries, as opposed to historically hydrogen embrittlement studies, in which tests were performed in directions other that the through-thickness direction. Then, understanding, how the material behaves without the presence of hydrogen is fundamental to determine the differences in cracks number, size and shape and how grain orientation, precipitates and other microstructural features may have an impact in the susceptibility of the material when only the variable “relative humidity” is modified.

The analysis of AA alloys without the effects of hydrogen is then one of the main concerns during this study; therefore, processes were very cautious during the metallographic preparation and storage of samples to avoid hydrogen intake. The data analysis consists of different sets of experiments with a combination of quantitative and qualitative approaches, in which stress-strain curves in dry air and different humidity levels for different sample conditions were obtained. Besides, electron backscatter diffraction techniques (EBSD) were acquired, to evaluate grain orientation and microstructure features before and after deformation, as well as secondary electron imaging of the material at fracture surfaces and zones of interest.

The dissertation first gives a literature review (chapter 2) that covers the fundamental concepts of aluminium 7xxx series and hydrogen embrittlement, and some dislocation theory will be taken into account too; it is not the task of this thesis to examine other types of aluminium alloys. Chapter 3 begins by laying out a brief description of techniques used to obtain the data provided to support the present work, follow by (chapter 4) methods used to prepare the samples for experiments and analytical

techniques to characterize the material. Chapter 5 to 7, presents the results and discussion of the tests, in which i) mechanical behaviour (stress-strain curves), ii) microstructure feature changes and iii) fractography surfaces, when the material is exposed to interrupted slow strain tensile tests will be compared at dry air, lab air and high humidity conditions at different strain rates. Finally, the dissertation will culminate with a general discussion, conclusions and future work that summarise the research outcomes highlighting any experiments, which may increase the understanding and knowledge of hydrogen embrittlement in aluminium 7xxx series.

It is hoped that this research will contribute for a deeper understanding of how hydrogen embrittlement affects the degradation of aluminium alloys 7xxx series, and comprehend the interactions with the material microstructure features, for the future development of resistant materials in commercial applications.

Chapter 2.
Literature Review

2.1. Aluminium alloys

Aluminium is an abundant, light material that by itself has low yield strength. To be used in demanding applications and specific environments, a process called solid solution hardening is performed where, elements such as magnesium, zinc and copper are added to improve the mechanical properties. (Polmear, StJohn, Nie, & Qian, 2017; Speidel, 1975) [18-19]

Materials used in structural components for the aerospace industry should be lighter, have good corrosion resistance, low manufacturing cost and durability. (Staley & Liu, 1997) [20] Aluminium alloys are widely used in fuselage, wings, empennage and supporting structures in commercial aircraft. These parts are considered major structural components, and for this reason, aluminium alloys should have excellent mechanical properties such as good resistance to corrosion and stress corrosion cracking (SCC), good fracture toughness, resistance against fatigue, exhibit slow crack growth and high strength. (Starke & Staley, 2011) [21]

2.2. Wrought aluminium alloys

The primary production of aluminium alloys (AA) consists in the production of wrought products where the material is cast into ingots, then rolled into plates, foils or extruded into wires, tubes, rods or wires. (Polmear, StJohn, Nie, & Qian, 2017, 2017) [18]

There are two kinds of wrought alloys: strain hardenable alloys and age-hardenable alloys; the present work focus on age hardenable alloys 7xxx series.

2.3. Aluminium Alloys 7xxx series.

Aluminium alloys 7xxx series play an essential role in the aerospace industry as they offer relatively high strength at a low density. The main alloying elements of AA 7xxx series are zinc, magnesium and copper, which are added during casting. The solution heat treatment process consist of heating the alloy to a certain temperature, followed

by rapid quenching, the quenching rate has significant effects on alloys environment-induced cracking (EIC) susceptibility. Then, the alloy is stretch a formal $\sim 2\ \%$ at room temperature, and finally, go through a heat treatment process called "aged hardening" that improves mechanical and electrochemical properties. (Polmear, StJohn, Nie, & Qian, 2017) [18]

2.3.1. Aluminium 7xxx (Al-Zn-Mg-Cu) microstructure.

2.3.1.1. Work Hardening effects on microstructure

Aluminium alloys first undergo a casting process; then the material is wrought into ingots generating an increase in the material hardness, as precipitates inhibit the movement of slips; this is called "Work Hardening". In Figure 2-1, a 7xxx series AA microstructure displays the effects of rolling in the orientation and shape of the grains, because of this directional deformation mechanical properties may vary with the direction in which the stress is applied. Wrought aluminium alloys are more susceptible along the short transverse direction because the grains acquired an elongated shape along the rolling direction that facilitates the propagation of cracks. A typical aluminium alloy 7xxx series is formed by i) recrystallised grains (defect-free grains with a misorientation higher than 15°), ii) constituent particles which are formed by impurities Fe and Si, size: 5-30 um, volume fraction: 1-5%, and iii) un-recrystallised grains compound by sub-grains with a misorientation lower than 15°. Figure 2-2 shows the typical microstructure of al aluminium 7xxx series alloy and the characteristic "pancake" grain shape. (23, 25).

2.4. Age-hardening.

Aged hardening is the process of strengthening a material, through the precipitation of particles while temperature decreases due to solubility reduction. There are some necessary steps to achieve the desired properties, which will be described as follows: (Polmear, StJohn, Nie, & Qian, 2017) [18]

1) Dissolution of alloying elements at high temperature in a single-phase region.

2) Production of a supersaturated solid solution (SSSS) by rapid quenching in water at room temperature.
3) Precipitation of fine and disperse particles after controlled decomposition of the SSSS by a complex ageing process at specific temperatures during convenient times. (Polmear, StJohn, Nie, & Qian, 2017; Vargel, 2004; Li, et al., 2008; Zang, Zhang, & Dai, 2012) [18, 22-24]

During the last step, particles may precipitate in the subsequent order:

$$SSSS \rightarrow GP\ zones \rightarrow metastable\ \eta'\ phase \rightarrow stable\ \eta\ phase$$ (Li, Hansen, GjØnnes, & Wallenberg, 1999) [25]

When the alloys endure aged- hardening at room temperature, this is called "natural ageing", however, most aluminium alloys required higher temperatures to get the desired properties, and this is called "Artificial Ageing".

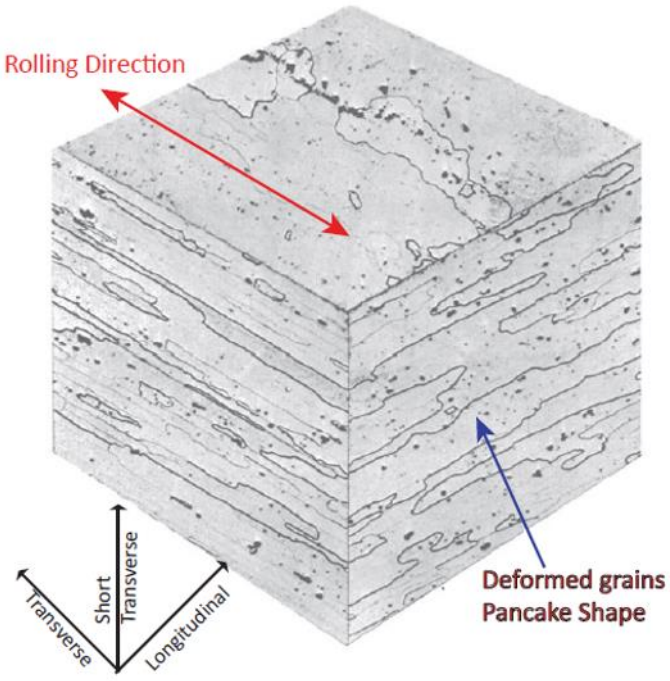

Figure 2-1. Wrought 7xxx alloy showing different orientation and shape of grains in the different directions of a 0.25-in.-thick 7075-T651 plate. (Figure adapted from Speidel, 1975) [19]

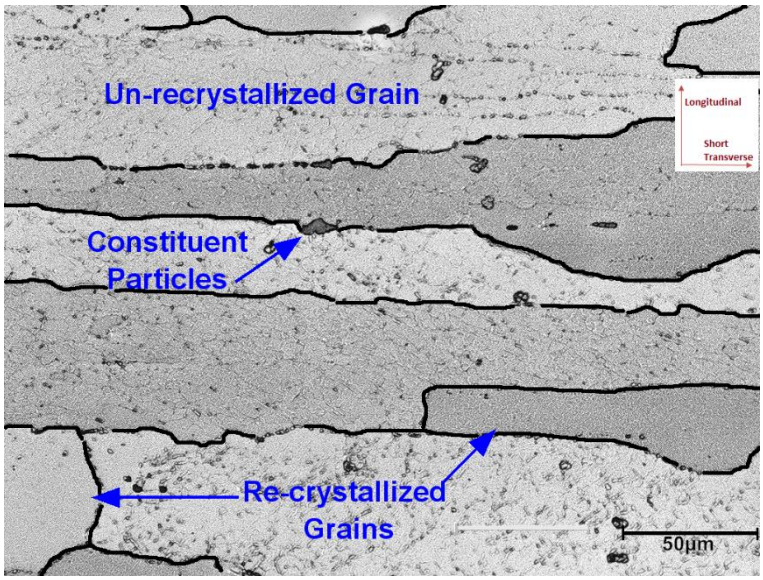

Figure 2-2. Confocal image of Wrought AA 7040-T7651 microstructure indicating the microstructure features in the plane ST-L, the typical "pancake" grain shape may be seen, recrystallised grains and sub-grains from un-recrystallised grains.

2.4.1. Artificial Ageing

Artificial ageing consists on the precipitation of intermetallic compounds as a result of controlled processes, in which variables such as temperature, time and quenching parameters may vary depending on the alloy, to improve properties. Through artificial ageing variations in mechanical, chemical and electrochemical properties may be achieved varying the temperature and time of exposure. (Polmear, StJohn, Nie, & Qian, 2017) [18]

In aluminium alloys 7xxx series (Al-Zn-Mg-Cu), precipitation of Mg(ZnAlCu2) particles occur while ageing; it was noticed that depending on the ageing times, the mechanical properties vary. When the alloy achieves is maximum hardness by artificial ageing, it is known as "peak-aged" which corresponds to the temper T6. However, the materials at this stage are very susceptible to corrosion and stress corrosion cracking (SCC). Then, to obtain maximum performance, the temper T7 called "over-ageing" was developed, in which some tensile strength is sacrificed, improving chemical and electrochemical properties by increasing the resistance against corrosion and SCC; This behaviour may be observed in Figure 2-3. Some aluminium alloys 7xxx series receive a duplex ageing process to provide an adequate resistance against certain types of corrosion while

maximizing the strength, for example, the temper T76 improves the resistance to exfoliation corrosion whilst allowing the maximum tensile strength. (Vargel, 2004; Rometsch, Zhang, & Knight, 2014; Kaufman, 2000) [22, 26, 27]

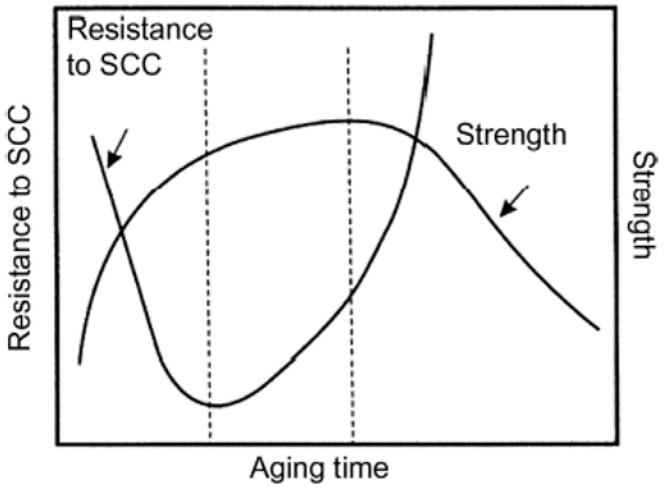

Figure 2-3. Relationship between ageing times and resistance to stress corrosion cracking in aluminium alloys (Speidel, 1975) [19]

2.4.2. Precipitate formation in Aluminium 7xxx series.

Aluminium alloys 7xxx series present the formation of different precipitates during manufacturing stages for commercial application purposes. The precipitates composition and the effects they may have on the material behaviour microstructure is critical to understand how variations in the composition may affect the performance of the different alloys. One example is that some AA 7xxx series alloys show superior SCC resistance compare to others. It has been suggested that Zn: Mg ratio in the range 2.7 - 2.9 is related to a satisfactory resistance against SCC. The effects of the alloying elements in the material properties may be observed in table 2-1. (Polmear, StJohn, Nie, & Qian, 2017; Vargel, 2004; Zhang, & Knight, 2014; Rometsch, Zhang, & Knight, 2014) [18, 22, 24, 26]

Table 2-1. Alloying elements of AA 7xxx Al-Zn-Mg-Cu and their effects in the material properties. (Polmear, StJohn, Nie, & Qian, 2017, 2017) [18]

Alloying element	***Composition (%)***	***Observations***
Cu	2.0 – 2.6 %	- Increase resistance to SCC.
Zr	0.08 – 0.25 %	- Zr precipitate as small insoluble particles of Al_3Zr. - Zr acts as a recrystallization inhibitor. - Zr is less sensible to quenching effects.
Zn: Mg ratio	>2.5	- Ratio related to SCC behaviour.
Impurities: Fe, Si	< 0.1 %	- Contents remain low to obtain good mechanical properties.

Aluminium alloys 7xxx series have a complex microstructure based in different precipitates present at grain boundaries, sub-grains and matrix. The different precipitates are explained as follows:

- Constituent Particles are rich in impurities such as Fe and Si, during rolling these particles are broken and dispersed; regularly their size is between 5-30 μm, and the total volume fraction in AA alloys should be 1 - 5%.
- Dispersoids are critical particles in high strength AA; the composition varies from alloy to alloy, one of the most frequent Al_3Zr. Dispersoids improve their mechanical properties as they reduce grain growth suppressing recrystallization; the total volume fraction is 0.05 -0.2% with particle sizes from 20-500 μm. (Rometsch, Zhang, & Knight, 2014; Liu, et al., 2003; Conserva, Di Russo & Caloni,1971; Thompson, Subramanya, & Levy, 1971) [26, 29, 30, 31]
- Guinier-Preston (GP) zones were discovered in 1938, they are small solute clusters (size >2 nm), which are coherent with the aluminium matrix; for Al-Zn-Mg alloys, GP zones are spherical and contain Mg and Zn. GP zones are the precursors for the latter formation of η' ($MgZn_2$), which is a metastable phase and present a spherical or elongated shape. Later, the stable phase η (MgZ_2) forms, which is incoherent with the matrix. (Guinier, 1938; Sato, 2006; Sha & Cerezo, 2004) (32, 33, 34]

The different precipitate kinds that may be found in an aluminium alloy 7xxx series are shown in figure 2-4 using SEM microscopy.

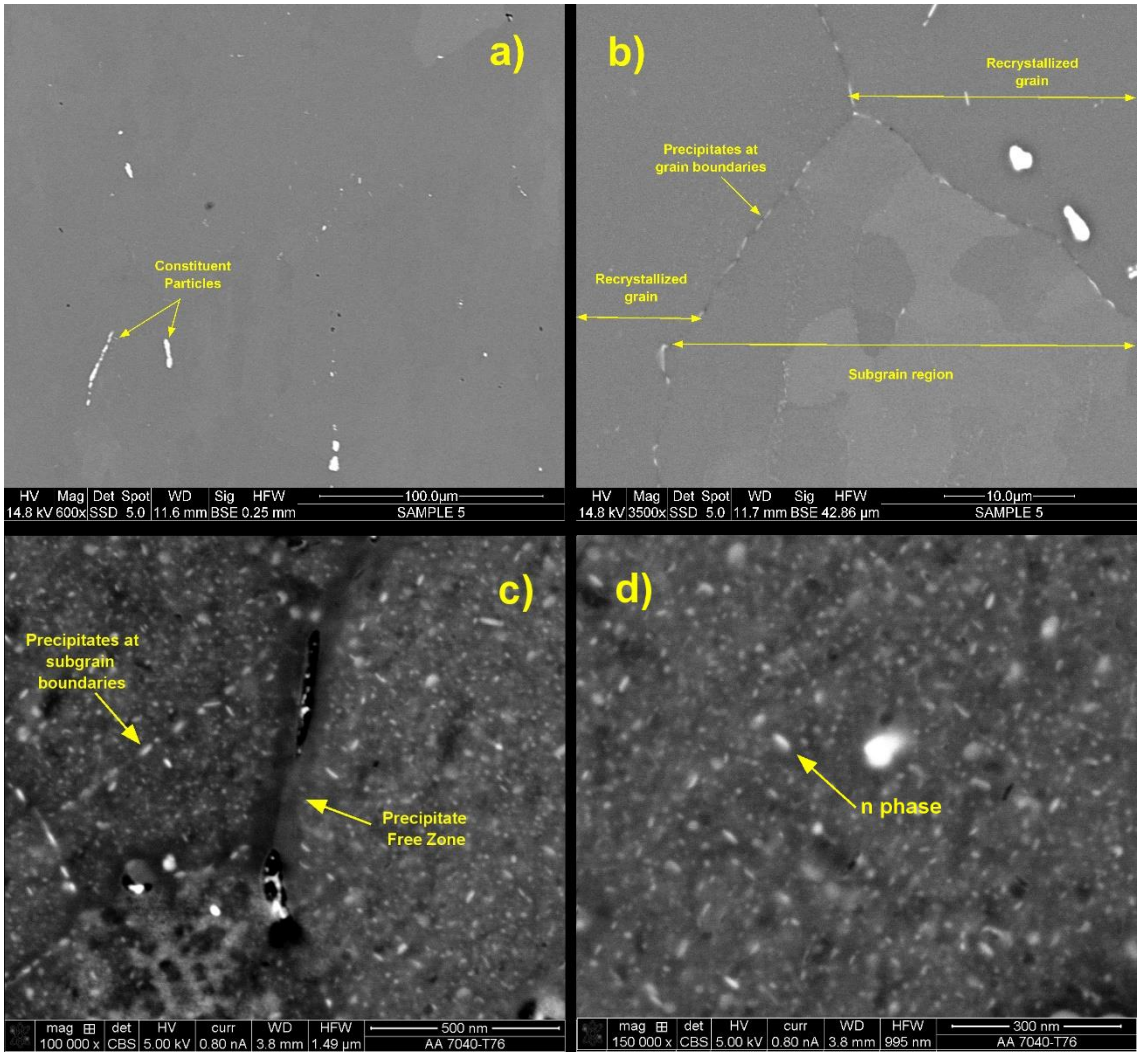

Figure 2-4. SEM images of particle types at an aluminium 7xxx series, AA7040-T7651 a) constituent particles b) precipitates at recrystallized grain boundaries and sub-grain regions c) precipitate Free zone and precipitates at sub-grain boundaries and d) GP zones existing at the alloy matrix. (SEM microscope: FEI Magellan HR FEGSEM)

2.4.3. Precipitate-free zones

Precipitate free zones are narrow areas around the grain boundaries of aluminium alloys, in which there is an absence of precipitates, as displayed in figure 2-5, this happens because solute atoms diffuse to the grain boundaries to form large precipitates. The width of PFZ might change depending on the heat treatment and composition of the alloy. (Nguyen, Thompson & Bernstein, 1987) [13]

PFZ are soft areas where there is a strain localisation, and it was believed that it plays an essential role in the intergranular fracture process; however, despite many attempts, there is no experimental evidence that PFZ may play a fundamental part on embrittlement process. Furthermore, some in situ testing on alloys proves that fracture may happen due to void formation in front of crack tips suggesting that, grain boundaries, precipitates size, and spacing may be critical factors for intergranular fracture processes. (Vasudevan, & Doherty, 1987; Crooks, Kenik, & Starke,1983) [35, 36]

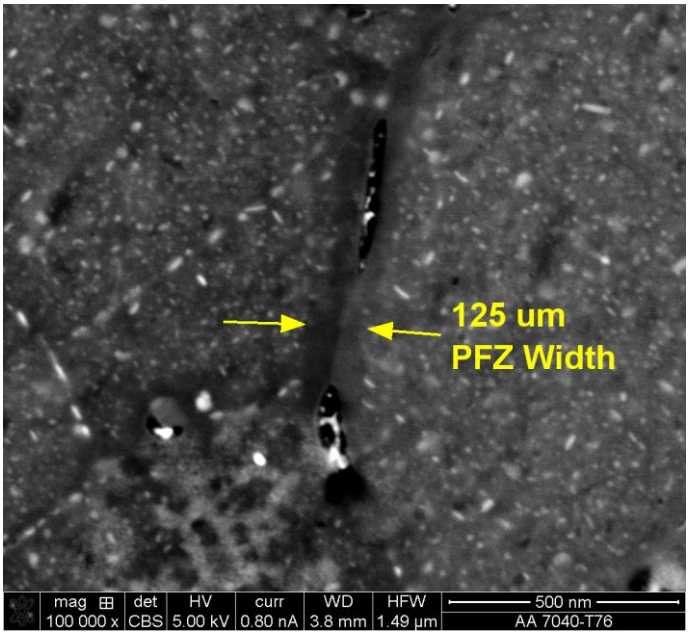

Figure 2-5. Precipitate-free zone width of AA 7040-T7651, SEM images acquired with FEI Magellan HR FEGSEM.

2.4.4. Ageing effects on microstructure.

Aluminium alloys 7xxx series are over-aged to increase the stress corrosion cracking resistance despite a diminution of strength by 15%, such characteristics are attributed to transformations in the grain boundary precipitates microstructure, as the fracture pathway in aluminium 7xxx series is mainly intergranular. Many research has been done to understand this microstructure development, it has been accepted that i) grain boundary precipitates size and spacing increases with ageing, (Knight, 2008) [8] ii) copper content increments at grain boundary precipitates (GBP) (Doig, Flewitt, & Edington, 1977; Ramgopal, Gouma & Frankel, 2002) [37, 38], and iii) GBP are akin in

composition to the η phase with copper additions on it, this behaviour can be seen in figure 2-6, in which for an over-aged alloy copper increases considerably in comparison with the peak-aged GBP compositions. (Goswami, et al., 2013) [39]

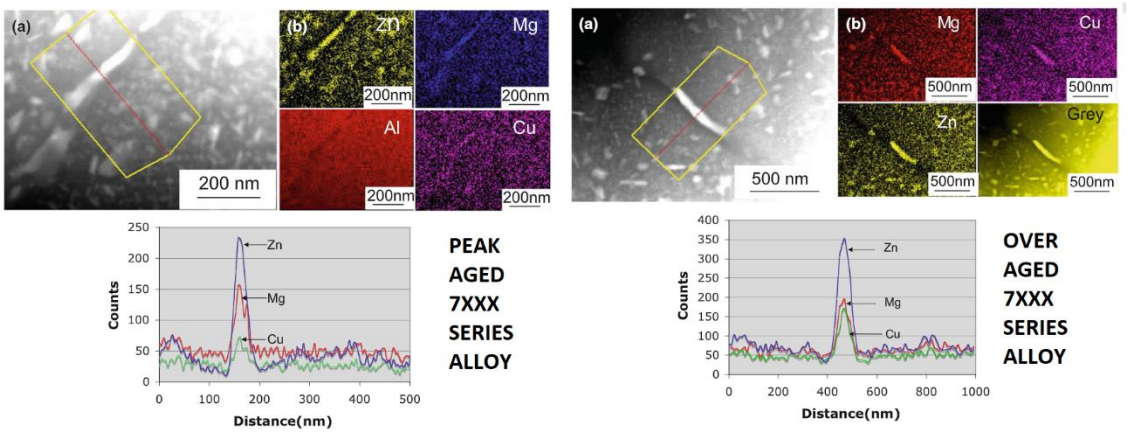

Figure 2-6. Grain boundary precipitates composition in a 7xxx series alloy i) in the left, composition of GBP in a peak-aged alloy with Cu counts below 100; ii) on the right, the composition of an over-aged alloy, where copper counts increase up to 190 counts approx., the changes in precipitates size and spacing is also appreciable. [39]

2.5. Environmental Assisted Cracking (EAC)

Aluminium alloys under liquid-metal, aqueous and hydrogen environments suffer a decrease in the resistance to crack initiation compare with the material properties in inert environments, and this is known generally as environmentally assisted cracking (EAC). Fracture surfaces after being exposed to dry gases show ductile features; however, brittle characteristics are observed when aluminium alloys are exposed to aqueous or moist environments. Figure 2-7 shows the main parameters that affect EAC processes, which are the environment, stress and sensitive materials. When only the environment is changing it has been observed that fracture areas and metallographic features shared similar characteristics for liquid metal embrittlement (LME), stress corrosion cracking (SCC) and hydrogen assisted cracking (HAC); implying that these processes may be affected by the same embrittlement mechanism. (Lynch, 1988) [40]

The similarities in EAC processes are i) distribution of slips around crack tips, ii) dimples, tear ridges and slip lines, iii) crystallographic direction of crack growth, and iv) decrease on strength. It is concluded that for HAC hydrogen atoms weaken the material, in the

same way, metal atoms affect the embrittlement of LME. Hydrogen entry into aluminium under dry conditions is prevented because the hydrogen does not dissociate; therefore, it cannot affect aluminium alloys microstructure. However, in aqueous environments the dissociation of water molecules, when they react with clean aluminium surfaces during the rupture of oxide films, may produce adsorption of hydrogen in crack tips. (Lynch, 1986; Lynch, 1982) [41, 42]

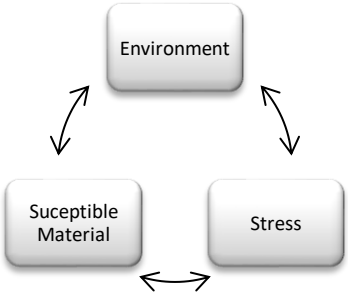

Figure 2-7. Environmentally assisted cracking (EAC) parameters that are responsible for the embrittlement of certain materials.

2.6. Hydrogen Embrittlement (HE)

Some decades before, it was believed that high strength aluminium alloys weren't affected by hydrogen embrittlement, because hydrogen diffusion in face centre cubic (fcc) crystalline structures was meagre. Aluminium alloys were tested in dry environments the fracture surfaces did not display any signs of embrittlement and the stress-strain curves do not display early failure or lower mechanical properties. However, there is evidence showing how under slow strain rates and moist environments aluminium alloys present macroscopic brittle fracture characteristics, although at high-resolution imaging it presents shallower dimples and the strength resistance to cracking decreases; then it was suggested that the adsorption of hydrogen atoms at crack tips weakens aluminium alloys microstructure. To date, several studies have been done to understand the mechanisms under which this embrittlement takes place and how they affect the alloy microstructure and the mechanical properties. (Albrecht, Bernstein, & Thompson, 1982; Nguyen, Thompson, & Bernstein, 1987, Beachem, 1972; Johnson, 1973; Scamans, 1982; Albrecht, Thompson & Bernstein, 1979; Thompson & Bernstein, 1980) [12, 13, 16, 43, 45, 47, 48]

2.6.1. Effects of solute hydrogen on dislocation activity

The effects of hydrogen in the dislocation activity have been obtained through comparisons between hydrogen-free and hydrogen charged materials when exposed to mechanical testing; some important effects are:

- The stress-strain relationship during tensile tests is dependent on many variables such as temperature, strain rate and the material type.
- Slip lines changes in height, spacing and the number of active slip systems may be characterized by scanning electron microscopy (SEM) analysis.
- Dislocations behaviour observed through transmission electron microscopy (TEM) in thin foils shows that dislocations become mobile increasing their speed, and dislocations generation from sources may increment. (Lynch, 2012; Robertson et al., 2015) [45, 46]

2.6.2. Determining the effects of adsorbed hydrogen on surfaces

Adsorbed hydrogen diffuses into the bulk to zones of high hydrostatic stress in front of cracks. Voids can nucleate at slip band interceptions and around second phase particles; then in high strength aluminium alloys exposed to moist air environments, it has been observed that cracking occurs along grain boundaries and around grain-boundary precipitate/matrix interfaces. (Lynch, 2012) [45]

2.6.3. Hydrogen Embrittlement Mechanism

Many pieces of research have been done to understand how atomic hydrogen interacts with material's microstructure. Some of the proposed mechanisms are:

- Hydride Embrittlement
- Hydrogen-enhanced decohesion (HEDE)
- Adsorption-induced dislocation-emission (AIDE)
- Hydrogen-enhanced localised plasticity (HELP)
- Hybrid Mechanism and Vacancy role.

2.6.3.1. Hydride Embrittlement

Hydride Embrittlement consists in the continuous formation and fracture of hydrides at the crack tips following the sequence: i) hydrogen diffuses to regions of high hydrostatic stress ahead of crack tips, ii) hydride nucleation and fracture, and iii) crack arrest at the hydride-matrix interface, as can be seen in figure 2-8. This mechanism is hard to analyse after fracture, as hydrides may dissolve in the absence of high hydrostatic stresses. (Ciaraldi, et all. , 2011) [49]

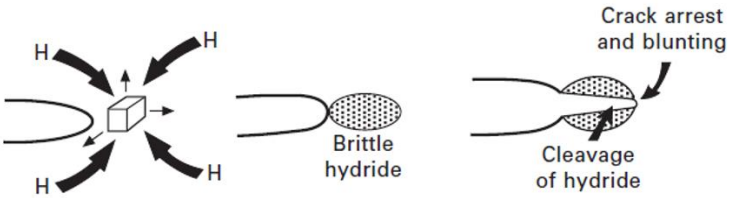

Figure 2-8. Hydride embrittlement mechanism illustration by diffusion of hydrogen to high hydrostatic stress zones, hydride formation, fracture and arrest. [16]

2.6.3.2. Hydrogen-enhanced decohesion (HEDE)

Hydrogen is believed to weaken interatomic bonds, producing tensile separations of atoms instead of slip. The evidence for the existence of this mechanism is "featureless" IG cracking, when imaging using SEM, but this is still debatable, as other techniques may resolve small shallow dimples on apparent flat surfaces; (Troiano, 1960; Lynch, 2011) [50, 15] figure 2-9 illustrates how HEDE mechanism works.

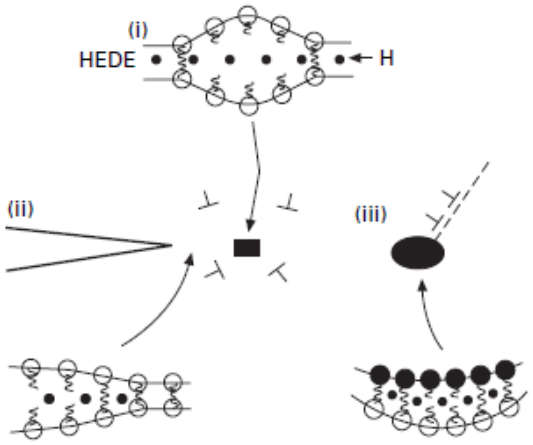

Figure 2-9. Illustration of HEDE mechanism where interatomic bonds are weakened by i) hydrogen lattice ii) adsorbed hydrogen iii) hydrogen at particle-matrix interfaces. [15]

2.6.3.3. Hydrogen-Enhanced Localised Plasticity (HELP)

Beachen (1972) [16] suggested that solute hydrogen facilitates the movement of dislocations, then Hydrogen-Enhanced Localised Plasticity (HELP), as can be observed in figure 2-10, makes slips easier resulting in higher deformation due to embrittlement. (Scully, 2012) [51] The presence of hydrogen in front of crack tips is fundamental for HELP mechanism to happen, and it is believed that a sub-critical crack growth may occur by a more localised microvoid-coalescence (MVC) process than in inert environments. (Lynch, 2011) [15]

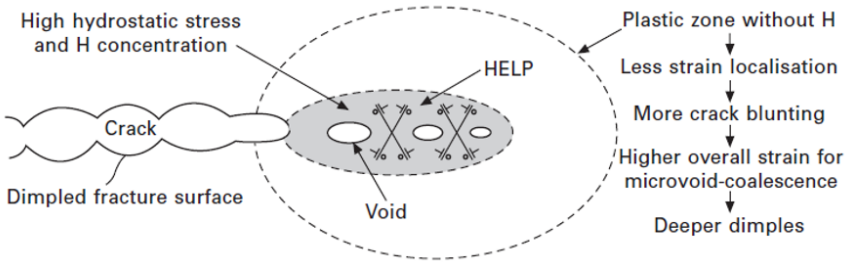

Figure 2-10. Illustration of HELP mechanism where localised plasticity promotes microvoid-coalescence in high hydrogen concentration areas ahead of crack tips. [15]

HELP mechanism is a function of the strain velocity and temperature because hydrogen moves with dislocations and the presence of hydrogen increase dislocation pile up at grain boundaries (Robertson, et al., 2015) [46]. Further research needs to be done to understand how hydrogen may promote the nucleation of dislocations. (Lynch, 2011) [15]

2.6.3.4. Adsorption-induced dislocation-emission (AIDE)

AIDE mechanism consists of dislocations nucleation at second-phase particles, slip bands intersections or other sites in the plastic zone. When atomic hydrogen is adsorbed, and it causes the emission of dislocations away from crack tips due to high stresses. Crack growth by AIDE also requires the nucleation and growth of micro or nanovoids ahead of crack tips as can be seen in figure 2-11. (Vehoff, H., Rothe, W., 1986) [52]

AIDE mechanism is expected to produce a cleavage-like cracking surface with nanoscale dimples and localised slip planes that intersect the crack tip; this mechanism presents shallower dimples than non-embrittled materials. AIDE is also consistent with a dimple intergranular fracture, in which crack growth in embrittled materials occur because hydrogen adsorption weakens the interatomic bonds; promoting the egress of dislocations from crack tips, as slip bands contribute to crack opening. (Lynch, 2011) [15]

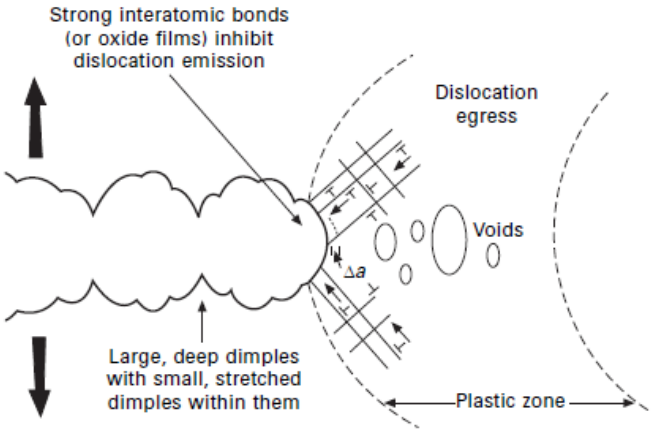

Figure 2-11. Illustration of AIDE mechanism that consists of ductile crack growth by coalescence of voids and egress of dislocations. [15]

2.6.3.5. Hybrid Mechanism and Vacancy role.

More than one HE mechanism may promote crack growth, AIDE may promote crack growth by void nucleation ahead of cracks and slip band intersections at particle-matrix interfaces can be caused by HELP or HEDE, the way hybrid mechanisms work can be seen in figure 2.12. Vacancies play an essential role in crack growth as they can agglomerate in from of crack tips leading to nanovoid formation, then possibly facilitating dislocation climb and cross-slip, reducing strain hardening. (Lynch, 2011) [15]

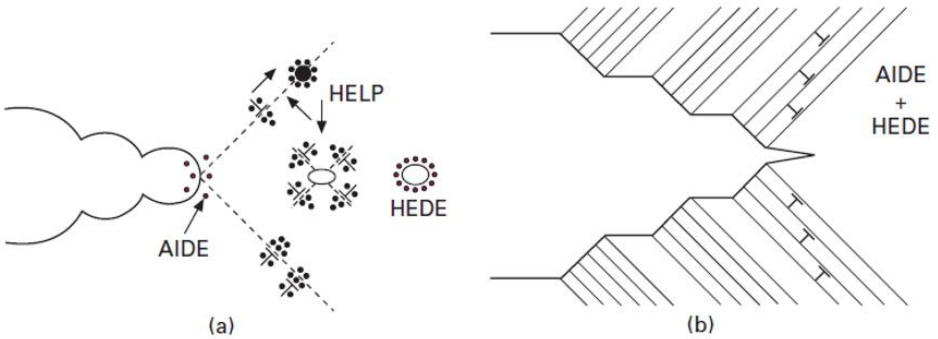

Figure 2-12. Hybrid mechanism illustration showing a) AIDE crack growth with HELP or HEDE facilitating void coalescence and b) AIDE with HEDE alternation. [15]

2.6.4. Hydrogen Embrittlement in Aluminium alloys

Aluminium alloys are susceptible to hydrogen embrittlement when they are exposed to aqueous environments, water vapour saturated air, and water vapour mixed with other gases. Hydrogen adsorption does not occur in the presence of dry hydrogen gas, and it happens when atomic hydrogen is produced by water dissociation on the alloy surface. (Lynch, 2011) [15]

2.6.4.1. Hydrogen interaction in aluminium systems

2.6.4.1.1. Hydrogen surface interactions and adsorption

Aluminium alloys are protected against chemisorption of dihydrogen due to a protective oxide layer, which thickness depends on the reaction rate with oxygen. However, when water vapour gets in contact with the alloy, aluminium produces aluminium oxide and hydrogen atoms, as shown in the following half-cell reaction:

$$2Al + 3H_2O \rightarrow Al_2O_3 + 6H^+ + 6e^- \qquad \text{Eq. [2.1]}$$

Then, the water dissociates in chemisorbed atomic hydrogen H(c), which later may be absorbed by the metal lattice becoming very detrimental for high strength aluminium alloys. (Scully, 2012) [51]

2.7. Dislocation Theory

This section will focus on explaining the fundaments of basic dislocation theory for high strength aluminium alloys.

2.7.1. Dislocations

In aged-hardened aluminium alloys precipitates play a fundamental role in the strengthening of materials acting as obstacles for the movement of dislocations. As there is slip mismatch between grains, dislocations cannot jump from one grain to the

other piling up against grain boundaries, requiring higher stresses to promote slips crossing beyond the boundaries, second phase particles size and spacing characteristics play a critical role in this process. Figure 2-13 displays how some dislocations move around precipitates leaving a loop around them; this is known as Orowan mechanism; the separation between particles determine the stress required to achieve the movement of dislocations. (Roylance, 2001)[53] (Scattergood, Bacon, 1975; Smallman, 2016) [54, 55]

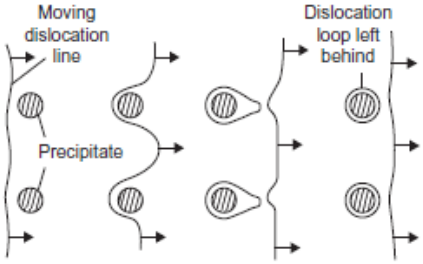

Figure 2-13. Illustration of a dislocation moving through precipitates using the Orowan mechanism where dislocations left loops around particles as they pass. [55]

2.7.2. Slip lines

Slip lines look as irregular steps in the fracture surface; slips are caused by shearing-off layers of material. In figure 2-14 slips on aluminium alloy may be seen, (Broek, 1974)[56] aluminium alloys have a faced centre cubic crystal structure; for this reason, it has 12 slip systems, slip occurs mainly on closed packed {111} planes along <110> closed packed directions. (Jackson, 2012) [57]

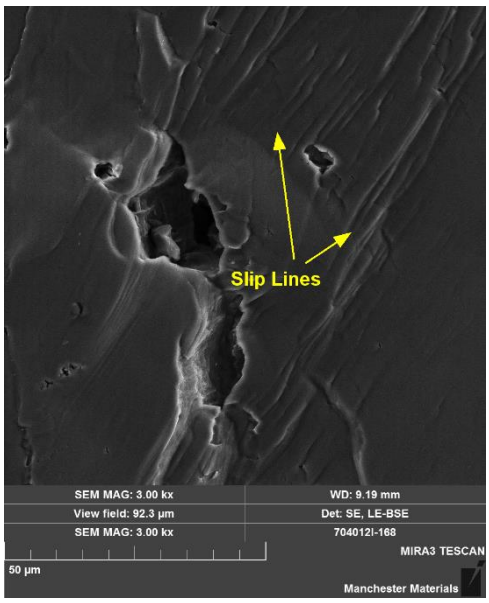

Figure 2-14. Slips lines in Aluminium 7040-T7651 after exposure to moist air environments during tensile testing.

2.7.3. Intergranular misorientation and grain breakup

Cubic crystal structures like aluminium and magnesium suffer deformation heterogeneity, figure 2-15 shows how a grain breaks into sub-regions due to i) changes in the slip direction, ii) the number of slip bands, and iii) slip intensity. Next, deformation bands break the grains into regions of different orientations separated by boundaries of high lattice curvature. (Hughes, 1997; Orozco, et al., 2017) [57, 59]

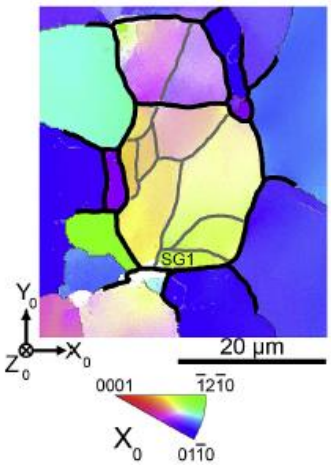

Figure 2-15. Grains in magnesium showing sub-regions within grains with different orientations. [59]

2.7.4. Enhanced grain boundary shear

Certain grain boundaries show higher shear strain levels; this has been observed in measurements acquired in magnesium alloys that confirm that these high strains are not caused by grain boundary cracking or sliding in grain boundary planes. Instead, enhanced slip is believed to occur in regions near-certain grain boundaries where there is enhanced slip. It has been suggested that this localised slip is caused by deformation incompatibility at the grain boundaries, implying it only happens between grains that have different basal slip activities. (Orozco, et al., 2017) [59]

2.7.5. Taylor Factor (M)

Taylor Factor (M) is used to express an average orientation of grains in a polycrystal; it is highly dependent on the material texture and the crystallographic orientation. (Lebensohn & Tomé, 1993; Kocks, Tomé & Wenk, 1998) [60, 61] Some void nucleation theories have been performed through Taylor factor analysis. Voids seem to occur preferentially in zones of contrasting hard (high M) and soft (low M) orientations, as they display a very heterogeneous deformation than in hard orientations regions and between grain boundaries with soft orientations (low M). (Bieler, Semiatin; 2002) [62].

2.7.6. Schmid's Law

The Schmid's law states that slip begins when the shear stress reaches a critical value an overcomes the dislocation motion reaching a critical value known as critical resolved shear stress (CRSS). The preferential slip system may be the one with the highest Schmid factor (m), which is dependent on the crystal lattice orientation with the loading axis. The material is weaker (soft orientation) when the slip plane and the loading axis are at 45 degrees (m=0.5). In comparison, a hard orientation (strong material) happens when the angle between the slip plane and the tensile loading axis is 90 or 0 degrees (m=0). (Schmid & Boas, 1950; Hosford, 2010) [63, 64]

2.8. Fractography Analysis

One method to analyse HE is applying loads in environments that may cause embrittlement of materials; to afterwards observed the fracture surface looking for signs of embrittlement, effects on the metallography, and to correlate this with the HE possible mechanisms. It is vital to notice that different environmental conditions or strain rates may cause different characteristics; then, some fractography theory may be mentioned to understand future work on the present dissertation.

2.8.1. Ductile and brittle fracture characteristics

Metals are generally ductile materials meaning that they may accommodate considerable deformation before material's failure. Alloys may lose some ductility with different alloying elements compositions because precipitates resist the movement of dislocations strengthening the material. It is essential then, to recognise the differences between fracture surfaces characteristics, as brittle materials show a smooth, flat surface with no or little deformation, it is said that the crack propagates through cleavage fracture modes. (UNSW, 2020; Pineau, 2016; Liebowitz, 2018) [65-67] Finally, a ductile fracture present dimples around precipitates, that coincide with the opposite fracture surface, in figure 2-16 the difference between brittle and ductile fracture surfaces can be observed. (Lynch, 2012) [45]

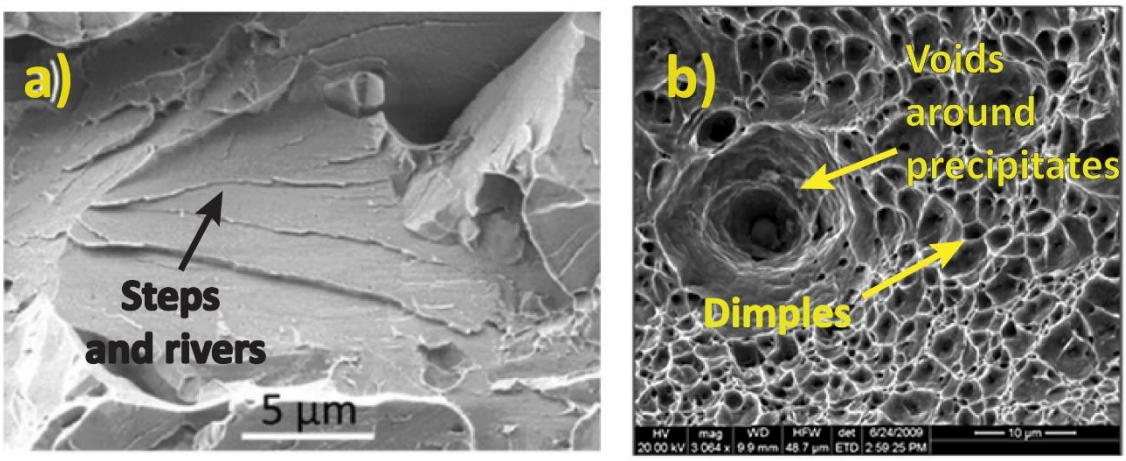

Figure 2-16. Differences between a) characteristic brittle fracture showing steps and rivers with a smooth surface and b) ductile fracture showing dimples and voids around precipitates.

2.8.1.1. Cleavage Fracture

Cleavage fracture happens when a crystal fails along low index crystallographic planes, it is characterised for the lack of plastic deformation and features like river lines and tear ridges (formed when a crack intersect isolated voids ahead of cracks with a characteristic Y-shaped) that point in the direction of crack growth. (Lynch, 2012; Brooks & McGill, 1994; Vehoff & Rothe, 1986) [45, 68, 70]

2.8.1.2. Intergranular Fracture

Some materials like aluminium alloys have an intergranular fracture, in which the crack grows along grain boundaries, IG fractures are characterized by brittle fracture surfaces, displaying tear ridges and cleavage like fractures with the formation of voids around precipitates, as observed in figure 2-17. (Brooks & McGill, 1994) [68]

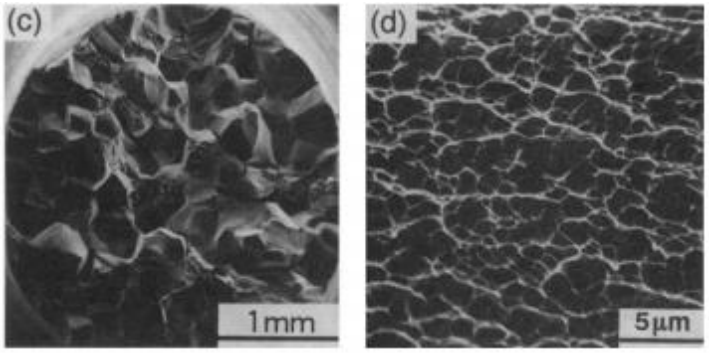

Figure 2-17. Intergranular fracture in aluminium alloys at a high strain rate. (Kuramoto, Itoh & Kanno, 1996) [70]

2.8.1.3. Void Coalescence

Figure 2-18 indicates two void formation mechanisms under the application of tensile loads. First, i) the image on the left happens when voids are formed trapping particles inside, this is called "particle-matrix decohesion", here both sides of the fracture surface are dimpled. On the other hand, ii) the image on the right shows particles surrounded by voids on both sides of the fracture surface this happened when the particles broke (particle cracking); finally, crack growths by void coalescence in both cases. (Brooks & McGill, 1994) [68]

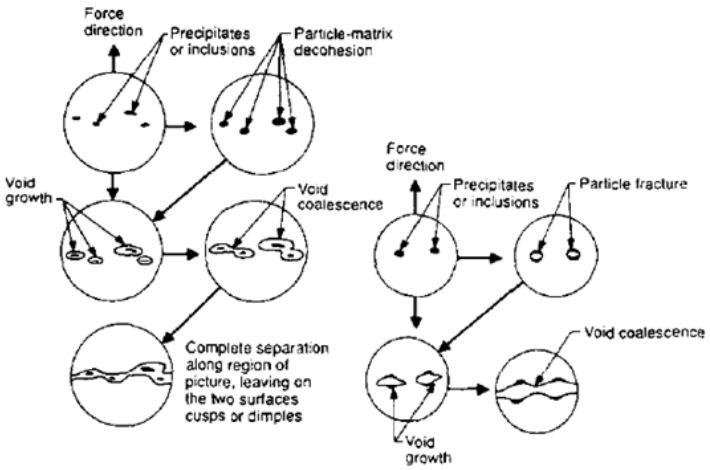

Figure 2-18. Illustration of formation of voids and posterior coalescence due to precipitates by i) particle-matrix decohesion (on the left) and ii) particle cracking (on the right) [68]

2.8.2. Hydrogen embrittlement fractography characteristics.

Deformation influenced by hydrogen may allow materials to deform at lower stresses because hydrogen is believed to increase the dislocations movement speed. There may be an increase in the number of dislocations and the number of dislocations piled up against grain boundaries. (Robertson, et al., 2015) [46]

HELP mechanism states that hydrogen may have an effect on local stresses, but not in the global stresses of the material, may be caused by enhanced plasticity as hydrogen moves to zones ahead of cracks with dislocations. It has been observed that when certain materials are exposed to hydrogen charged environments, the fracture surface has an apparent brittle behaviour, as can be seen in figure 2-19. However, nowadays, small dimples have been observed in these apparent smooth areas with the help of higher resolution imaging techniques. The size of the dimples depends on the aluminium alloy ageing treatment; for instance, over-aged samples have bigger dimples than peak-aged alloys. (Lynch, 1988, Bieler, et al., 2014) [40, 71]

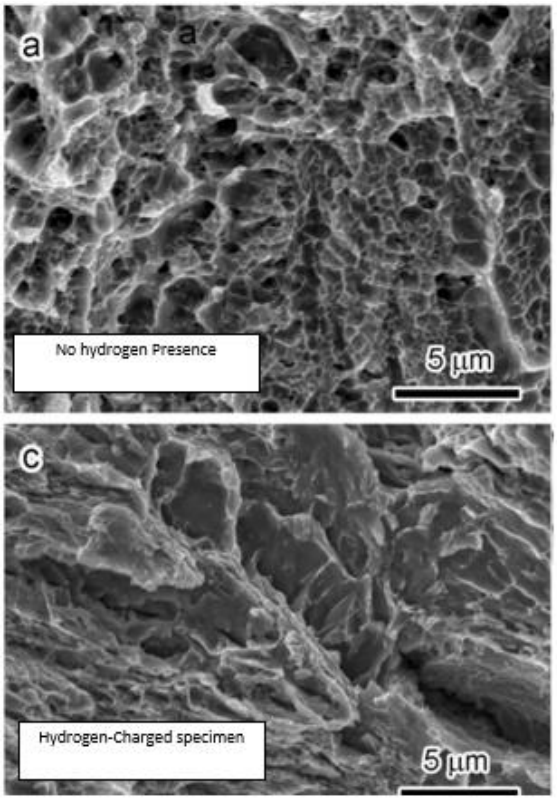

Figure 2-19. Comparison between fracture surfaces of a) no presence of hydrogen specimen and c) hydrogen-charged sample. [40]

2-9. Latest Research in Hydrogen Embrittlement and Aluminium Alloys.

2.9.1. Fracture Types in Hydrogen Environmental Assisted Cracking (HEAC)

Commercial Al-Mg alloys 5XXX series display three different fracture surfaces when exposed to lab air environments during slow strain rate testing (SSRT) of smooth tensile specimens. In figure 2-20, a) fracture "Type-1" occurs close to the edges, it shows a bright, flat and smooth appearance along grain boundaries, this fracture type was never observed when testing in dry air. Afterwards, it is substituted by b) fracture "Type-2" which displays flat areas with high topography between grains, probably due to intermetallic particle clusters which also shows tear-ridges and cleavage-like characteristics. Finally, when the material is closed to failure this fracture type is replaced for c) fracture "Type-3" characterised by a dimpled-ductile surface. It is believed that these surfaces are observed in moist air environments as hydrogen acquires high concentrations at second phase particle interfaces, grain boundaries and dislocations. (Holroyd, et al., 2017) [72]

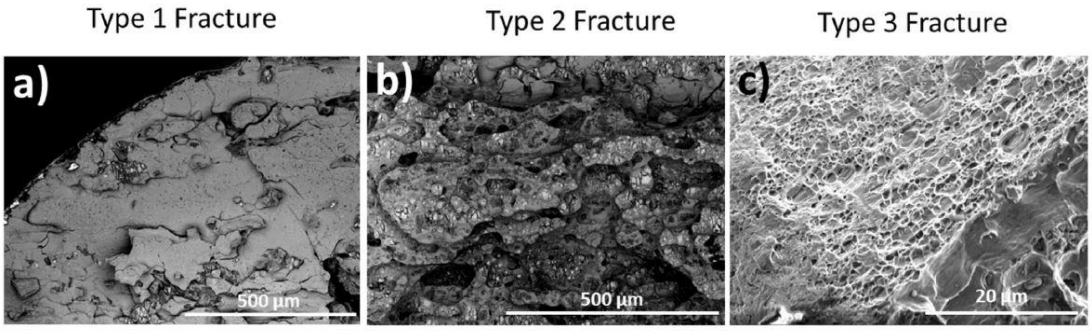

Figure 2-20. Hydrogen Environmental Assisted Cracking fracture surface types, BSE images of a) fracture "type 1", b) fracture "type 2" and c) fracture "type 3". [72]

2.9.2. Hydrogen effects on high Zinc Aluminium alloys 7xxx series.

It has been demonstrated that hydrogen embrittlement susceptibility increases when Zn composition increases. In the last generation of aluminium alloys with higher Zn content when materials are exposed to hydrogen environments, the fracture surface changes from dimpled (characterised by micro-void coalescence) into quasi-cleavage features. Changes can be observed in figure 2-21, in which fracture surfaces of the aluminium alloy 7150 (with induced hydrogen) after tensile testing displays a) a dimpled fracture along the whole fracture surface with an initial 6% Zn content. However, b) when Zn content is increased up to 10 % a brittle surface (flat-featureless) appears close to the edges of the sample, this change in surface features is attributed to a major hydrogen susceptibility. (Bhuiyan, et al., 2016) [73]

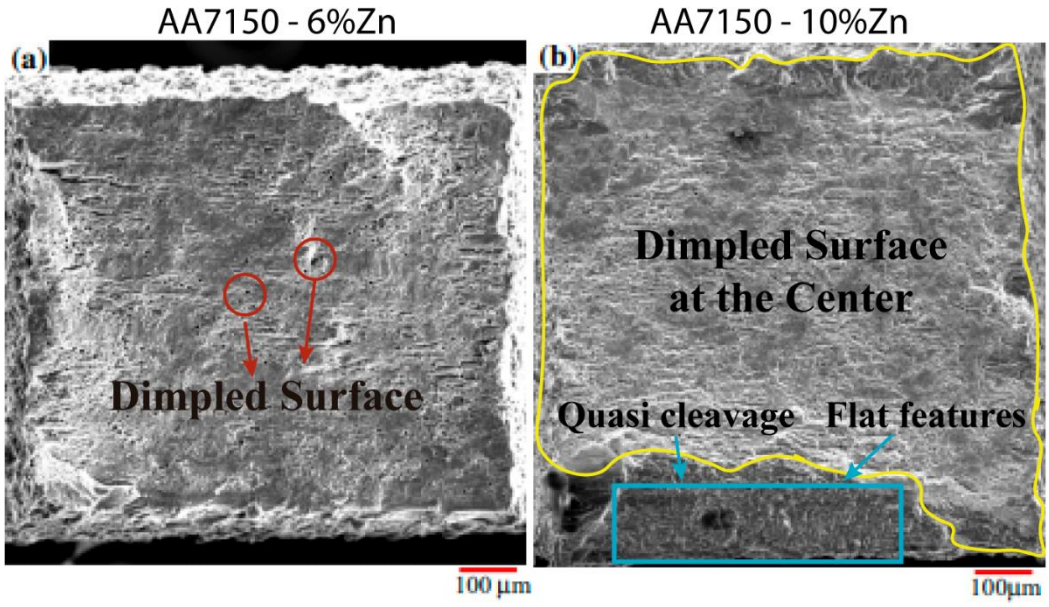

Figure 2-21. Hydrogen-induced 7150 aluminium alloy fracture surface at a) 6% and b) 10% Zn content. [73]

2.9.3. In-situ testing in 7xxx aluminium alloys

In an attempt to understand cracks nucleation and propagation under the effect of moist environments in high Zn-Mg ratio aluminium alloys, 4-point in-situ bend tests were performed in AA7449 and AA7075. After testing samples were polished and imaged; the results are displayed in figure 2-22, in which cracks distribution along the whole specimen demonstrates that: i) cracks grow along grain boundaries in the transverse direction, and ii) sequential polishing steps points that cracks may be larger below the surface. Furthermore, figure 2-23 displays cracks with similar lengths on both alloys; however, it is clear that cracks form at lower stresses in the alloy with the highest Zn/Mg ratio (AA7449), probably because cracks can growth through tortuous paths and to overcome obstacles such as triple junctions and grains oriented 45 degrees, while for the AA7075 the same conditions tend to stop crack growth. (De Francisco, Larrosa & Peel, 2020) [74]

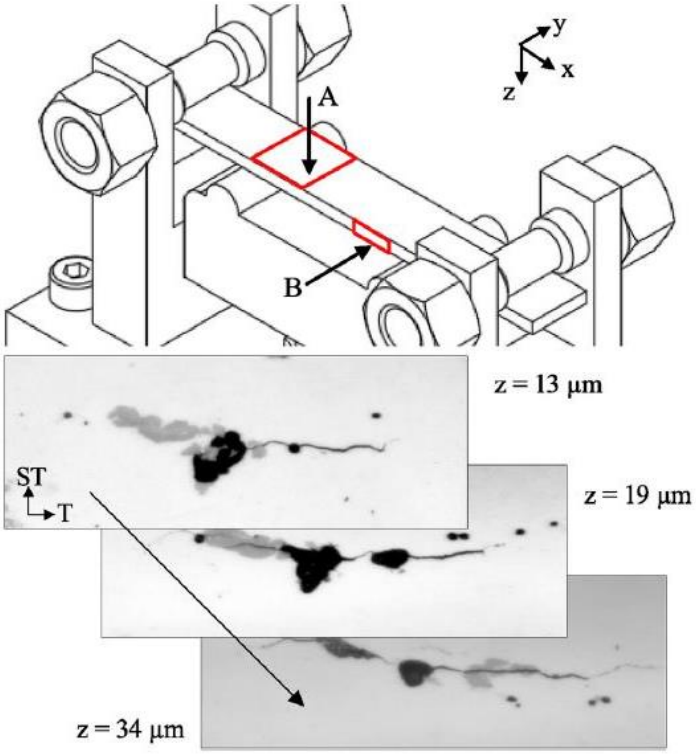

Figure 2-22. 4-point in-situ bend test for the AA7075, displaying a crack growing along the transverse direction with sequential polishing steps showing the development below the surface. [74]

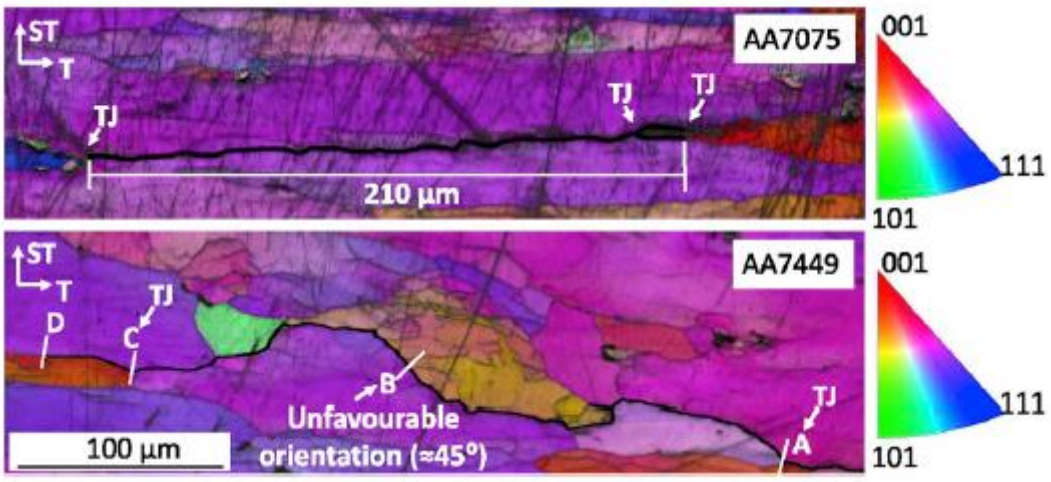

Figure 2-23. EBSD showing similar crack lengths were a) for the AA7075 the crack growths along the grain boundary and is arrested at a triple junction and b) crack in AA7449 keeps growing despite obstacles [74]

2.10. Summary

Aluminium alloys 7xxx series are high strength materials which are very promising for the aerospace structural industry due to their high mechanical properties, but when aluminium alloys are exposed to moist air environments such properties decrease causing detrimental effects in the microstructure; many attempts have been made to understand how hydrogen interacts with the material microstructure, and hydrogen is believed to enhanced plasticity closed to crack tips and to promote an increase in the egress of dislocations from crack tips, augmenting dislocations mobility rates and speed.

Hydrogen embrittlement study is complex because it requires the understanding of microstructure features like grain size, orientation, precipitates, second phase particles, hydrogen embrittlement mechanisms, dislocation theory, and fractography. Lately, for high strength aluminium alloys, it is still not clear how hydrogen interacts with the microstructure under the presence of moist air with the grain size, orientation and strain localisation. The primary aim of this work is to analyse the effects of hydrogen in cracks and void nucleation for a high zinc 7xxx alloy (AA7040). To this end, in-situ and ex-situ tensile SSRT tests are performed at different humidity levels and strain rates.

Chapter 3.
Experimental Methods

3.1. Introduction

In the development of the present research a variety of imaging and analysing techniques were used, to determine the effects of hydrogen embrittlement in the slip behaviour and the microstructure of the aluminium alloy 7040-T7651, by the comparison of the material in moist air (detrimental environment) and hydrogen-free environments. This chapter provides the reader with basic operation principles theory regarding the different techniques employed, followed by each technique importance in the subsequent data analysis.

All of the experimental and analytical techniques used to carry out this research have been summarised in the flow chart in figure 3-1.

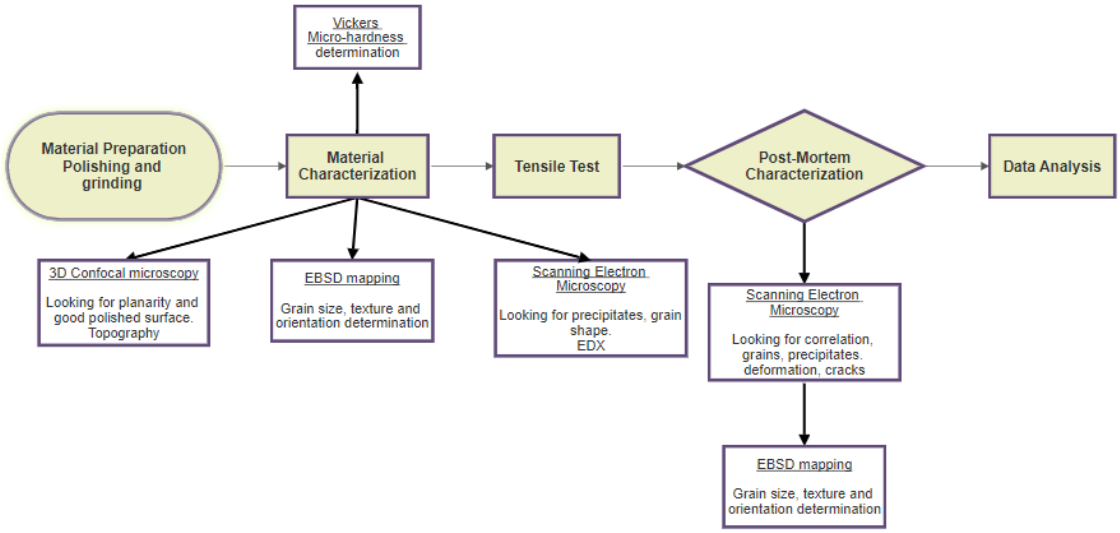

Figure 3-1. Methodology employed in the development of the present research

3.2. Confocal Laser Scanning Microscopy (CLSM)

Confocal microscopy is superior to conventional optical microscopy as it is designed to reduce or eliminate light from non-focal planes by applying spatial filtering techniques, obtaining images with better optical resolution and contrast. Nowadays, confocal microscopes are widely used in the material science industry as they allow the acquisition of high resolution/quality images. (Leiva-Garcia, Antón & Muños-Portero, 2011, Fellers & Davidson, 2020) [75, 76]

3.2.1. Operation Principle of the CLSM

In confocal microscopes, a laser source emits light that passes through a pinhole and then is reflected in a dichromatic mirror, scanning the specimen in focal planes. Secondary fluorescence generated at the specimen goes to a photomultiplier detector, in which a second pinhole located before the detector reduces the presence of out of focus light rays, as is illustrated in figure 3-2. (Fellers & Davidson, 2020) [76]

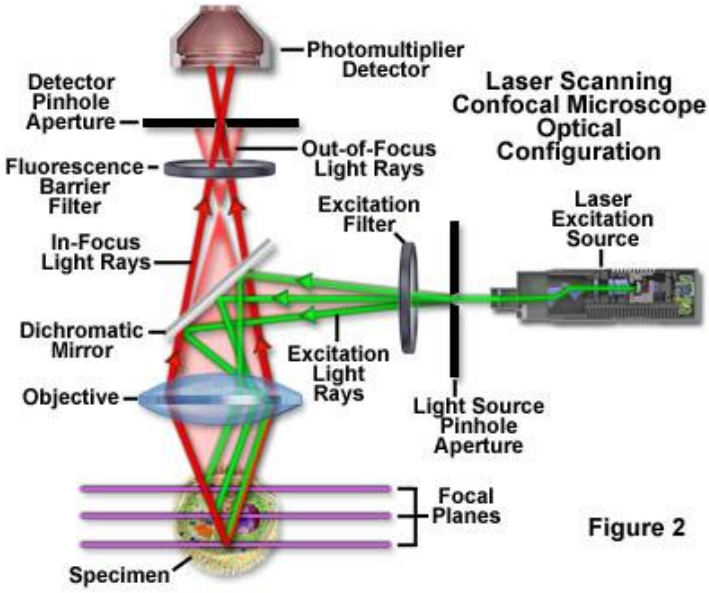

Figure 3.2. Illustration of a confocal scanning laser microscope. [76]

3.2.2. Outcomes of CLSM technique in the present research

Confocal Laser Scanning Microscopy was used in this research to determine: i) microstructure of the as-received material, ii) grain size, and iii) planarity of polished surfaces for the following scanning electron microscopy and electron backscatter diffraction data acquisition.

3.3. Scanning Electron Microscopy (SEM)

The Scanning Electron Microscope (SEM) was developed in the 1960s, as preparation for other imaging techniques like TEM, which required complex sample preparation; since then SEM microscopes have been improved to obtain high-resolution imaging.

Nowadays, SEM microscopy has a good depth of field and high spatial resolution, giving images of high quality and precise interpretation. (Egerton, 2005) [77]

3.3.1. Operation Principle of the SEM

SEM Microscopy is an imaging technique that analyses bulk specimens and requires easy sample preparation. The principle of operation is known as the "scanning principle", in which an electron probe scans through the sample surface while the direction of the incident beam changes by the influence of electrostatic or magnetic fields. (Egerton, 2005) [77]

The primary electron source is generated using: i) tungsten wire, ii) LaB6 or iii) a tungsten field-emission tip; next, the beam is accelerated using a voltage that ranges from 1-30 KV. Later, to increase the resolution of the final image, a reduction in the electron probe diameter is achieved through the objective lens. Finally, detectors collect the data and transform it into photons using a scintillator as can be seen in figure 3-3. (Egerton, 2005, Microscopy Australia, 2020) [77-78]

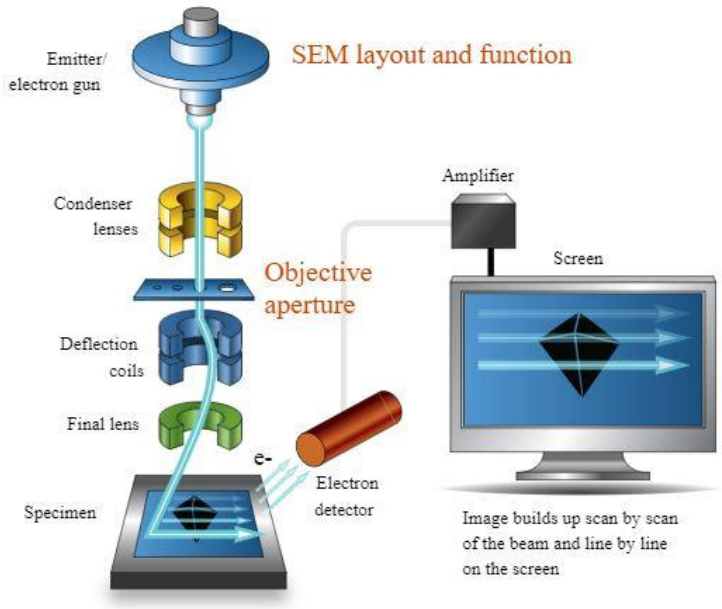

Figure 3-3. Illustration of an SEM microscope microstructure showing the electron gun, lenses, detector and last image obtained. [78]

When the electron beam interacts with the bulk material a) some electrons from the primary source are then absorbed into the solid to a certain depth, this is known as "penetration depth", and the volume at which this happened is highly dependent on the atomic number and is called "interaction volume". As a result of the beam interaction, b) different kinds of electrons are produced, which are X-rays, backscattered and secondary electrons. Each electron kind has different depths of penetration and then will be collected to obtain the final SEM image, as may be observed in figure 3-4 a and b respectively. (Egerton, 2005) [77]

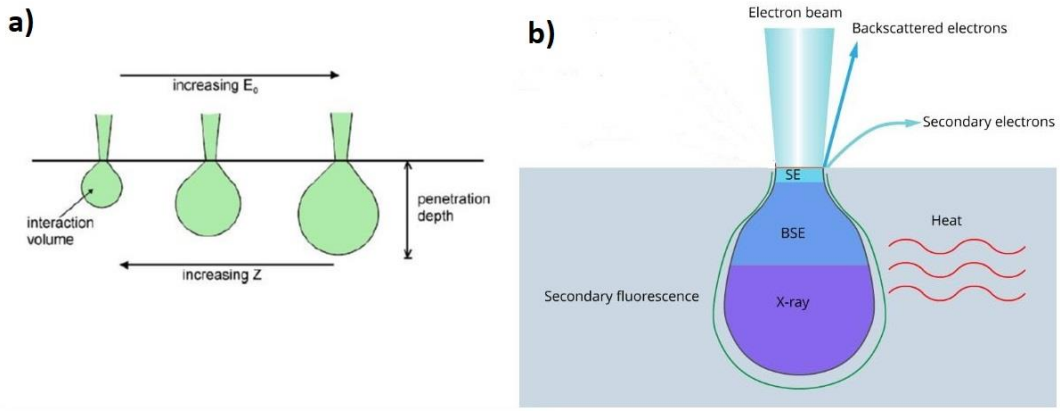

Figure 3-4. Effects of the interaction between the electron beam and bulk samples in SEM microscopy, a) relation between penetration-depth and volume-interaction with the atomic number and b) different electrons collected and depth of interaction of each. [77-78]

SEM technique has many advantages compared with other microscopy techniques; it requires simple sample preparation and provides topography information and 3D appearance due to its improved depth of field. Also, when specific detectors are added, SEM microscopy contributes with: the material compositional information using BSE detectors, X-ray analysis by attaching EDS or WDS detectors, and orientation and texture information when EBSD detectors are in used. (Microscopy Australia, 2020) [78]

3.3.1.1. Secondary Electron Imaging

Secondary electrons (SE) are generated because of inelastic scattering, in which electrons of the primary beam are: i) bound to the valence electrons or ii) bound to the conduction band of electrons. Secondary electrons have low kinetic energy, and only

very few of them are able to move in the surface of the material and scape into the vacuum. Because the depth of interaction of SE is shallower than for BSE electrons, secondary electrons are used to determine the topography of fractures. The SE image is obtained as a positive biased electrode improves the collected signal of secondary electrons. Later, the current is amplified and finally, an optimum operation voltage, beam current, aperture size and working distance selection are fundamental to obtain the best quality image. (Lynch, 2012; Egerton, 2005; Goldstein, et al., 2017) [45, 77, 79]

3.3.1.2. Backscatter Electron Imaging

Backscattered electrons (BSE) are generated at greater depths than SEs by electrons that are elastically scattered with an angle higher than 90 degrees, providing crucial information about the material characteristics. When the material has a higher atomic number, the collected BSEs increases compare with lower atomic number elements; allowing BSE images to show good atomic number contrast and an excellent response to the material composition. (Egerton, 2005; Goldstein, et al., 2017) [77, 79]

3.3.1.3. Energy-Dispersive X-ray Spectroscopy. (XEDS)

The Energy-Dispersive X-ray spectroscopy technique determines the chemical composition of materials thanks to x-rays emitted when the beam interacts with the sample surface. As the probability of inelastic scattering is minimal, electrons go through a transition to a higher-energy orbit leaving an electron vacancy. Then, electrons go to an equilibrium state releasing a photon (x-ray), the quantity of energy release is characteristic of the element atomic number. (Egerton, 2005) [77]

EDS detectors are conductor diodes that are added up to SEM microscopes, in which the beam may be trained to analyse specific points on the surface of the material or areas containing multiple sites, creating distribution EDS maps. Then the analysis of particles, points of interest and the general composition of materials is possible, obtaining resolutions up to 1 um. (Egerton, 2005) [77]

3.3.2. Outcomes of SEM technique in the present research

Scanning Electron Microscopy is one of the main techniques employed in this research, in which secondary and backscatter electron images were collected to analysed: i) the microstructure of the as-received material, ii) grain boundaries, iii) precipitates, iv) topography of the deformed material after tensile testing and v) the general composition using EDS techniques.

3.4. Electron Backscattering diffraction (EBSD).

Electron backscattering diffraction is a characterisation tool that can be attached to SEMs, to obtained texture, phase identification and orientation information in polycrystals. (Schwartz, et al., 2009) [80]

3.4.1. Operation Principle of EBSD

3.4.1.1. Kikuchi Diffraction Pattern

Backscattered electrons interact with the lattice planes at a depth closed to 20 nm from the specimen surface creating diffractions that are collected in a phosphor screen as two lines known as “Kikuchi bands” which width will correspond to the specific crystallographic planes as may be observed in figure 3-5a. A group of “Kikuchi bands” are called “Kikuchi pattern”, and the angles formed between bands give information about the crystal symmetry (figure 3-5b), materials with higher atomic number will have sharper patterns than those with low atomic number. (Schwartz, et al., 2009; Engler & Randle, 2009) [80, 81]

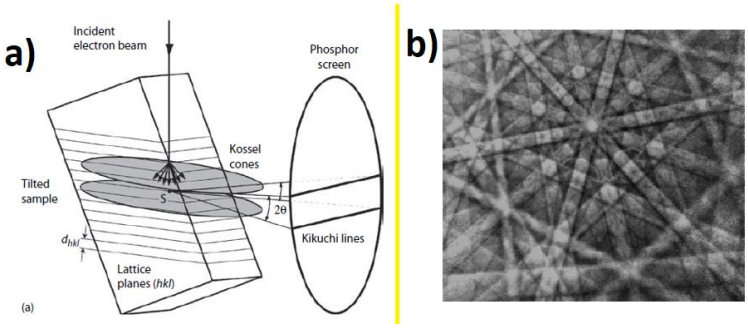

Figure 3-5. a) Electron beam interacting with the specimen surface generating two lines in a phosphor screen and b) Kikuchi pattern of a cadmium sample obtained at 20 keV. [81]

3.4.1.2. Pattern Acquisition Parameters

EBSD maps acquisition is a complex process, which quality depends on the adequate manipulation of specific parameters. The specimen to "phosphor screen" distance is a fixed parameter for each SEM. The specimen tilt is an angle between 60-70 degrees that allows more electrons to be diffracted and collected at the detector; the standard angle is 70 degrees. The specimen working distance and the accelerating voltage keep a linear relationship with the interaction volume, obtaining better resolution when a low accelerating voltage is utilised. (Engler & Randle, 2009) [81] Figure 3-6 proportion two cases where a 70 degrees sample tilt is done while different sample orientations are observed.

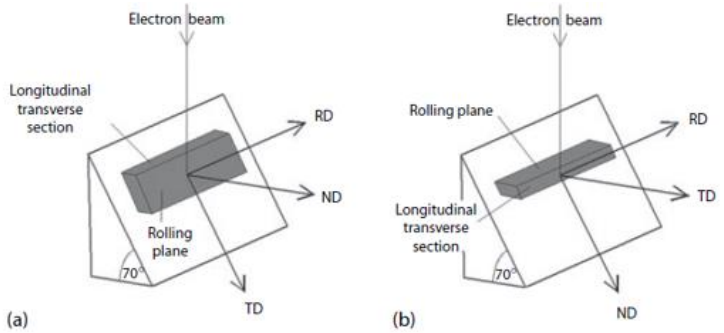

Figure 3-6. EBSD acquisition for different sample orientations using the standard sample tilt of 70 degrees. [81]

3.4.1.3. Euler Angles and Euler Maps

Euler angles are a conventional representation of sample orientation using a coordinate system known as Euler Space; this information can be collected as Euler maps. However,

Euler maps are difficult to interpret becoming more practical the utilisation of Inversed Pole Figures. (Engler & Randle, 2009) [81]

3.4.1.4. Inversed Pole Figures (IPF)

When Inversed Pole Figure maps are used, texture and orientation information will be displayed using the crystal coordinate system. The representation is done using a triangle with the axes <100>, <110>, and <111> that correspond to the material crystallographic planes, as shown in figure 3-7, which are easier to interpret and analyse as variations in orientation are represented with fewer colour changes than the Euler angle system. (Engler & Randle, 2009; Oxford Instruments, 2019) [81, 82]

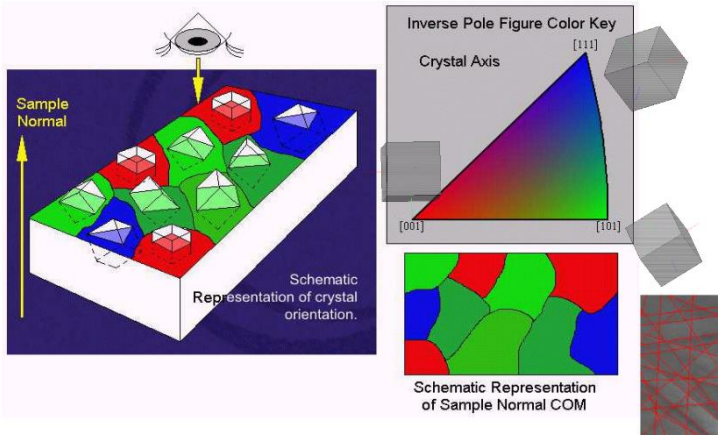

Figure 3-7. Representation of the Inversed Pole Figure representation system, where the crystallographic orientation is shown in a triangle related to the crystallographic coordinate system. [82]

3.4.2. Outcomes of the EBSD technique in the present research

Electron Backscattering Diffraction was used to collect: i) the microstructure of the as-received material, ii) grain boundaries, iii) orientation and iv) texture. EBSD inversed pole figure maps were taken before and after tensile tests to correlate the effects of the microstructure, texture and orientation with cracks formation and propagation in vacuum and humid-air environments.

Chapter 4.
Material Characterisation

4.1. Introduction.

The aluminium alloy selected for the present research is the commercial AA7040-T7651; the basic mechanical properties, the composition and microstructure are the starting point to analyse variations after tensile testing in different environments and strain rates. In this chapter, the experimental methods for the present research will be explained followed by the results of the as-received condition properties of the alloy.

4.2. Experimental Methods and Results

4.2.1. Material

The present study will focus on the material AA7040-T7651 that is a commercial (Al- Mg-Zn-Cu) 7xxx series alloy in the as-received conditions, in which blocks of the material have a thickness of 110 mm as shown in figure 4-1, the general composition of the material is given in the table 4-1. (WA Alloys, 2015; Dumont, et al., 2004) [83, 84]

Figure 4-1. Blocks of the as-received wrought commercial alloy AA7040-T7651

Table 4-1. Chemical composition in weight percentage of the Aluminium Alloy AA 7040-T7651. (WA Alloys, 2015; Dumont, et al., 2004) [83, 84]

Alloy	Si	Fe	Cu	Mn	Mg	Cr	Zn	Zr	Ti
AA 7040–T7651	0.1	0.13	1.5-2.3	0.04	1.7-2,4	0.04	5.7-6.7	0.05-0.12	0.06

4.2.2. Metallographic Preparation

Wrought aluminium alloys have anisotropic properties due to grain deformation and elongation along the rolling direction; the present study investigates the material properties across the rolling direction as it is the most susceptible to crack propagation. Then, all samples in this research were obtained from the middle of the block (T/2) on the longitudinal-short transverse plane, as shown in figure 4-2.

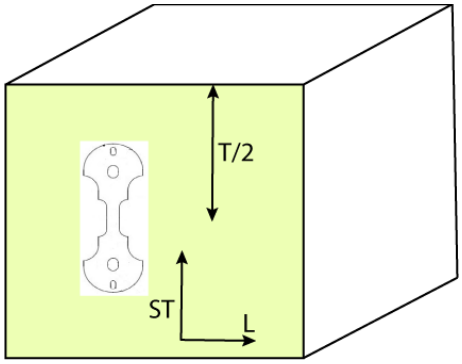

Figure 4.2. Illustration of AA7040-T7651 blocks showing the area from which specimens were cut (T/2) in the longitudinal-short transverse plane.

All samples were cut using electro-discharge machining (EDM) as this technique can produce samples with complex shapes and accurate dimensions with high precision in all the specimens, (Rajurkar, Sundaram & Malshe, 2013) [85] a lubricant is used to avoid changes in material properties due to any localised heating. After the EDM process all samples were grinded, polished, and analized under the SEM microscopes. It was determine that no unusual effects that could produce crack initiation were introduced during the EDM cutting process. Two sample models displayed in figure 4-3 were prepared to obtain the as-received mechanical properties of the material (a) and to determine the effects of hydrogen embrittlement during tensile testing in different environments (b).

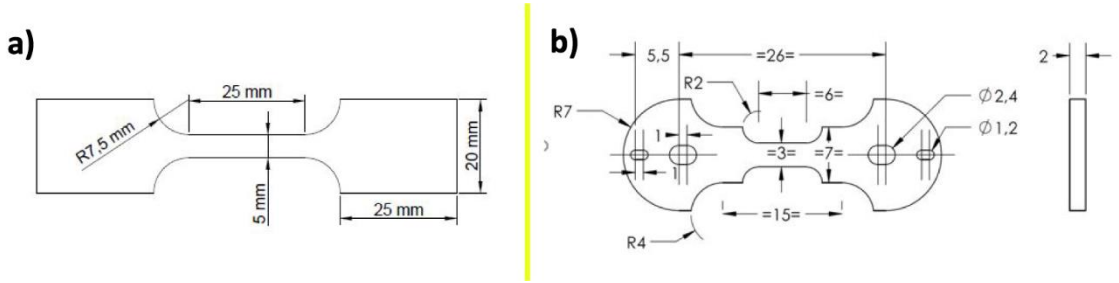

Figure 4-3. Samples types preparation using EDM for a) getting the as-received mechanical properties and b) in-situ and ex-situ tensile testing and SEM acquisition.

Samples used for obtaining the as-received mechanical properties of the material were used after cutting without further surface preparation. On the other hand, all samples employed in interrupted tensile tests were stuck in a polishing wheel, as displayed in figure 4-4; next, grinding started using silicon carbide paper $P600$ followed by $P800$, $P1200$ and $P2400$ respectively using a rotating grinding machine set at 150 RPM, ethanol was used instead of water as a lubricant. Subsequently, the polishing process was achieved with oil-based monocrystalline diamond suspensions beginning at 3 um and followed by $1\ um$, and ¼ um respectively that were applied to polishing cloths in rotating machines at 150 RPM. Afterwards, OPS was diluted in distilled water (1:4 ratio) using OPS polishing cloths at 60 $RPMs$ for 10 min, as it was critical to diminish specimens contact with water. It is essential to point out that in-between-steps, samples were cleaned using only ultrasonic baths with ethanol to avoid water contact. Finally, samples were removed from the wheel using ethanol ultrasonic baths at 40 degrees and blow-dried immediately afterwards. Prepared samples were stored at a desiccator filled with silica gel at all times and samples transportation was realized in SEM boxes with silica gel to keep any possible exposition of the specimens to contamination and hydrogen intake to a minimum.

Figure 4.4. Samples stuck to a polishing wheel; this method ensures that all samples mounted will have a similar thickness for posterior analysis.

4.2.3. Confocal Laser Scanning Microscopy

The confocal microscope Keyence X200K 3D Laser was used to observed polished samples to determine the planarity of samples. Also, etching was performed in samples using the Keller Reagent (2 ml HF, 1 g NaOH, 100 ml water) for 15 seconds to observe the microstructure of the alloy.

4.2.4. Micro-hardness Testing

Vickers micro-hardness testing was performed on AA 7040-T7651 samples prepared as described in section 4.2.2. The tests consist in the application of a 300 grams load and 10 seconds at each indentation, using the Matsuzawa Micro Vickers MMT-X series machine. Measurement of hardness on each specimen consists of the indentation of a minimum of three points in the centre of the sample, the distance between edges and indents should be at least 300 um.

4.2.5. Tensile Testing

Aluminium alloys 7040-T7651 were tested at T/2 using a Static Testing Machines (STM) INSTRON 5569H1549 to obtain mechanical properties; all tests were performed at a strain rate of $10^{-3}\ /s$ in samples shown in figure 4-2a. In-situ and Ex-situ interrupted

slow strain rate tensile tests (SSRT) were done using the Tescan and NewTec In-Situ Testing Station (TANIST); which is a system that alloys mechanical testing while imaging at good resolutions. (HENRY ROYCE INSTITUTE, 2020) [86]. The parameters at which the tensile tests took place can be found in table 4-3, all samples were prepared as shown in figure 4-2b and polished as explained in section 4.2.2., then samples were exposed to the desired environments at least 30 minutes before starting tensile tests. 50%RH environments were achieved in the ex-situ tests by the introduction of a cup with water in the testing chamber, while 90%RH used a cup with water and a pressure of 0.1 Pa, humidity levels were measured with the Lascar EL-USB-TC Temperature Data Logger, as can be observed in figure 4-5.

Table 4-2. Tensile Testing parameters for AA7040-T7651 samples.

Sample	Humidity $(\%RH)$	Strain Rate (s^{-1})	Method
1	0	$1 * 10^{-5}$	In-situ
2	50	$1 * 10^{-5}$	Ex-situ
3	90	$1 * 10^{-5}$	Ex-situ
4	0	$1 * 10^{-6}$	In-situ
5	50	$1 * 10^{-6}$	Ex-situ

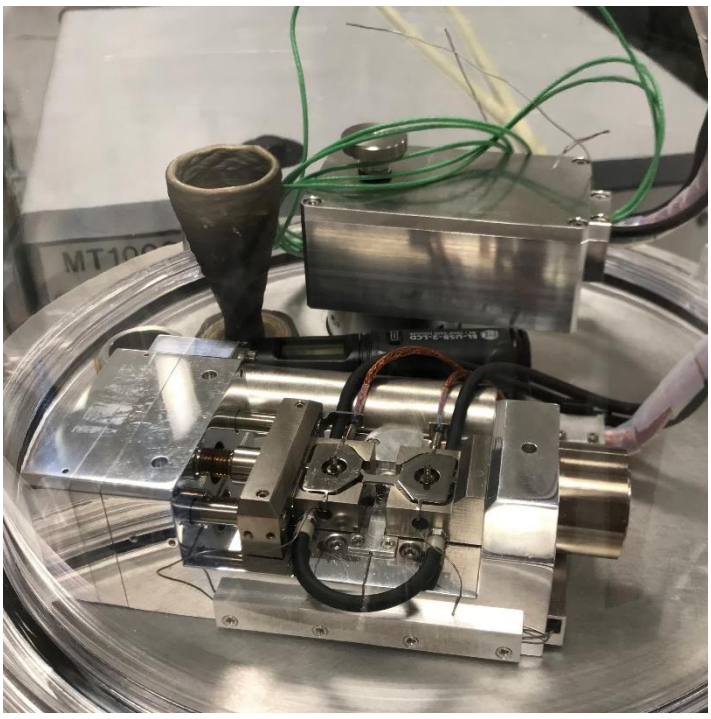

Figure 4-5. Ex-situ interrupted tensile test, lab air environments is generated with a cup of water using the Tescan and NewTec In-Situ Testing Station (TANIST), humidity was measured with the the Lascar EL-USB-TC Temperature Data Logger.

4.2.6. Scanning Electron Microscopy (SEM)

The Scanning Electron Microscopes (SEM) Tescan Mira3 and the FEI Magellan HR FEGSEM were used to study the material microstructure, along with EDS and EBSD detectors. Detailed information for the different parameters used while imaging samples can be found in table 4-3. The acquisition parameters for EBSD maps and EDS information are 20 kV accelerating voltage, 96 uA and 1.5 um step size when the sampled is tilted a 70-degrees angle; the data was processed using the AZTEC software; finally, EBSD maps were transformed into IPF (inverse poled figures), Taylor factor and Schmid factor maps using the software Tango – maps app.

Table 4-3. SEM imaging parameters for AA7040-T7651 samples in different experiments during and after testing.

Sample	Experiment	Beam Energy (kV)	Beam Current	Detectors
1	In-Situ	5	1 (pA)	BSE COMPU
	Post Morten	13	78 (uA)	SE and BSE
	Overview Image	20	3 (pA)	
	Fracture Surface	13	78 (uA)	
	Lateral View			
2	Post Morten	8	78 (uA)	SE and BSE
	Overview Image			
	Fracture Surface	13	78 (uA)	BSE COMPU
	Lateral View			
3	Post Morten	8	78 (uA)	SE and BSE
	Overview Image			
	Fracture Surface	13	78 (uA)	
	Lateral View			
4	In-Situ	5	1 (pA)	BSE COMPU
	Post Morten	20	3 (pA)	
	Overview Image			
	Fracture Surface			
	Lateral View			
5	Post Morten	20	3 (pA)	BSE COMPU
	Overview Image			
	Fracture Surface			
	Lateral View			

4.3. Results and Discussion

4.3.1. Metallographic Studies

Understanding the metallography of the commercial aluminium alloy AA7040-T7651 is a priority for the development of the present research, there is little information about this high zinc aluminium alloy along the ST/L plane. Figure 4-6 displays the microstructure revealed by Keller Reagent, using confocal microscopy in the ST/l plane, the alloy is anisotropic as grains are elongated along the longitudinal direction, in a) crystallised and non-recrystallised grains are observed, and b) shows constituent particles at grain boundaries interceptions.

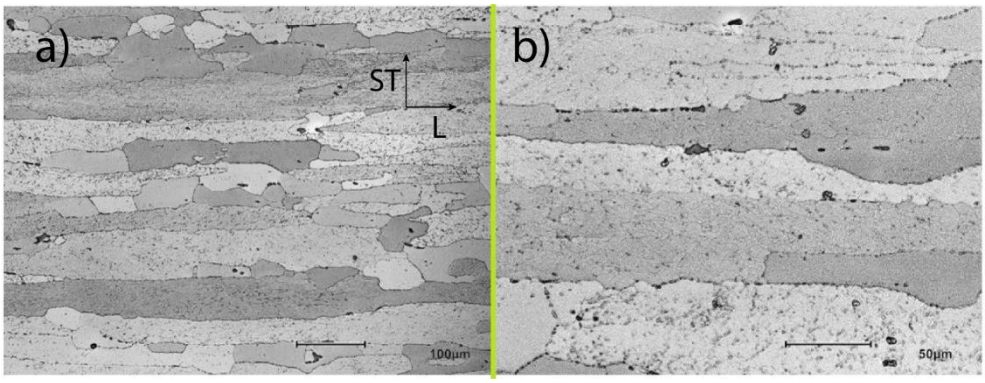

Figure 4-6. AA7040-T7651 microstructure along ST/L plane observed with the confocal microscope Keyence X200K 3D Laser a) 100 um and b) 50 um scales.

Figure 4-7-a to b shows general microstructure features: recrystallised and non-recrystallised grains, sub-grains, constituent particles, and grain boundary precipitates acquired using the TESCAN Mira3 SEM. Figure 4-7-c (10 kV) and figures 4-7-d to e (5 kV) were obtained with the FEI Magellan HR SEM, showing high-resolution images were sub-grain boundary precipitates are seen along with the matrix precipitates (small particles) and precipitate-free zones. Generally, a flat surface is seen after polishing, and only a few particles are dissolved, as a consequence of the OPS polishing step, despite attempts to avoid contact with water.

4.3.1.1. Composition

Composition in weight was obtained using the FEI Quanta 650 FEG(E)SEM + EBSD + EDX, for the most important alloying elements in the commercial alloy 7040-T7651. As can be seen in figure 4-8, the alloy in the as-received condition is composed by 1.6 % copper, 1.6 % Mg and 6.5% Zn, which is in agreement with the chemical composition find in table 4-1.

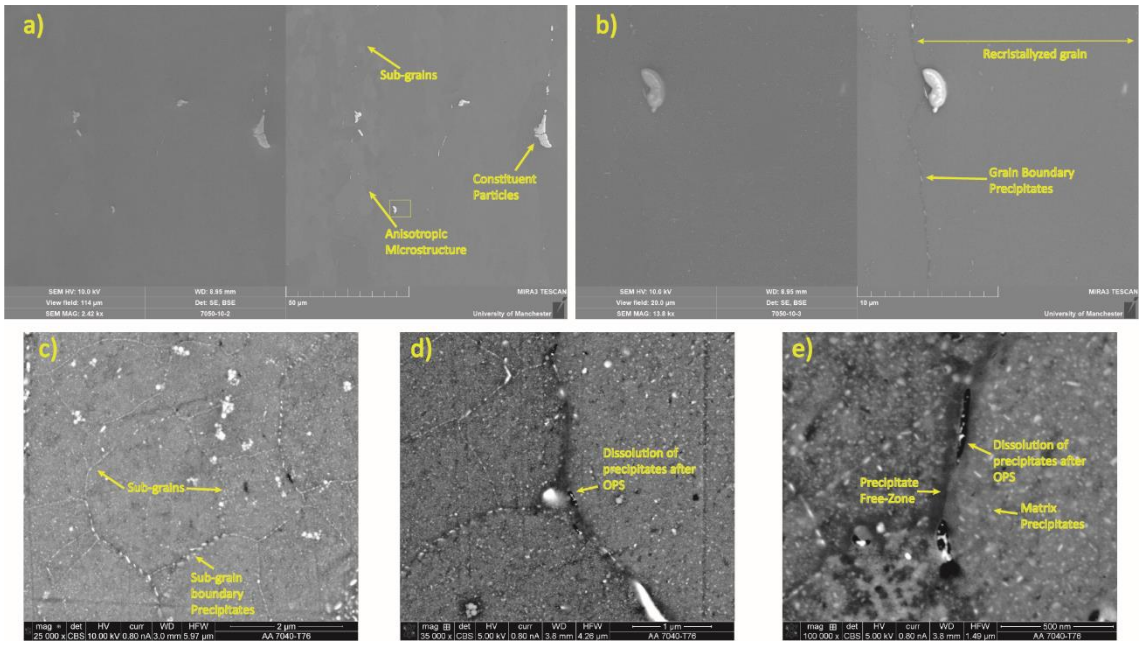

Figure 4-7. SEM imaging shows the microstructure features of a commercial AA 7040-T7651 alloy a) constituent particles and anisotropic microstructure, b) recrystallized grains and grain boundary precipitates, c) sub-grains and sub-grain boundary precipitates, d) dissolution of precipitates due to OPS and e) high-resolution image of matrix precipitates and PFZ.

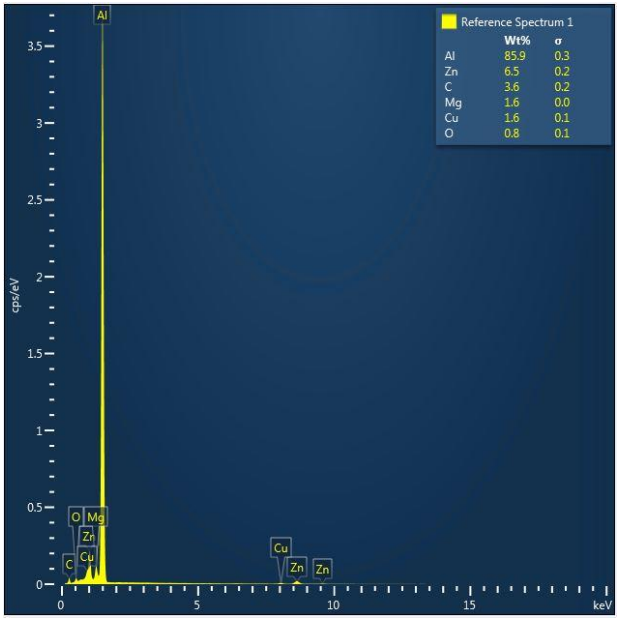

Figure 4-8. EDS chemical composition results for the commercial AA7040-T7651 in T/2.

4.3.1.2. Grain Size

Figure 4-9 indicates a linear intercept method in two perpendicular directions used to compute grain size; A confocal image and the ImageJ software were used to determine the average size of grains in the directions ST and L, then it was concluded that elongated grains of AA7040-T7651 have: 122 um length and 32 um width.

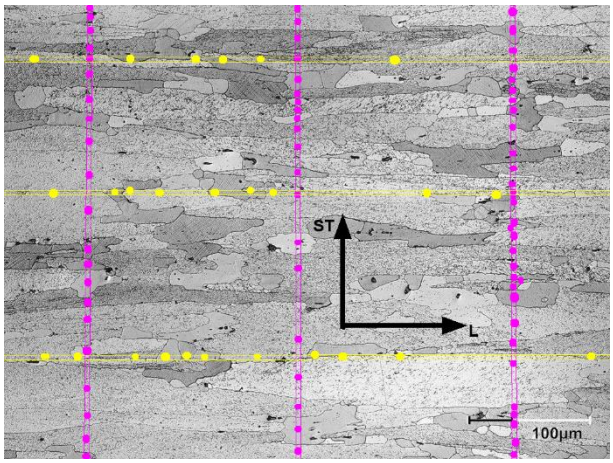

Figure 4.9. Linear intercept method used to determine grain size in AA7040-T7651.

4.3.1.3. Recrystallisation

The addition of alloying elements allows the precipitation of particles, which may stop the recrystallization of grains; EBSD maps were taken in polished samples, as described in 4.2.2 section, to determine the effect in the AA7040-T7651 alloy. Tango software processes EBSD maps to obtain a recrystallisation map, as can be seen in figure 4-10, in which blue and yellow grains are recrystallized. A clear heterogeneity pattern is observed as most grains are non-recrystallised; only specific regions shows recrystallised grain forming: i) clusters and ii) long chains along the sample width.

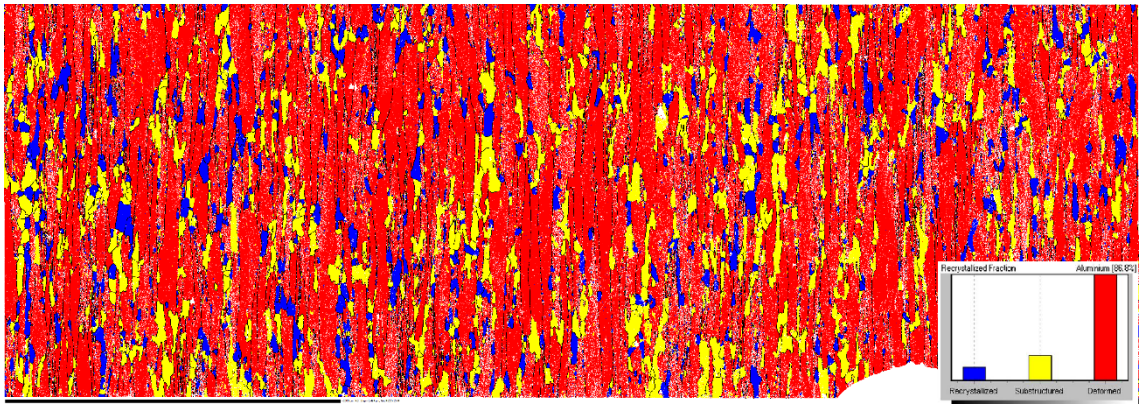

Figure 4-10. EBSD maps process using Tango software to determine recrystallized grains displays high recrystallisation heterogeneity.

4.3.2. Micro-hardness

Vickers hardness was obtained on polished samples from T/2 as described in 4.2.5 section using a micro-Vickers hardness tester Matsuzawa MMT-X series, seen in figure 4.11; three measurements were obtained and averaged to obtain a hardness of 167 Vickers.

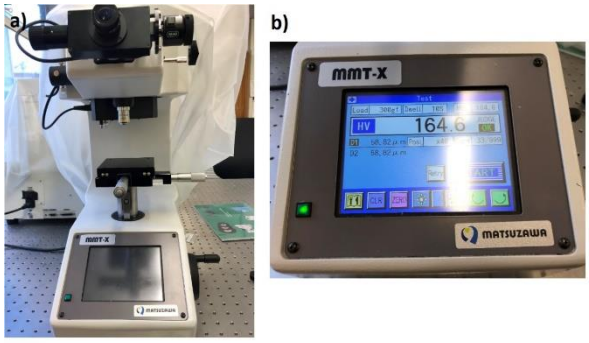

Figure 4-11. Measurement of Vickers hardness a) Micro-hardness tester Matsuzawa MMT-X and b) configuration and measurement of Vickers hardness on AA7040-T7651.

4.3.3. Tensile Testing

Tensile tests, described in section 4.2.6., were performed in four samples which dimensions are shown in table 4.4. Figure 4-12 resumes the mechanical properties obtained for the as-received alloy AA7040-T7651; the final values are the average results for all samples tested, in which the pseudo modulus of elasticity (E) is 60 GPa, this value is lower than the typical modulus for the alloy AA7040 because it includes a significant input from the stiffness of the loading frame, the Yield strength (σ_Y) is 458 MPa, The ultimate tensile strength (UTS) is 509 MPa, fracture strength (σ_F) is 477 MPa, at 10^{-3} $/s$ strain rate and the 7.8 % total strain and 5.9 % plastic strain.

Table 4-4. 7040-T7651 sample dimensions for tensile testing.

Sample	Length (mm)	Thickness (mm)	Width (mm)
1	25	2.12	5.07
2	25	1.97	4.94
3	25	1.96	4.95
4	25	1.96	4.97

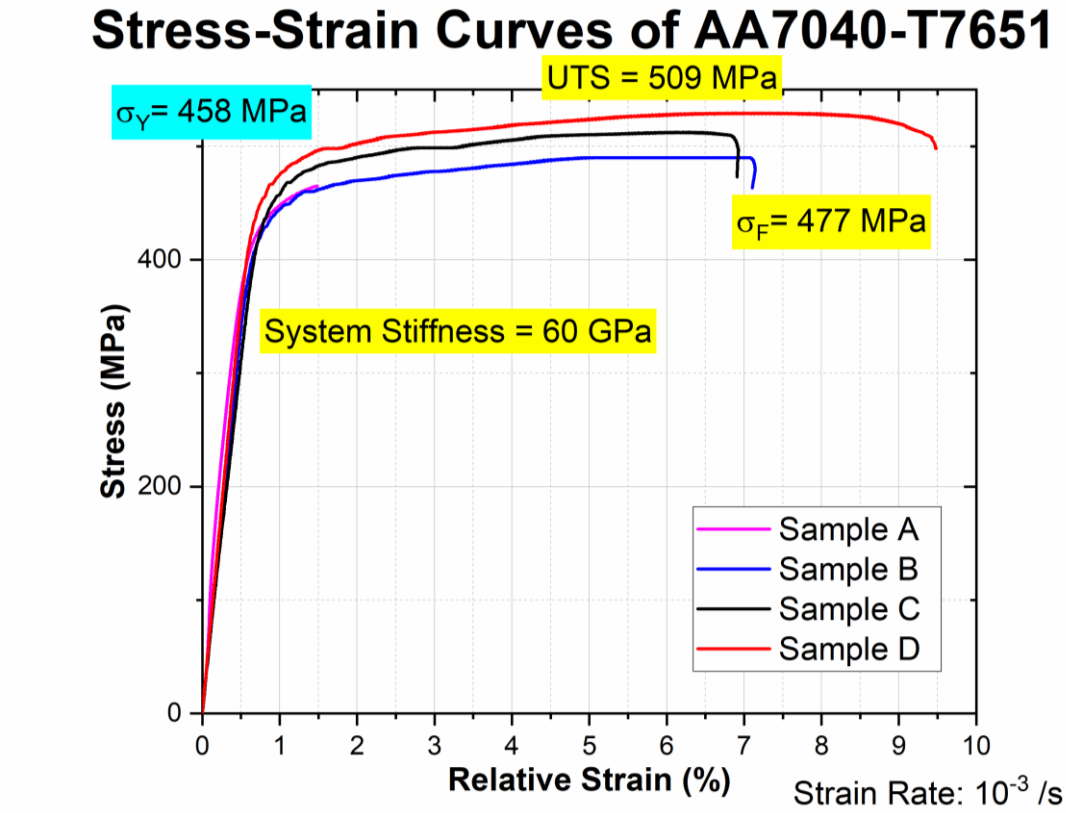

Figure 4-12. Stress-strain curved showing the main mechanical properties of the commercial AA7040-T7651 in the as-received conditions for samples tested at 10^{-3} /s strain rate.

Chapter 5. Effects of Hydrogen Embrittlement in AA7040-T7651 In Stress-Strain Curves.

5.1. Introduction

The present chapter provides the stress-strain curves of tensile tests of aluminium 7xxx series alloy AA7040-T765. First, a general comparison of the stress-strain and stress-time curves will be presented. Then, the analysis of mechanical properties for samples tested at different susceptible environments for specific strain rates is provided and compared. To conclude, an interpretation of the data presented is discussed.

5.2. Results

All the tests presented in this chapter were performed in aluminium alloy 7040-T7651 samples in the as-received condition; surface preparation was done as explained in section 4.2.2, then interrupted slow strain rate testing was done as discussed in section 4.2.5.

5.2.1. Stress-strain curves and stress-time curves during SSRT tests under different conditions.

Effects of hydrogen embrittlement in the microstructure of the material were analysed using interrupted slow strain rate testing $(SSRT)$ in the short transverse direction, while the material is in dry air $(0\%\ RH)$, laboratory air $(50\%RH)$ and high humidity $(90\%RH)$ at two different strain rates. In figure 5-1, all the tests stress-strain curves can be observed; all tests were interrupted at different stages of the test, to discard the effects of creep in the mechanical behaviour of the material by allowing relaxation of the samples while keeping a constant elongation at specific periods. The tests generally follow the expected behaviour, in which samples exposed to humidity environments present a diminution in the time to failure, total strain, yield stress and UTS; however, no significant differences were detected between samples tested under the same strain rate, this could be because the nominal strain is too high to allow Intergranular Type-1 EIC initiation of the 7040-T7651 overaged alloy.

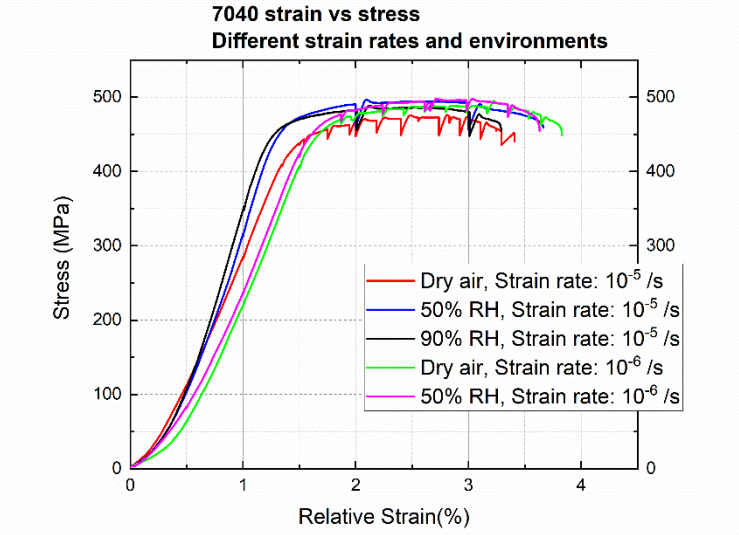

Figure 5-1. Stress-strain curves for all SSRT tests, showing little variations in the mechanical behaviour of the material at different environments and strains.

Stress-time curves are shown in figure 5-2, in which for tests at a strain rate of $10^{-5}\ /s$, it is clear that relaxation periods are not similar in all tests; for instance, sample 1 tested in dry air last 4100 seconds (16.4%) less than the test at 90% humidity, because the relaxation periods in dry air samples were more frequent due to image acquisition at in-situ tests. For tests at $10^{-6}\ /s$ strain rate relaxation periods are more similar between samples; however, the relaxation periods differ considerably after elastic deformation, and sample 5 failed 4846 seconds (10%) earlier than sample 4.

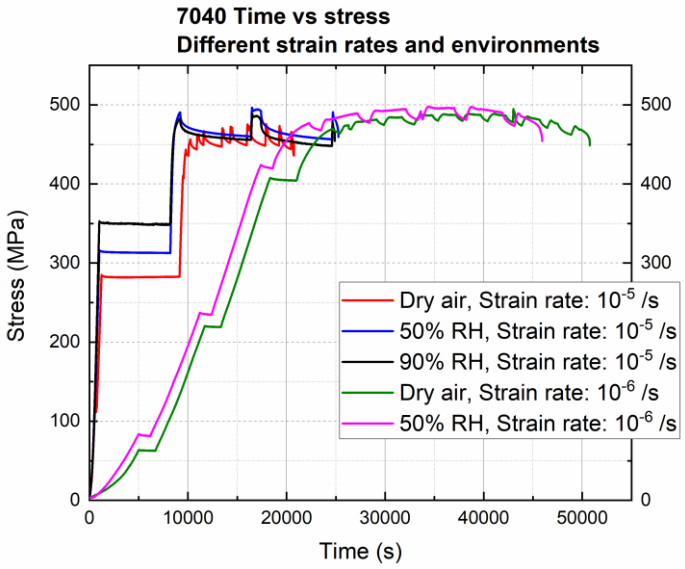

Figure 5-2. Stress-time curves for all SSRT tests, showing non-consistent relaxations periods of samples, and different times to failure.

5.2.1.1. Stress-strain curves comparison between environments at different strain rates.

Stress-strain curves for samples at a strain rate of $10^{-5}\ /s$, are displayed in figure 5-3; sample 1 tested in dry air failed at 1,55% plastic strain before than sample 2 tested at lab air (1,8% plastic strain), and it shows: i) inferior mechanical, ii) more relaxation periods and iii) lower total and plastic strain. On the other hand, sample 3 tested at 90%RH was tested with the same relaxation parameters of sample 2, and displays the lowest i) total strain (2,99%), ii) plastic strain (1,49%) and iv) the highest sloped (50 GPa).

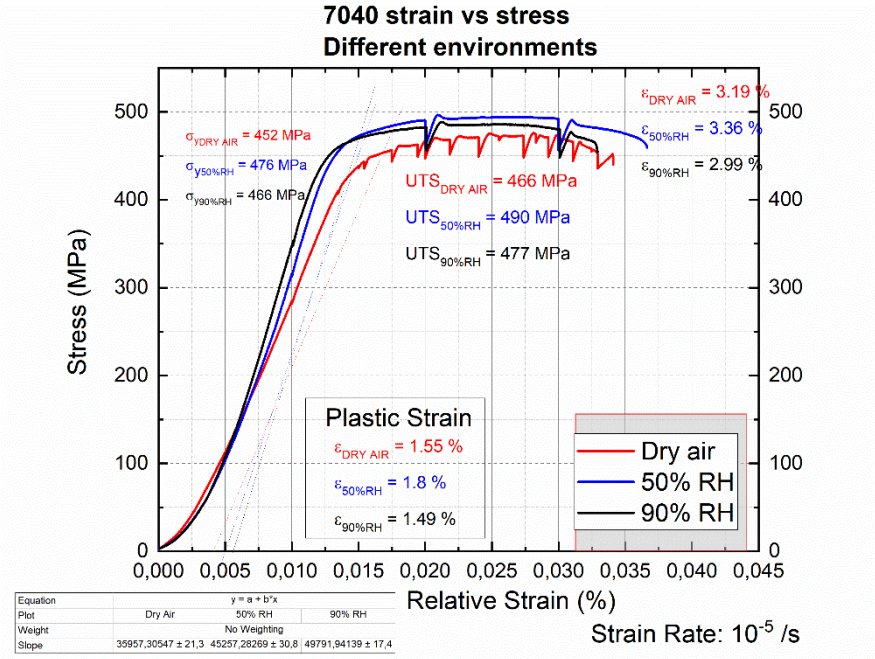

Figure 5-3. Stress-strain curves for SSRT tests at $10^{-5}\ /s$, showing: i) yield strength, ultimate tensile stress, total strain, plastic strain and slope for samples 1, 2 and 3.

Stress-strain curves for the samples 4 and 5 tested at a strain rate of $10^{-6}\ /s$, are displayed in figure 5-4. Sample 5 failed at 3,27% total strain before sample 4 tested in dry air (3,42% total strain), sample 5 also shows slightly inferior mechanical properties (UTS – 494 MPa and yield strength 470 MPa) and the lowest plastic strain (1,69%). The slope for both curves is similar (37GPa), and sample 4 displays more relaxation periods than sample 5 due to imaging acquisition.

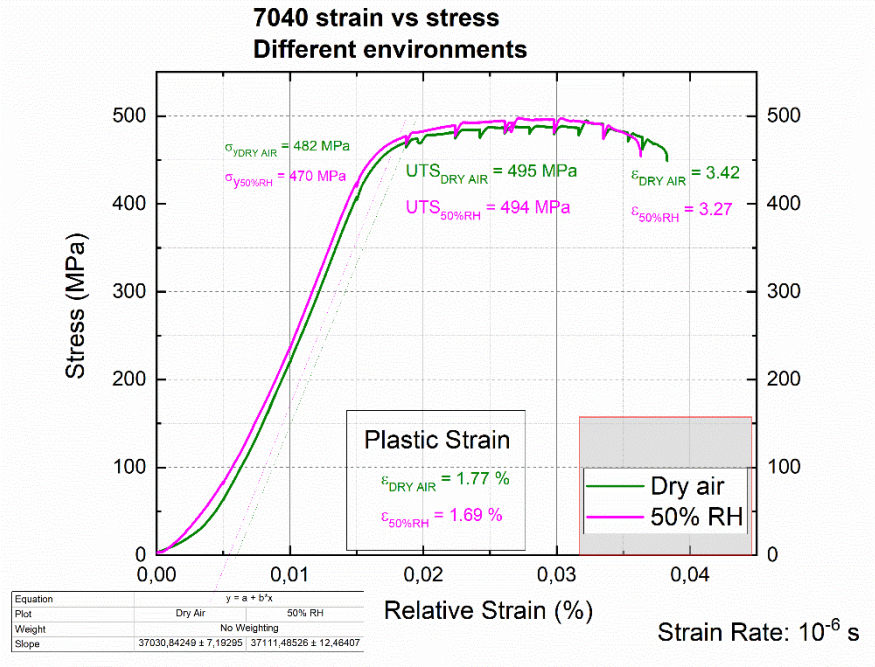

Figure 5-4. Stress-strain curves for SSRT tests at 10^{-6} $/s$ for samples 4(dry air) and 5 (lab air), displaying a slight diminution in yield strength, total strain and plastic strain for sample 5.

A summary of the results is presented in table 5-1; first, the slope of samples 2 and 3 are relatively alike and is important to mention that these tests were realized prior to a TANIST rig maintenance, once the rig was calibrated and ready to use samples 1, 4 and 5 were tested (presenting a similar slope); then, the slope is a characteristic of the rig employed and is believed that it does not have any detrimental effect in the mechanical properties measurements. There is a reduction of 75% in the plastic strain when comparing the present results with the tests realized to obtain the mechanical properties of the material in the as-received condition; these differences could be attributed to the higher strain used for the mechanical test and\or the different relaxation periods between samples as the difference is reduction in the plastic strain is higher than the expected.

Generally, the stress-strain curves do not show significant changes in the mechanical properties of the samples; however, it is observed that samples 2 and 3 have the same relaxation periods parameters during the tensile tests and present a reduction of 17% plastic strain. While, sample 5 has a lower plastic strain than sample 4 but, the change is relatively small (5% plastic strain) when a more significant difference was expected,

maybe due to the differences in the relaxation intervals. Sample 1 also shows an unexpected response; it showed a 13.9% plastic strain reduction in comparison with sample 2 when it was expected to have the highest elongation in the set of samples tested at 10^{-5} /s strain rate as it was tested in dry-air. However, more testing needs to be done for each environment to determine if the differences in the strains to failure are significant.

Table 5-1. SSRT tests parameters and mechanical properties obtained for AA7040-T7651 samples when exposed to different humidity levels and strain rates.

Sample	Humidity $(\%\boldsymbol{RH})$	Strain Rate $(\boldsymbol{s^{-1}})$	Time to failure $(\boldsymbol{s^{-1}})$	Slope $(\boldsymbol{GPa})$	Yield Stress $(\boldsymbol{MPa})$	UTS $(\boldsymbol{MPa})$	Total Strain $(\%)$	Plastic Strain $(\%)$
1	0	$1 * 10^{-5}$	20755	36	452	466	3,19	1,55
2	50	$1 * 10^{-5}$	25268	45	476	490	3,36	1,8
3	90	$1 * 10^{-5}$	24889	50	466	477	2,99	1,49
4	0	$1 * 10^{-6}$	50771	37	482	495	3,42	1,77
5	50	$1 * 10^{-6}$	45925	37	470	494	3,27	1,69

5.3. Discussion

Surprisingly, the reduction of 75% in the plastic strain for samples 1 and 4 tested at dry air (vacuum) when compared with the tensile test results in section 4.3.3., and the small variation in the total and plastic strain between all tests can be interpreted, as if hydrogen exposure and the strain rates variations play a minor role in the embrittlement of the material. However, a possible explanation for this might be the different relaxation periods applied and tests time durations; such variations occurred due to image acquisition periods on in-situ tests. Then, more testing needs to be done with and\or without image adquisition were possible to obtain comparable data for the tests with the same load holds, relaxation periods and for tests without any holds. For instance, sample 1 has the smallest test duration and 16 relaxation periods showing shorter elongation than sample 2 which has 4 relaxation periods, this might explain that sample 1 (dry air) have the lower mechanical properties as it has a high number of relaxation periods which could promote creep induced by load cycling (Evans and Parkings, 1975) [87]; also, samples 2 and 4 relaxation periods are alike and display a 17% variation in the plastic strain which is in agreement with the expected tendency in the mechanical properties when aluminium alloys are exposed to aqueous environments.

(Lynch, 2011)[15] Samples 4 and 5 also seem to correlate with the well-known hydrogen embrittlement theory; nevertheless, the difference in the plastic strain is only 5% contrary to expectations, in which a higher difference was expected, again this may be explained as the relation periods are 14 and 9 for samples 4 and 5 respectively. A possible explanation for the high reduction in plastic strain might be that when the sample has a stress relaxation, some localised hardening occurred in the material (Choudhry & Ashraf, 2007) [88]. It is observed that there is always a slight increase in the stress immediately afterwards the relaxation period when the load is re-applied, which may cause an early failure after some repetitions, this may also explain the dependency on the number of relaxation periods before failure. Finally, it has been previously observed that a reduction in the total plastic strain happens when materials are exposed to tensile stress relaxation testing. (Lee & Hart, 1971) [89]

Chapter 6. Effects of Hydrogen Embrittlement in AA7040-T7651 In Microstructure.

6.1. Introduction

Understanding the effects of aqueous environments in high strength aluminium alloys 7xxx series is one of the main objectives of the present research, then comparisons between tensile tests at different humidity levels and tensile strain rates are fundamental. Hydrogen effects have been studied widely by observation and analysis of changes in the mechanical properties; however, changes in the microstructure, nucleation behaviour, crack growth and propagation are not entirely yet understood.

This chapter studies the effects of hydrogen embrittlement in the microstructure for the aluminium alloy 7xxx series AA7040-T7651 when samples are exposed to interrupted slow strain rate tensile testing until fracture. First, understanding the behaviour of the material, when tested at dry air is essential, this will be achieved through the analysis of in-situ tensile images of the polished surface to understand the pure mechanical behaviour of the material in hydrogen-free environments; the differences are then compared in samples tested at different humidity levels and exposure times. Next, observations of SEM images of the polished surfaces are quantified, and EBSD maps containing IPFs, Schmid factor and the Taylor factor around voids and cracks are investigated. Finally, a summary and discussion of the data presented are presented.

6.2. Results and discussion.

All the tests presented in this chapter were performed in aluminium alloy 7040-T7651 samples in the as-received condition; surface preparation was done as explained in section 4.2.2, then interrupted slow strain rate testing was done as discussed in section 4.2.5., in-situ and post-mortem imaging parameters are described in section 4.2.6.

6.2.1. In-situ tensile tests: Void and crack nucleation and propagation in dry air conditions.

AA7040-T7651 samples SSRT tested in dry air were studied by image acquisition during relaxation periods at different total strains until fracture. Three microstructure features are believed to be mainly involved in the deformation, and posterior damage of the

Chapter 6. Effects of Hydrogen Embrittlement in AA7040-T7651 In Microstructure material and will be defined for a better analysis understanding in the present chapter. On SEM BSE images: Intermetallic particles (IMPs) are broken particles usually arrange in clusters that are seen as white formations on top of the material surface. Voids occurred in aluminium alloys by a wide separation between grains, triple junctions and intermetallic particles and have a dark-black colour. Finally, cracks are a slight separation or sliding between grain boundaries characterised by a dark-grey colour.

Point A in figures 6-1 and 6-2 (0% total strain, 0 MPa) show little or no damage in the polished surfaces along the L-ST directions. In both figures, in points: B, 50% Yield (50% elastic strain), no cracks are present in the microstructure, however, grain boundary sliding may have occurred. Figure 6-1 displays the strain-stress curve for sample 1 tested at a strain rate of $10^{-5}\ /s$, in point C (1.23% total strain, 90% Yield), it can be noticed that damage on some intermetallic particles (IMP) started. Next, in point D at 1.82% total strain (post-yield), voids can be seen at constituent particles and deformation (probably cracks) started to develop along grain boundaries joining existing voids. Little growth of voids is observed in point E (2.29% total strain) and F (2.63% total strain) before UTS, in comparison with point D. Then, point G (3.00% total strain) shows that voids become wider, but significant changes are present in length; at this point deformation along grain boundaries is clearer. Point H (3.18% total strain) indicates considerable damage increased in comparison with point G, the growth of cracks/voids closed to second-phase clusters of particles is apparent. Finally, in the point I (3.19% total strain) at fracture, an overview of the sample in which voids and cracks joining voids are distinguished.

Figure 6-2 shows the strain-stress curve for sample 4 tested at a strain rate of $10^{-6}\ /s$, point C (1.09% total strain, 90% Yield) do not display visible damage; however, point D (1.46% total strain, 100% Yield) has two voids forming at the IMPs and a crack joining them. Next, points E (2.01% total strain, post-yield) and F (2.57% total strain) display that the lower void increased in width, also a new void nucleates in the centre constituent particle, and the left superior void do not show further growth. Existing voids in point G (3.12% total strain) stay alike; however, a new void appears in the matrix, possibly in a triple junction point. Surface damage increased significantly in point

H (3.37% total strain) closed to fracture, existing voids become wider and longer in both constituent particles and along grain boundaries. Finally, the point I (3.42% total strain) after fracture, shows an overview of the surface in which fracture is confirmed to be intergranular; also the surface presents deformation all along the surface but damage decreases as the distance from the fracture increases.

Figure 6-3 indicates the development of three zones in sample 1 during the in-situ tests; zone 1 displays some voids that might be generated in the material due to some corrosion before testing due to OPS polishing, these voids widen slightly at higher stresses, however, did not contribute to the specimen's failure. Then, at E voids nucleation occurs at particles promoting cracks formation of neighbouring grain boundaries, causing more damage than previous corrosion features. Zone 2 was previously analysed in figure 6-1. Three voids related with constituent particles are observed in zone 3 (2.29% total strain) along a grain boundary which kept widening and may promote a mayor deformation along the grain boundary, the damage of this voids seems to be just superficial.

Figure 6-4 correlates with the observed behaviour for sample 4 shown in figure 6-2, wherein zones 4 to 6 no much deformation is observed at 1.09% total strain (90% yield). Once, the specimen reaches a 2.57% total strain (post-yield) formation of voids around particles, deformation and cracks along grain boundaries are observed maybe, as a consequence of voids related with particles, also it is observed that cracks growth in length and width along grain boundaries. In zone four, it is curious that the most significant void does not initiate at an intermetallic particle; the void acquires significant dimensions even when the void develops closed to total failure. Zone 5 shows five separated voids, three of which are originated at particles, and the two smallest voids occur at grain boundaries. Finally, zone 6 has six voids that are generated at particles, voids around small particles seem to be deeper than the ones formed at bigger IMPs.

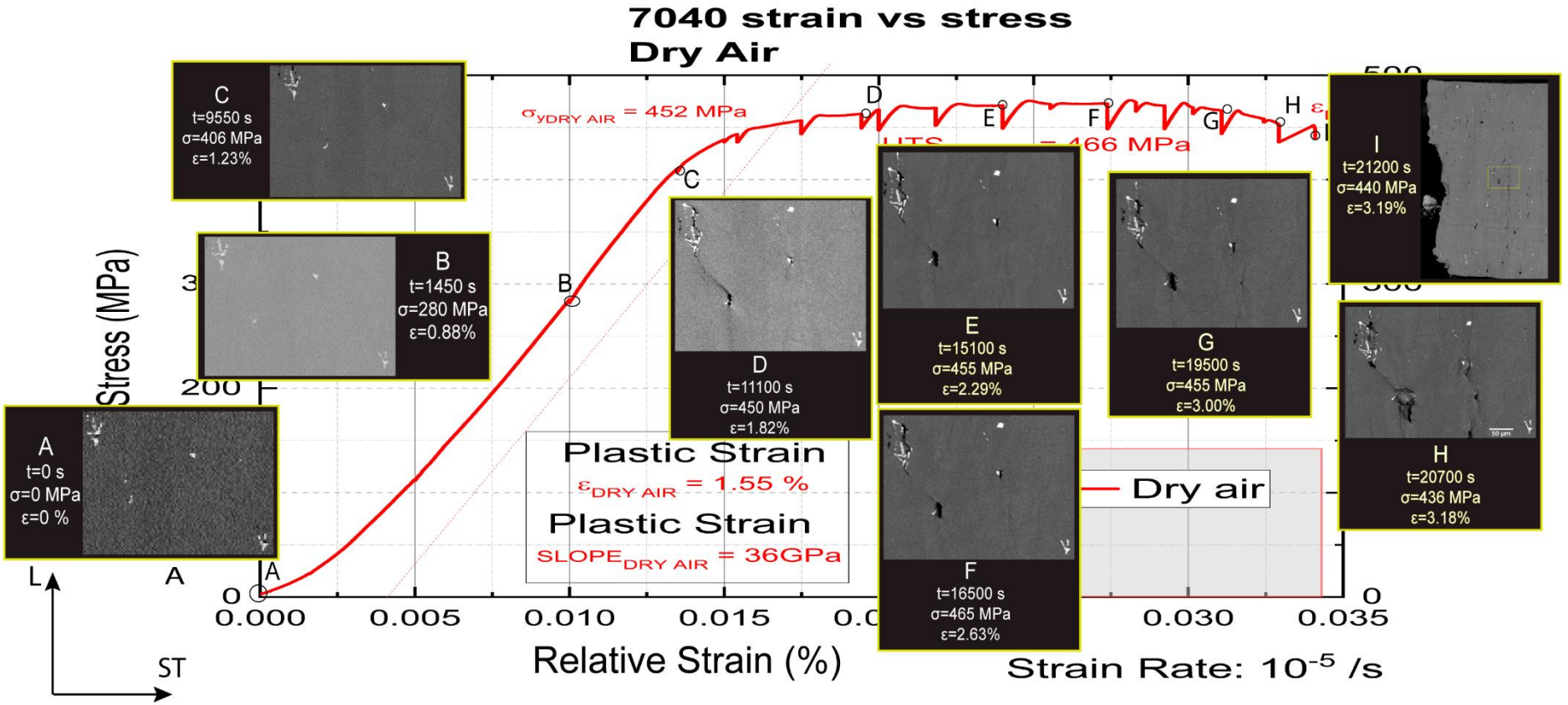

Figure 6-1. In-situ SEM images of voids and cracks development in the high strength AA7040-T7651 alloy (sample 1) during interrupted SSRT tensile testing at 10^{-5} $/s$ strain rate in dry air at different strain rates until failure.

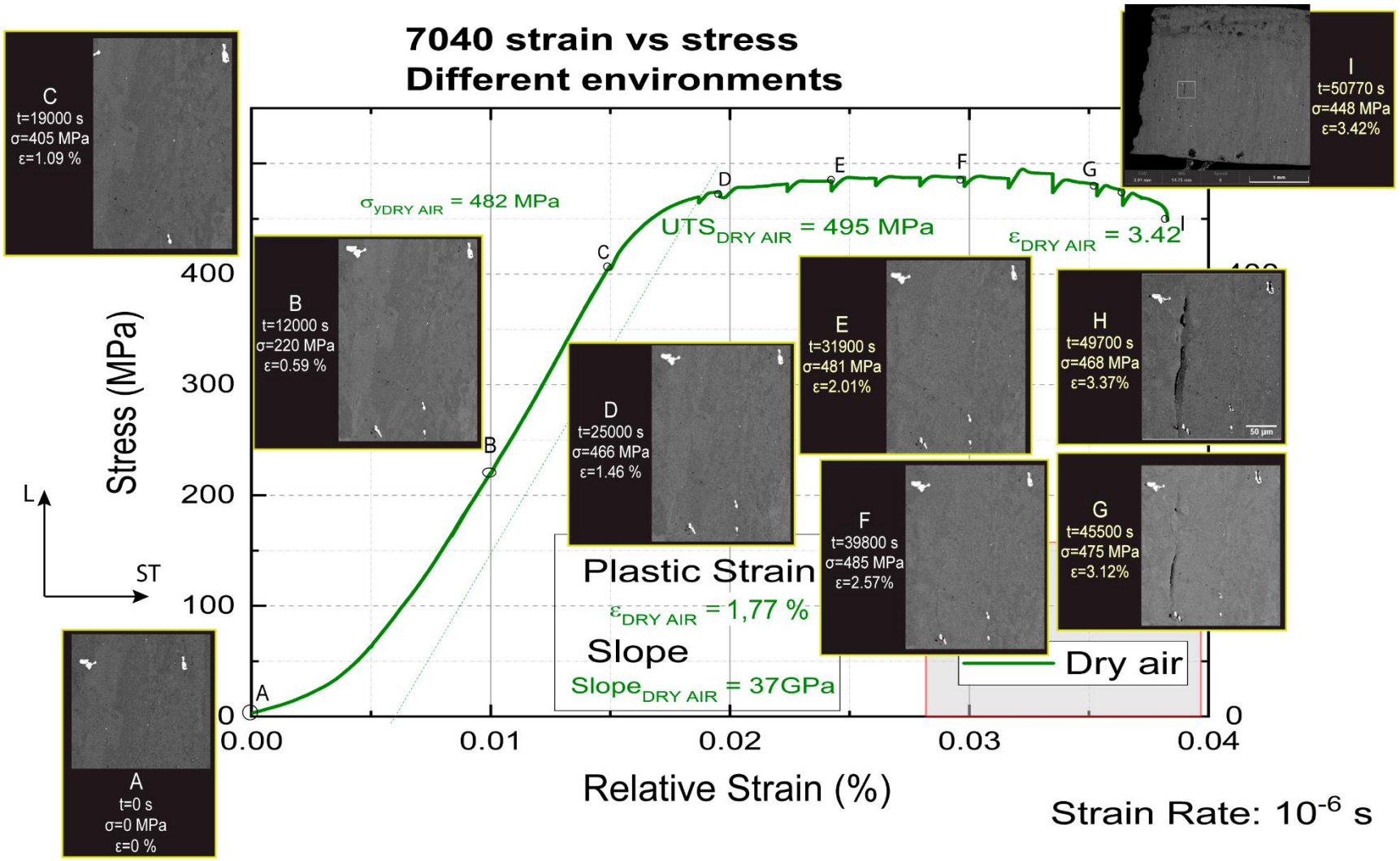

Figure 6-2. In-situ SEM images of voids and cracks development in the high strength AA7040-T7651 alloy (sample 4) during interrupted SSRT tensile testing at 10^{-6} $/s$ strain rate in dry air at different strain rates until failure.

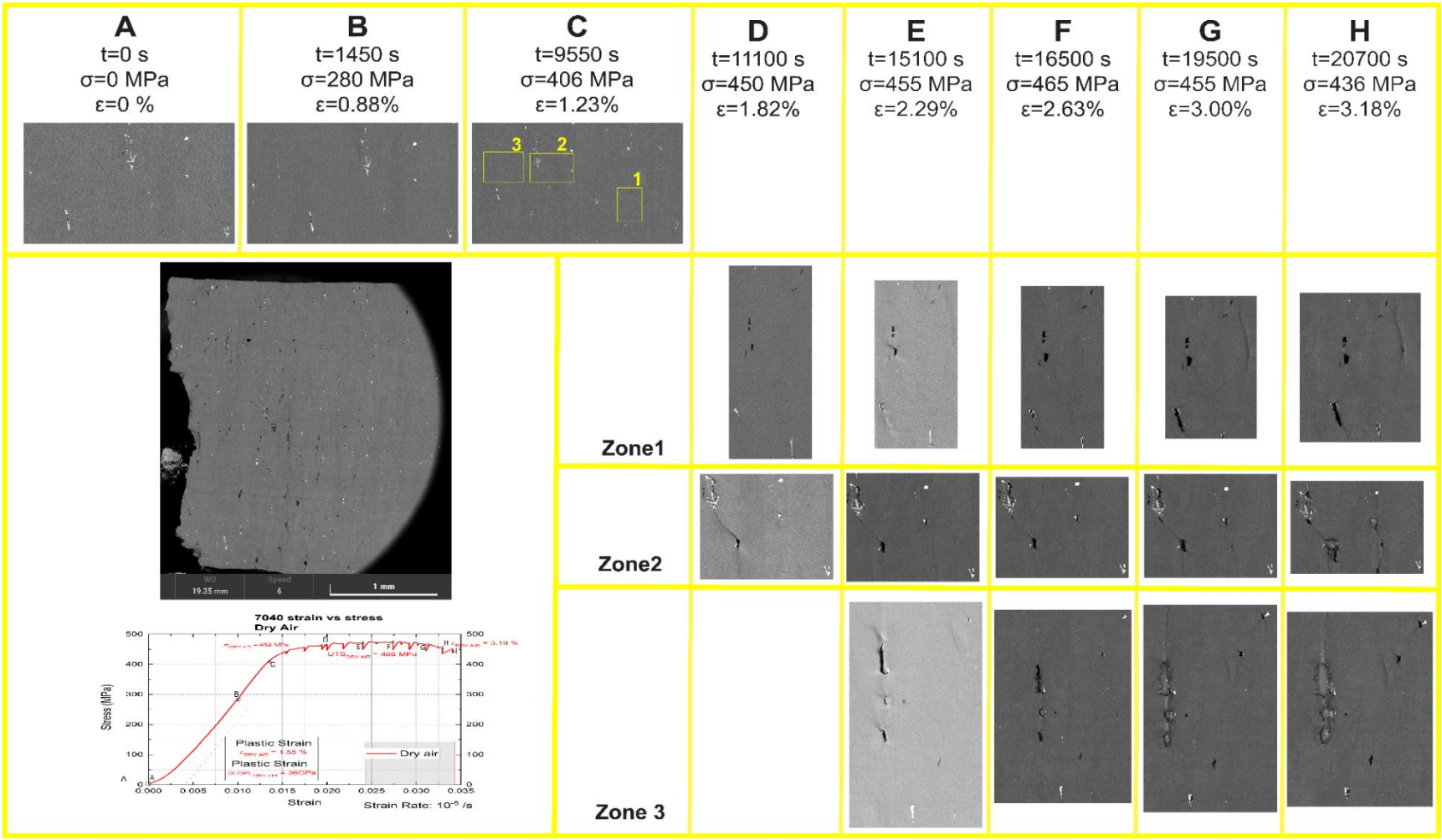

Figure 6-3. SEM images of in-situ voids and cracks development in the high strength AA7040-T7651 alloy (sample 1) during interrupted SSRT tensile testing at 10^{-5} $/s$ strain rate in dry air, for three zones of interest, at A) $\varepsilon = 0\%$, B) $\varepsilon = 0.88\%$, C) $\varepsilon = 1.23\%$, D) $\varepsilon = 1.82\%$, E) $\varepsilon = 2.29\%$, F) $\varepsilon = 2.63\%$, G) $\varepsilon = 3.00\%$ and H) $\varepsilon = 3.18\%$ total strains; also, the stress-strain curve and an overview of the polished surface after fracture are presented.

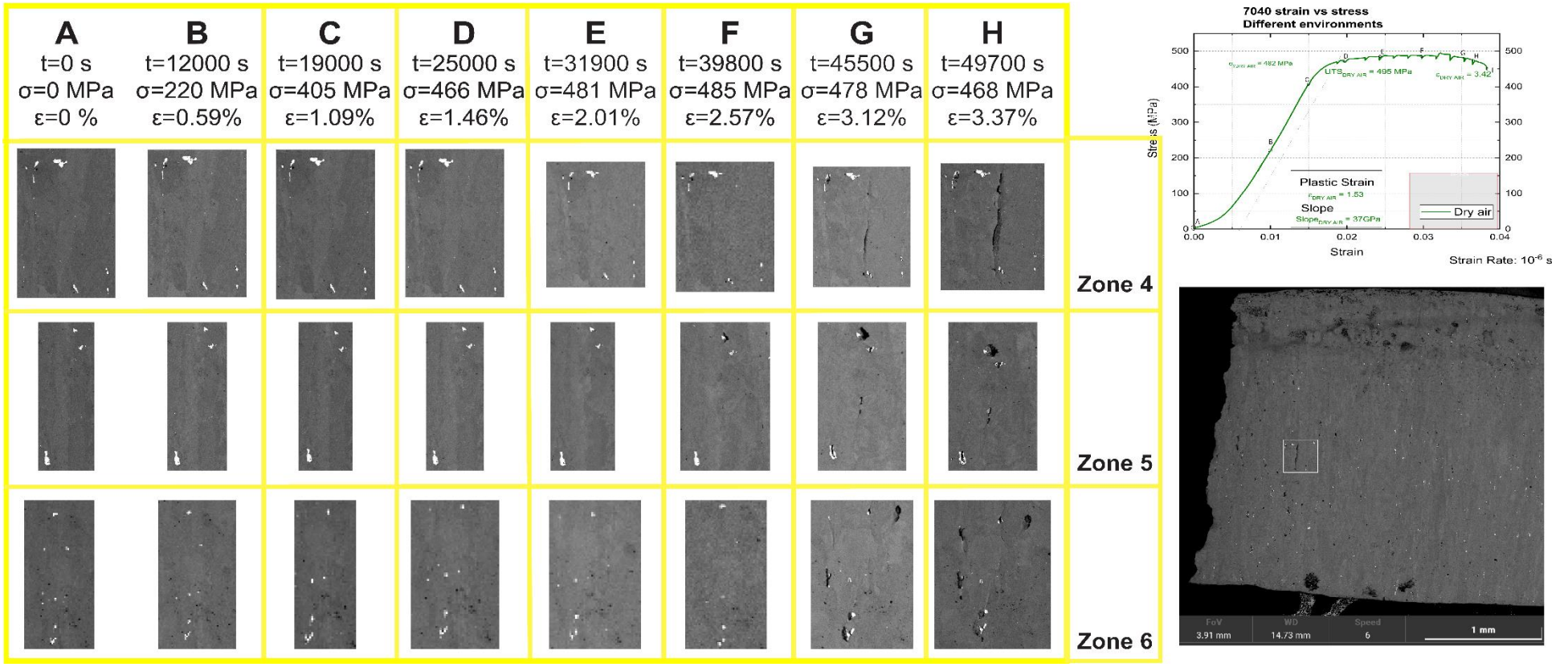

Figure 6-4. SEM images of in-situ voids and cracks development in the high strength AA7040-T7651 alloy (sample 4) during interrupted SSRT tensile testing at 10^{-6} $/s$ strain rate in dry air, for three zones of interest, at A) $\varepsilon = 0\%$, B) $\varepsilon = 0.59\%$, C) $\varepsilon = 1.09\%$, D) $\varepsilon = 1.46\%$, E) $\varepsilon = 2.01\%$, F) $\varepsilon = 2.57\%$, G) $\varepsilon = 3.12\%$ and H) $\varepsilon = 3.37\%$ total strains; also the stress-strain curve and an overview of the polished surface after fracture are observed.

i

6.2.2. Post Morten analysis: Void and crack nucleation and propagation in humid air environments.

After failure, the polished surfaces were imaged through scanning electron microscopy to analyse the possible origin of voids and cracks and determine differences between strain rates and humidity level variations. Next, it is seen that all samples present voids, cracks and visible deformation that diminishes as the distance to the fracture increases, the maximum distance at which a minimum void area of 50 um^2 will be referred in the present research as total depth of damage, and it was measured using "ImageJ" software. After fracture SEM high-resolution images were taken and then join together using the plugin "collection stitching" using the software "ImageJ" (Preibisch et al., Bioinformatics (2009)) [90]. Finally, the software "ImageJ" uses the plugin "Trainable Weka Segmentation", in which all images were classified every 250 um from the fracture surface to obtain quantitative data of the microstructural features after tensile testing under different environments and strain rate conditions.

6.2.2.1. Post-Mortem Analysis: SEM Images Dry air (Vacuum) Environment.

In figure 6-5, sample 1 is displayed, in which a) the polished surface of the specimen shows voids, cracks and considerable deformation, on b) the band contrast of the EBSD maps with the total depth of damage of 1460 um; and c) high-resolution images of points of interest. In which, void one was generated at a constituent particle, it has a depth of damage (DD) from fracture surface of 453 um, with a width (w) of 15 um and a length (H) of 147 um. The coalescence of 2 neighbouring voids forms void 2, it has a (DD) of 557 um, with a width (w) of 27 um and a length (H) of 89 um, it is not clear if these voids were formed due to the presence of particles. Void 3 is located at the inferior edge of the sample; no IMPs were found around the void, it has a DD of 711 um, a 15 um width and 58 um length. Finally, at a DD of 876 um, two voids are observed; the upper void is generated at a constituent particle and the inferior void show a small particle, this last void has 45 um width and 79 um length. All the significant voids studied on sample 1 nucleate at particles, and it seems that the size length does not have a dependence with the distance of damage from fracture.

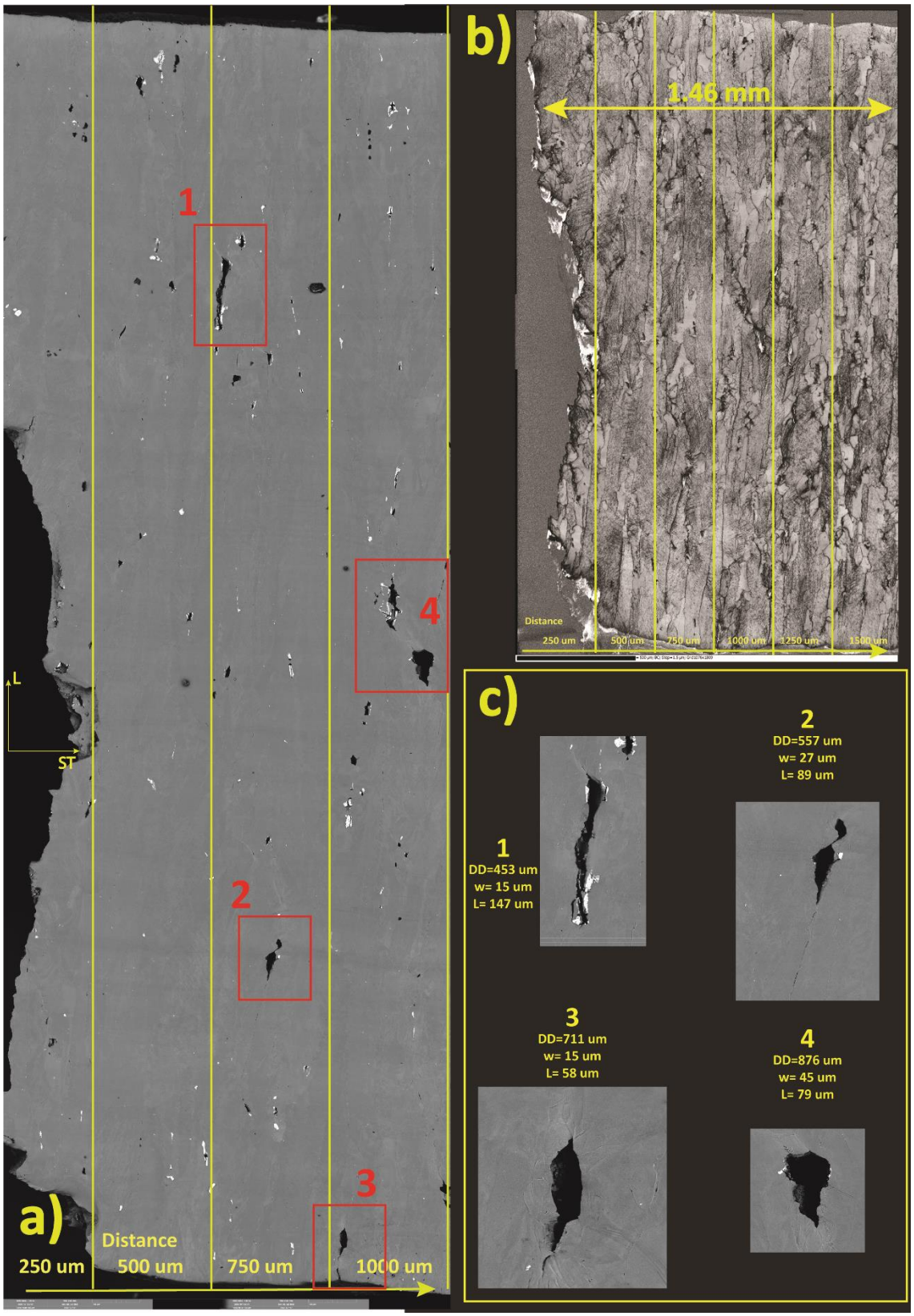

Figure 6-5. BSE-SEM images of AA7040-T7651 sample 1 tested at vacuum and $10^{-5}\ /s$ strain rate in a) an overview of the polished surface at different distances from total DD, b) band contrast of an EBSD map showing a depth of damage of 1.46 mm, and c) zones of interests damaged features at different depths displaying DD, width and length.

In figure 6-6, sample 4 is observed a) the polished surface of the specimen displays more deformation than sample 1, and the bigger voids are located close to the fracture in the centre, b) an overview shows a total depth of damage of 2123 um, and in c) the most representative damaged features. Area 1 displays damage closed to the fracture surface at a DD of 272 um, this area is formed by a string of voids with deformation along the grain boundaries The deeper voids on the left have a width and length are 21 and 57 um respectively. Area 2 shows a void closed to the superior edge, and it has a DD of 439 um, a width (w) of 24 um and a length (L) of 53 um, apparently the void initiate without the presence of particles. Next, area 3 displays a void closed to a small particle, it has a DD of 723 um, 24 um width and 42 um length. Area 4 is located in the sample centre at a DD of 805 um, a long void of 17 um width and 178 um length is formed, by the coalescence of two voids through grain boundaries without the presence of IMPs, this void was previously observed on image 6-4 zone 4. Then, area 5 at 1105 um DD shows the coalescence of voids generated at constituent particles, and there is a lot of deformation on the surrounding grain boundaries, the void has 22 um width and 67 um length. Finally, area 6 has small voids around small particles at a DD of 1429 um; the upper void is 7 um width and 18 um length.

6.2.2.2. Post-Mortem Analysis: SEM Images Humid Air Environments.

Figure A6-1 on the appendix displays sample 2 in which a) the polished surface of the specimen displays a concentration of voids in the upper left of the sample, the white-bright features on the surface are silver-paint contaminations, b) an overview shows a total depth of damage of 2209 um, and in c) high-resolution images of interesting areas; then, void 1 (DD=242 um, width (w)=30 um and length (L)=135 um) closed the superior edge) is formed at a medium-size constituent particle which then seems to grow along the grain boundary showing appreciable tearing of grains. Area 2 consists in a string of 5 voids with considerable amounts of deformation, the 2 central voids nucleate in constituent particles; however, it is not clear why the lower void growths as no presence of particles are observed, the rupture might be the result of the deformation in the adjacent grain boundaries For areas 3, 4, 6 and 9, voids are generated at constituent particles, the width and length of voids decrease with the distance from the fracture.

Finally, voids 5, 7 and 8 do not show particles on the surface; the shapes of the voids are mainly elongated with moderate cracks along grain boundaries.

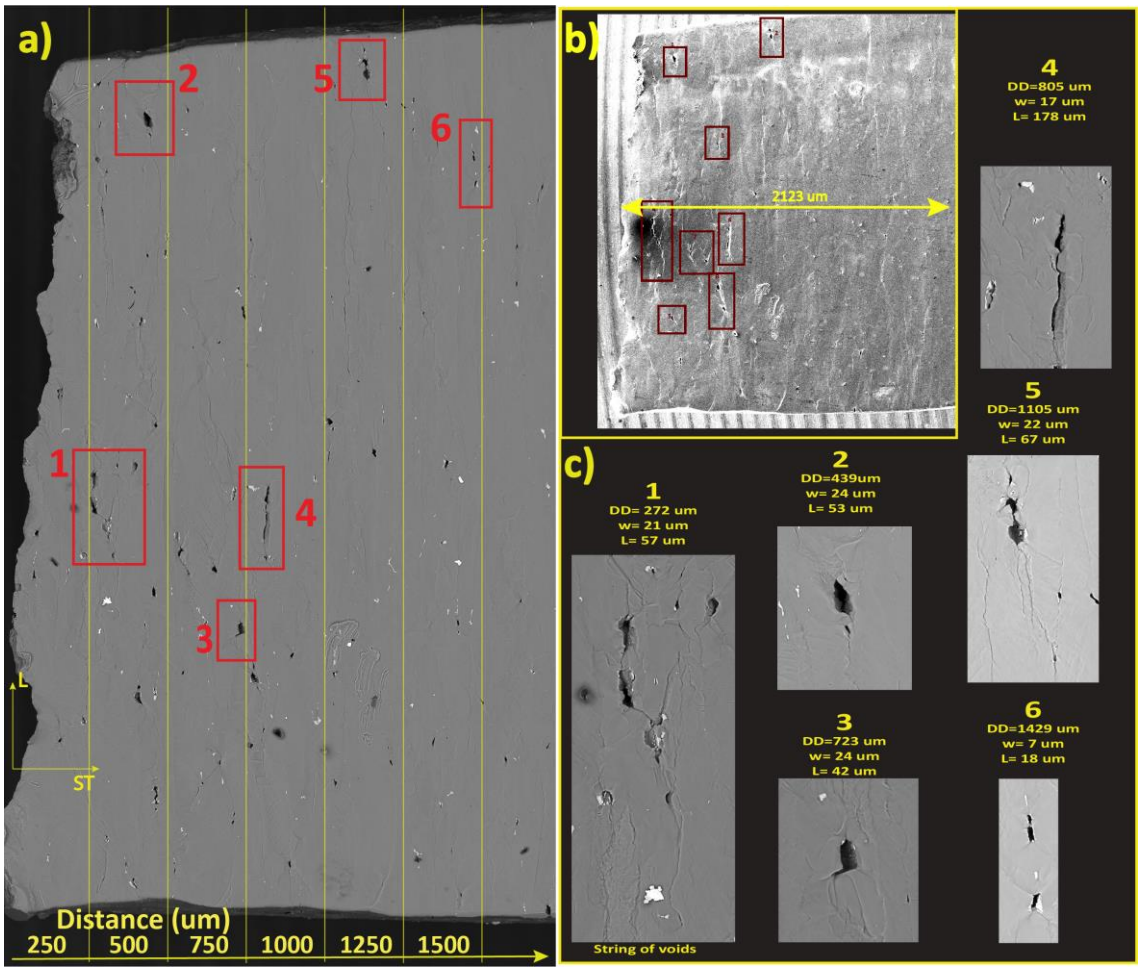

Figure 6-6. BSE-SEM images of AA7040-T7651 sample 4 tested at vacuum and 10^{-6} $/s$ strain rate in a) an overview of the polished surface at different distances from total DD, b) band contrast of an EBSD map showing a depth of damage of 2123 um, and c) zones of interests damaged features at different depths displaying DD, width and length.

Sample 3 is observed in figure A6-2, in which a) the polished surface of the specimen shows significant deformation close to the fracture surface. There is a large number of little voids at the grain boundaries in comparison with the other samples; figure 6-7 displays a BSE-SEM image acquire before testing that shows a smooth surface; then, it is believed that the mention voids are produced due to effects of high humidity (90% RH). b) an overview with a total DD of 2757 um, and in c) (dimensions on figure A6-2) Area 1 display damage closed to the edge at a DD of 175 um, two long voids are formed along grain boundaries without the presence of particles. Area two is a string of voids

 In Microstructure which are form without the apparent presence of IMPs and are elongated following the grain boundaries path, the lower void was initiated at a particle, and it can be seen that it became wide in comparison with the other void, this string is detrimental as the size is increased easily by void coalescence. Next, area 3 in the centre of the sample displays small voids, one of them closed to IMPs. Areas 4 and 5 have similar behaviour, in which one of the voids formed at particles is joined to the other void through a crack along the grain boundaries between voids. Then, along grain boundaries in areas 6 and 7 there is a string of cracks join by small voids, it may be that theses long features were formed by the coalescence of multiple voids along the grains. Finally, areas 8 and 9 show voids at big distances from the fracture surface; however, deformation and cracks along the grain boundaries are still observed, contrary with previous samples behaviour were at a depth of 1300 um no much deformation is observed. The width of cracks and voids generally decreases as they get far away from the edge.

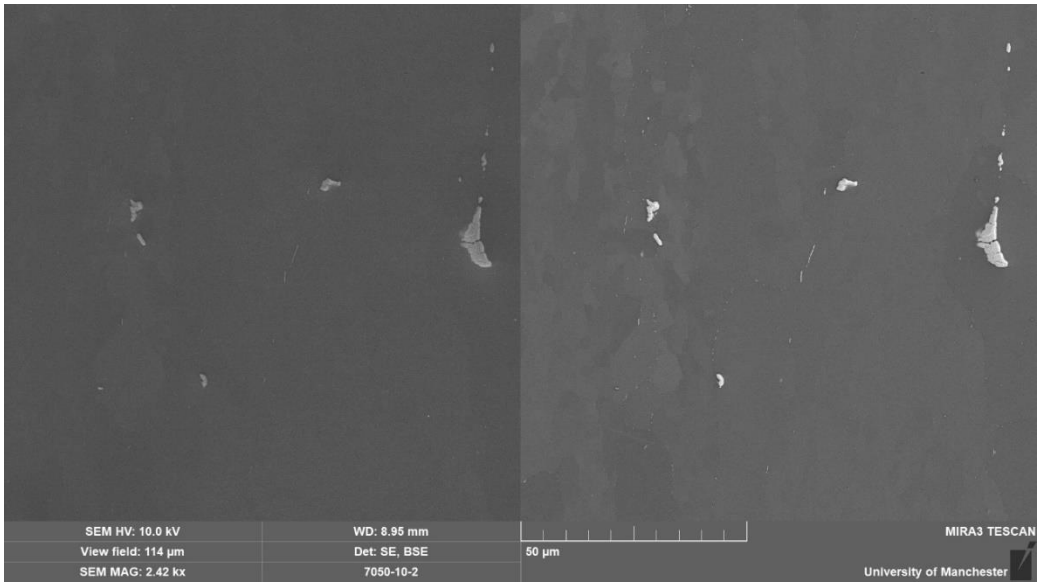

Figure 6-7. BSE-SEM image of sample 3 after polishing, and before tensile testing at high humidity. After this step, the surface is smooth, with no apparent corrosion products on the surface.

For sample 5 tested at 50%RH at a strain rate of $10^{-6}\ /s$, figure A6-3 shows a) the polished surface shows maximum deformation in the lower-left area b) the total depth of damage is 2384 um, and c) areas of interest (dimensions show in figure A6-3). Area 1 has a shallower void which formed at a wide-size particle. Area 2 is of great importance,

as it has a length of 276 um (~10% of the sample width) and it shows voids join by cracks, which probably growth due to void coalescence. Next, area 3 presents a void initiated at particles which acquired a significant length apparently by joining a neighbouring void. Void 4 nucleates at IMPs and it seems that the void was torn along the grain boundary, also some little voids are observed in the surrounding grain boundaries. Then, area 5 located at the bottom of the sample shows the formation of the void around a constituent particle; however, along the grain boundaries around the void, large deformation is observed. Area 6 at a DD of 1203 um shows voids with big constituent particles around them but not much widening of growth is observed. Finally, area 7 has a void in the centre-part that is formed around constituent particles, however, despite being considerably away from the fracture surface, it still shows high deformation around it and big cracks along the neighbouring grain boundary.

The total depth of damage for all samples can be observed in table 6; it is evident that as humidity content increases and the strain rate decreases the total depth of damage increments; this tendency can be observed in samples one to three, in which the total depth of damage increases from 1460 um to 2757 um when humidity increases from 0 to 90% RH, and when the strain rate decreases (10^{-5} $/s$ to 10^{-6} $/s$) in samples 1 and 4, the depth increases from 1460 um to 2123 um. Most voids are mainly initiated at constituent particles independent of the humidity levels; however, more deformation at grain boundaries and an increase in the number of voids is seen when the strain rate decrease as the humidity levels increases. The size and number of the voids seem to be independent of the distance to the fracture surface, and this may suggest that the increase in voids number when the humidity contents raise, clearly states embrittlement that affects voids and cracks development. For instance, sample 3 display a string of little voids at grain boundaries, such effect is only observed under a high humidity environment (90%RH), then atomic hydrogen might be concentrating at grain boundaries and crack tips causing a detrimental effect on the material response to deformation.

Table 6-1. Total Depth of damage (DD) for all samples after tensile testing for AA7040-T7651 when they are exposed to different humidity levels and strain rates.

Sample	Total Depth of Damage (um)
1 Dry Air Strain Rate: $10^{-5}\ /s$	1460 ± 9
2 50 % RH Strain Rate: $10^{-5}\ /s$	2209 ± 9
3 90 % RH Strain Rate: $10^{-5}\ /s$	2757 ± 9
4 Dry Air Strain Rate: $10^{-6}\ /s$	2123 ± 9
5 50 % RH Strain Rate: $10^{-6}\ /s$	2384 ± 9

6.2.2.3. Post-Mortem Analysis: Microstructural features at different environments.

A quantitative analysis is performed through the segmentation of four microstructural features (matrix, cracks, intermetallic particles (IMPs) and voids). The segmentation was performed using the plugin "Trainable Weka Segmentation" of "ImageJ" software, in which for each sample the features assigned as explained: Intermetallic particles are observed as white particles with random shapes located all around the surface, cracks are areas characterized by deformation which may cause gliding between grains, little or no separation of grains occurred. Voids are areas where the separation between grains or in the particle/matrix interface are produced, and finally, the matrix is the surface inside grains. For the segmentation analysis, all samples were divided into sections of 250 um width starting at the fracture surface; then, each section was classified as shown in figure 6-8. First, the original BSE-SEM image was classified into voids, IMPs, cracks and matrix as previously explained; Images in grey-scaled are generated for each feature these are known as "probability maps", afterwards images are transformed into an 8 bits format and thresholded following the same parameters for all samples. Finally, the results are generated, and features with areas greater than 25, 6, and 25 um^2 were discarded to avoid noise and reduced errors during the process.

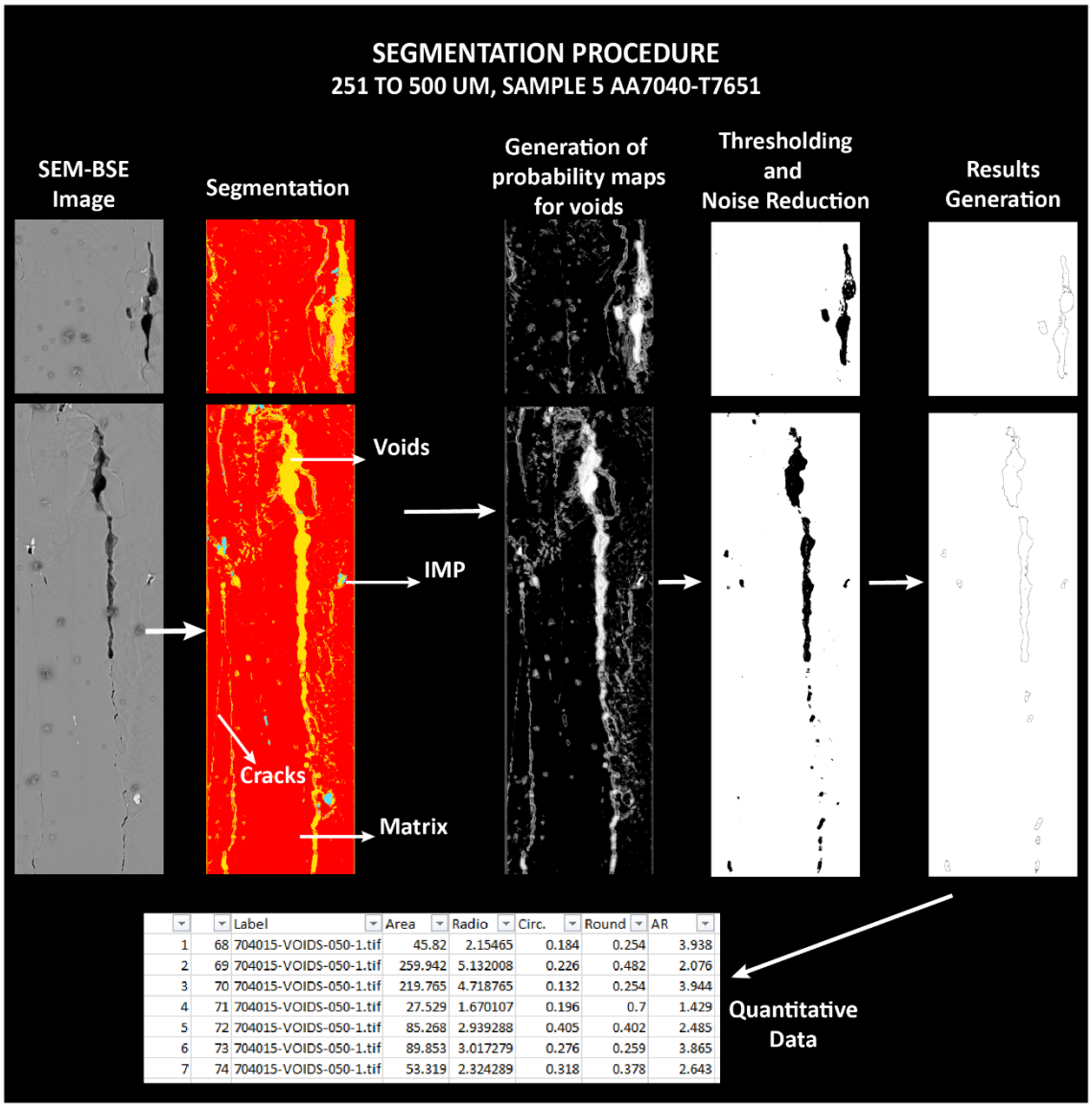

		Label	Area	Radio	Circ.	Round	AR
1	68	704015-VOIDS-050-1.tif	45.82	2.15465	0.184	0.254	3.938
2	69	704015-VOIDS-050-1.tif	259.942	5.132008	0.226	0.482	2.076
3	70	704015-VOIDS-050-1.tif	219.765	4.718765	0.132	0.254	3.944
4	71	704015-VOIDS-050-1.tif	27.529	1.670107	0.196	0.7	1.429
5	72	704015-VOIDS-050-1.tif	85.268	2.939288	0.405	0.402	2.485
6	73	704015-VOIDS-050-1.tif	89.853	3.017279	0.276	0.259	3.865
7	74	704015-VOIDS-050-1.tif	53.319	2.324289	0.318	0.378	2.643

Figure 6-8. Example of segmentation procedure for the quantitative analysis of voids, cracks and IMPs size, aspect ratio and roundness using the software "ImageJ". First, the BSE-SEM image is classified into voids, cracks, IMPs and matrix, next a grey-scaled imaged is generated that subsequently is thresholded and the results are generated discarding the smallest features to avoid noise.

A detailed illustration of the classifier can be found in figure 6-9; the segmented images are shown on the left, accompanied by the original high-resolution BSE-SEM image on the right. In section a, the segmentation is a 96% correctly identified; however, some areas that surround voids (pointed by the yellow arrow) are classified as IMPs(light blue), and some particle/matrix interfaces were detected as cracks, these errors are minimum, and they are eliminated in the last step of the segmentation process.

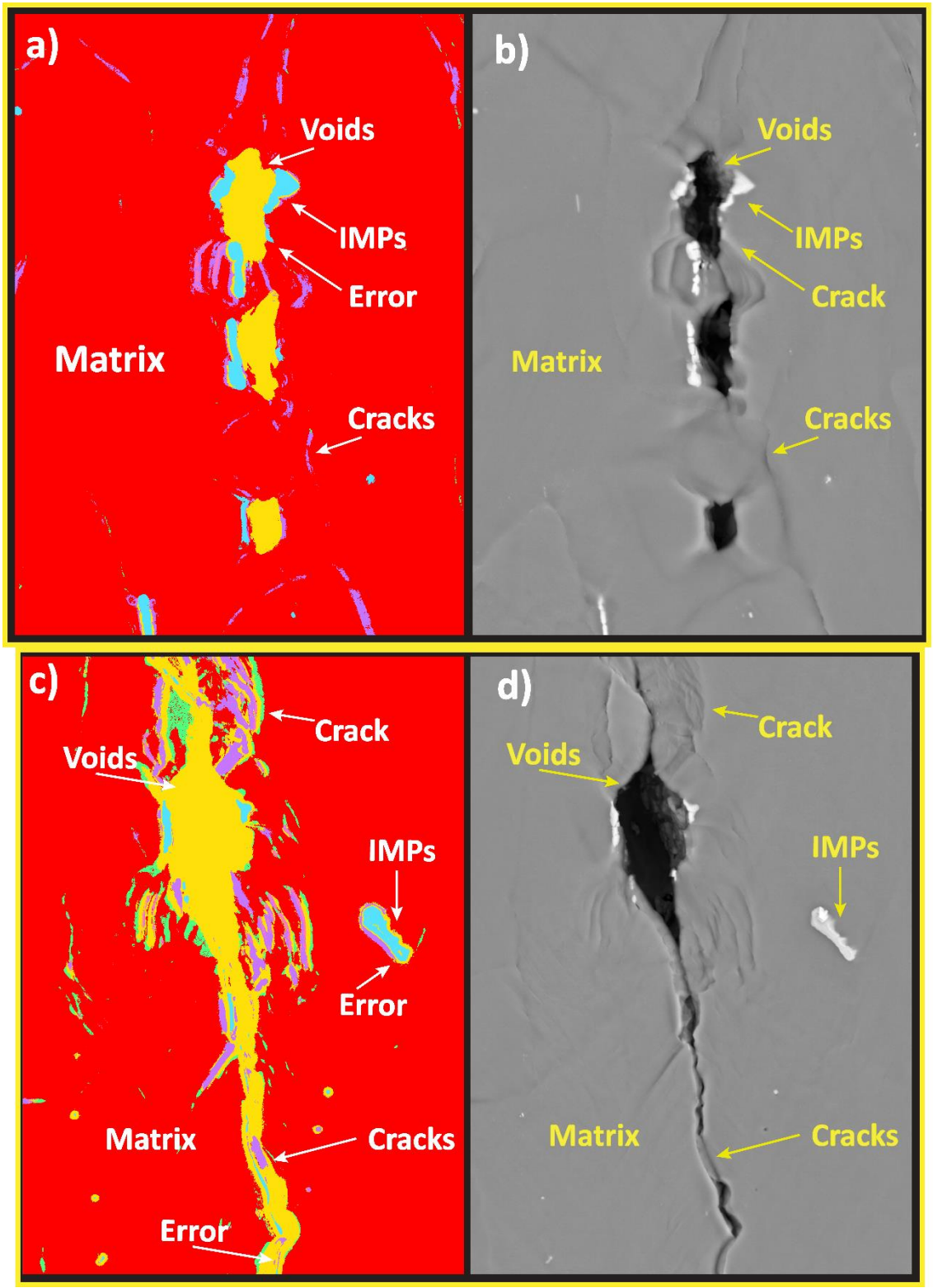

Figure 6-9. Segmentation illustration showing a detailed segmentation of microstructural features for sample 5 AA7040-T7651, the segmented image may be found in the left with the original BSE-SEM image on the right. In a) voids are correctly identified however the errors include particle/matrix interfaces and voids edges, and for b) voids in cracks look thicker than usual, in total error is lower than 4%.

In figure 6-9 section c, the segmentation of microstructural features is accurate with small errors pointed in yellow. First, thin cracks are detected in particle/matrix interfaces, small IMPs are recognized as voids; finally voids joined by cracks formed along grain boundaries are thicker than usual, after thresholding and noise reduction the total error in the segmentation process is lower than 4%. Finally, BSE-SEM images were obtained at different parameters, as explained in section 4.2.6; for this reason, it was necessary to understand if the segmentation process was affected by the changes in image acquisition. Then, the plot profile analysis of features with the similar characteristics are presented in figure 6-10; in which microstructural features with similar characteristics were analysed and it was seen that voids profiles have similar behaviour (the grey-scaled drops down to zero); for IMPs the matrix present different grey-scale; however, the IMPs behaviour is alike and show that the plot raises in both samples. Finally, cracks display a similar tendency in which at the crack the plot drops down close to 80; It is finally concluded that differences in image acquisition do not affect the final segmentation significantly as small features present similar characteristics.

A summary of the microstructural feature characteristics for samples tested in dry air (table 6-2), in all samples microstructural features were assumed as circles for the radio and roundness computation. For samples 1 and 4 voids present a similar number, size, aspect ratio and roundness. Sample 4 displays more intermetallic particles; however, the size, roundness and aspect ratio keep the same behaviour. The number of cracks increases by 35% when the strain rate decreases; this can be explained as a material tested at slower strain rates have more deformation; cracks are a 30% smaller and 25% sharper in sample 1.

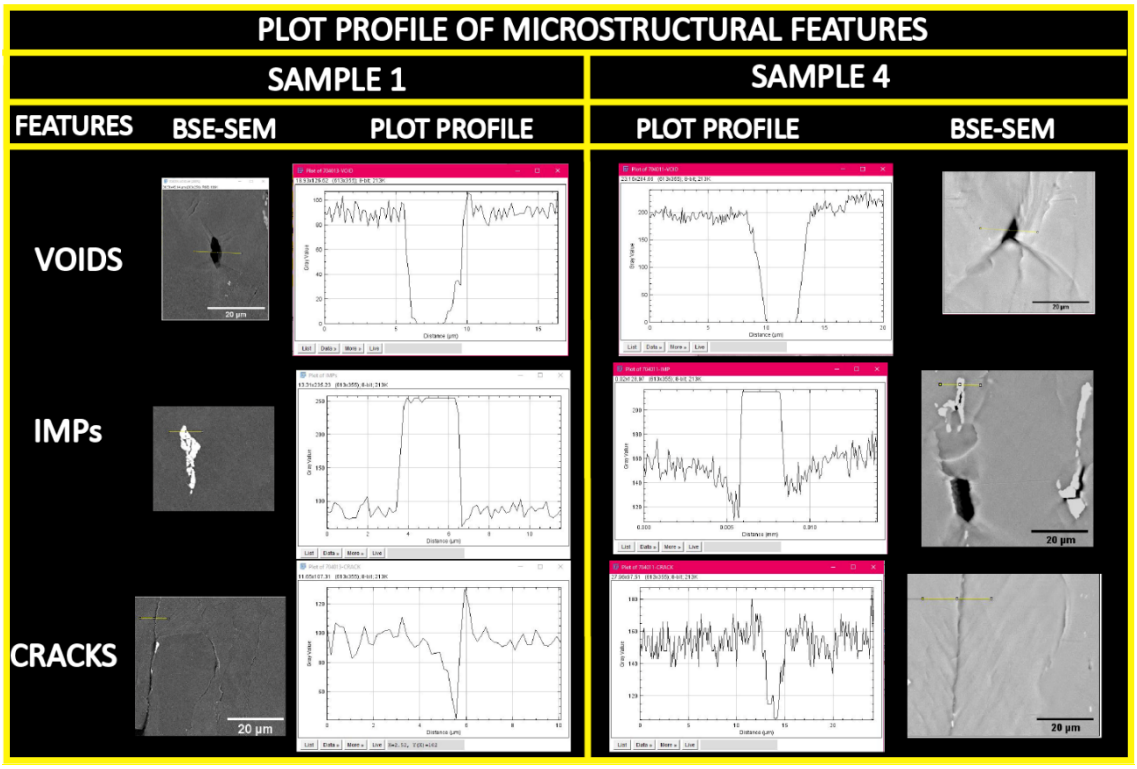

Figure 6-10. Plot profile analysis of microstructural features (voids, cracks and IMPs) of similar characteristics to discard errors in segmentation due to different acquisition parameters.

Table 6-2. Microstructural features (voids, IMPs and cracks) characteristics (roundness, radio (um) and aspect-ratio) in the polished surface after interrupted SSRT for AA7040-T7651 samples tested in dry air at different strain rates.

Microstructural Features	Characteristics	Sample					
		1			4		
		Total Results		ST. DEV.	Total Results		ST. DEV.
		Number	Size		Number	Size	
Voids	Round	103	0.48	0.22	104	0.46	0.19
	Radio (um)		3.35	2.22		3.19	1.45
	AR		2.85	1.94		2.70	1.89
IMP	Round	59	0.54	0.17	76	0.54	0.17
	Radio (um)		1.7	0.55		2.03	0.53
	AR		2.08	0.74		1.9	0.64
Cracks	Round	306	0.2	0.14	471	0.26	0.15
	Radio (um)		2.21	0.75		3.30	2.74
	AR		7.12	3.87		5.37	3.06

In table 6.3, when comparing samples 2 and 3 tested at the same strain rate, the number of voids increased by 7%, the roundness and aspect ratio indicates that voids in sample 3 are 27% sharper than sample 2 voids; however, the size of the voids decreases considerably for sample 3. The number of cracks increases by 35%, cracks size is 21% bigger, and the aspect ratio decreases by 10% for sample 3. Then, when comparing samples 2 and 5 tested at different strain rates but with the same humidity level, it is observed that the number of voids, void size, aspect ratio and roundness are very similar, the number of cracks increases by 40% in sample 5 and the cracks size, roundness and aspect ratio keep the same tendency in both samples. Finally, for intermetallic particles in all samples, the number of IMPs, roundness, radio and aspect ratio have similar characteristics.

Table 6-3. Microstructural features (voids, IMPs and cracks) characteristics (roundness, radio (um) and aspect-ratio) in the polished surface after interrupted SSRT for AA7040-T7651 samples tested in different humidity levels (50%RH and 90%RH) at two different strain rates.

Microstructural Feature	Characteristic	Sample								
		2			3			5		
		Total Results		ST. DEV.	Total Results		ST. DEV.	Total Results		ST. DEV.
		Number	Size		Number	Size		Number	Size	
Voids	Round	168	0.43	0.2	180	0.34	0.19	165	0.41	0.19
	Radio (um)		3.35	3.05		2.44	0.77		3.16	1.85
	AR		3.00	1.61		4.09	2.86		3.17	1.72
IMP	Round	72	0.58	0.17	87	0.53	0.19	73	0.53	0.19
	Radio (um)		1.79	0.53		1.94	0.65		1.92	0.73
	AR		1.9	0.65		2.14	0.82		2.16	0.78
Cracks	Round	311	0.19	0.14	480	0.19	0.14	509	0.23	0.18
	Radio (um)		2.27	0.81		2.86	1.29		2.48	1.24
	AR		8.19	4.86		7.37	4.56		8.13	5.71

When comparing samples tested at the same strain rate and different environments; For samples 2 and 5, it is observed that the number of voids increased by 40% than samples 1 and 4 respectively. In sample 2 voids are a 10% sharper than voids generated at dry air, the number of cracks increased slightly by 6%; however, the roundness and aspect ratio indicates that voids are a 13% sharper; the number of cracks increases only by 6%. For samples 4 and 5 the voids radio is the same and voids gets sharper when

tested in lab-air, the cracks became smaller and 34% sharper; finally, the number of cracks varies just in 7%. The analysis of samples 1 and 5 displays a 43% increase in the voids number; the voids are small but, 30% sharper; the number of cracks increased by 36%, cracks are longer and also present sharper characteristics.

From this results, it can be seen that as humidity increases the number of voids increases considerably (40%) while the number of cracks changes slightly (6%), voids and cracks tested at humidity became sharper as humidity levels increments. Interestingly, the differences in the voids number and characteristics change slightly when tested in dry air at different strain rates but present significant differences when humidity increases (40% more voids), cracks number augment lightly however they became 34% sharper than sample 1 tested in vacuum. Detailed information and statistical figures can be found on the appendix from figure A6-4 to A6-8 and tables A6-1 to A6-5, in which the microstructural features characteristics, every 250 microns are observed for all samples.

It is clear that when humidity increases, the nucleation of voids plays an essential role in the failure of the material; figure 6-11 shows the radio distribution and aspect ratio statistical curves of voids for all samples. It is important to notice that voids in sample 3 have smaller radio dimensions than sample 1; however sample 3 has 82 voids which size is between two and three um although it has 13 more voids with a size: 3-4 um than sample 1, the same tendency is observed for sample 5 which shows 107 voids smaller than two microns, but it has 25 voids of 3-4 um radio, and 33 voids bigger than 4 um; also, sample 2 displays 39 voids larger than 4 um when sample 1 only has 23 voids. The aspect ratio (AR) has the same tendency as expected; there is a high concentration of voids with an AR smaller than 3 for all samples, samples 2, 3 and 5 present a high frequency of voids with an AR smaller than 3 when compared with samples 1 and 4, this may be explained because small voids have small aspect ratios as they are almost round; this will be in accordance with the number of small voids observed in a), in the end, the total results do not display the behaviour of larger voids accurately for samples 2, 3 and 5. It is observed that sample 3 has more voids with an aspect ratio larger than 4 um, followed by sample 5 and sample 2 subsequently. On c) the curve presents the number of voids vs the depth of damage from the surface, it is evident that sample 3 has a

considerably increased in the number of voids along the whole surface when compared with the other samples; samples 2 and 5 have similar behaviour; however, there is a drop in the sample 5 curve at 750 um depth of damage, which is not entirely understood, it might be strongly related with microstructural features such as recrystallised grains or grain orientation. Finally, samples 1 and 4 have a lower increase in the number of voids when the depth of damage increases.

In figure 6-12 the analysis of statistical graphs is observed for all samples, the radio of cracks smaller than 3 um is high for all samples; cracks radios between 1-2 um are more frequent in sample 3, while crack radios of 2-3 um are higher for sample 2. When comparing crack voids bigger than 3 um, it is clearly seen that sample 3 and 2 has 76 and 249 cracks respectively when Sample 1 only has 39 cracks of this dimension, and sample 5 has 103 cracks compared with 123 cracks from sample 4, this last results seem contradictory but is not reflecting that sample 5 has more total cracks than sample 4, but they are smaller than 3 um. The aspect ratio analysis indicates that all samples have the aspect ratio evenly distributed. Finally, a curved of the total number of cracks vs depth of damage is provided, in which sample 5 displays the mayor growth of cracks, samples 3 and 4 shows a similar growth behaviour. However, sample 2 shows an increase in the number of cracks that reduces significantly at 750 um, this behaviour is not entirely understood, but it might be attributed to the true stress in the material at 750 um from the fracture surface. While sample 1 has the fewer number of cracks which is in accordance with the polished surface observed which did not display much deformation around voids in comparison with the other samples.

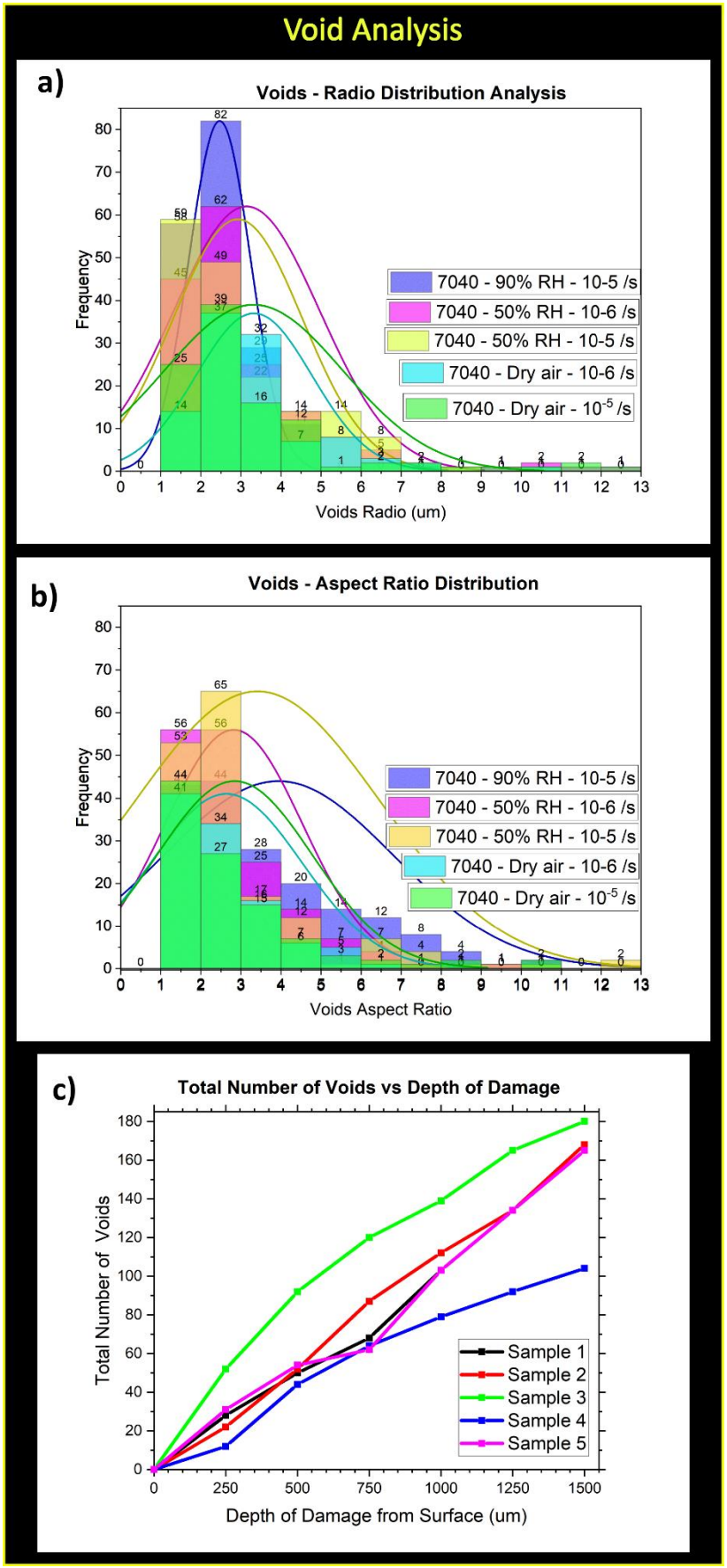

Figure 6-11. Void analysis for AA7040-T7651 samples, in which a) detailed statistical figure of voids radio vs frequency, b) statistical figure of voids aspect ratio vs frequency and c) the number of voids vs depth of damage from the surface curve is observed for all samples.

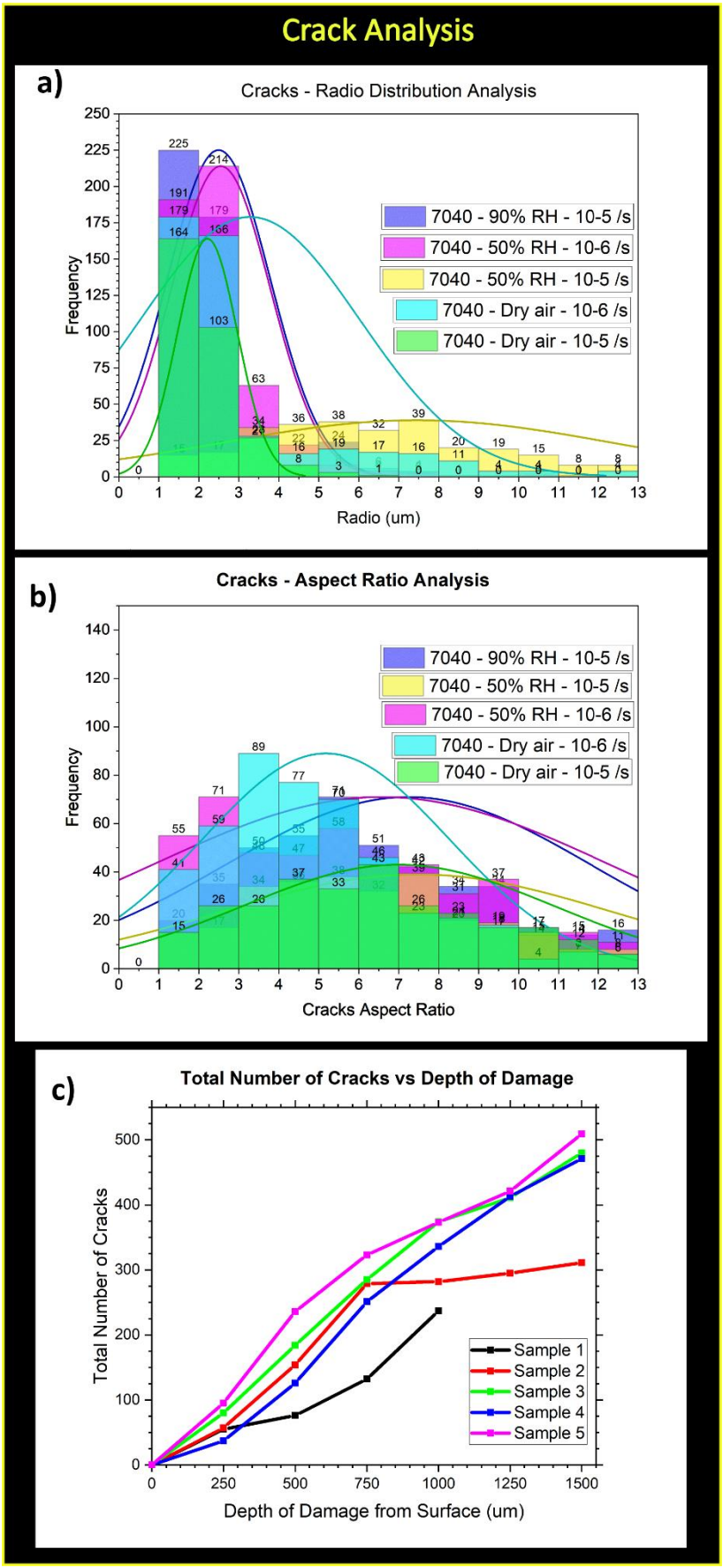

Figure 6-12. Crack analysis for AA7040-T7651 samples, in which a) detailed statistical figure of cracks radio vs frequency, b) statistical figure of cracks aspect ratio vs frequency and c) the number of cracks vs depth of damage from the surface curve is observed for all samples.

The voids and cracks number seem to be strongly influenced by the humidity levels of the material and exposure times to the environment. The number of voids increased up to 40% when the humidity increases from 0 to 90%RH; however, voids seem to be smaller and not to sharp for sample 3 as it was at dry air. Then, when the detailed information was analyzed, samples 3 and 2 have bigger and sharper voids than sample 1; this unexpected result was not easy to determine as there was a significant number of small voids. Moreover, these samples have bigger voids in a mayor quantity than sample 1, which is not easily seen when analysing the general data of the sample. It is interesting to notice that humidity composition in the air plays a critical role when compared with exposition times, sample 4 is more affected by humidity than sample 2 however is not as affected as sample 5 even when the time of exposure was two times longer.

In figure 6-13, BSE-SEM images with an area of 500*600 um were taken for all samples in the centre of the specimen closed to the fracture surface; this was done to compare the differences in the deformation when different humidity levels and different strain rates are applied. The yellow arrow in the images indicates the areas in which there is a separation between grain boundaries known in the present work as “medium-cracks”. It was observed that the deformation and separation of cracks increased with the humidity levels, this can be easily seen when comparing sample 1 and 2, in which sample 2 has 16 voids separation while sample 1 only has one; the same tendency occurred for samples 4 and 5, confirming that as the humidity increases the number of separations raises. This behaviour is also affected by changes in the strain rate, for instance, between samples 1 and 4, the number of separation increases slightly from 1 to 4 when the strain rate decreases and this little increased is observed between samples 2 and 5 with an increment of two. Finally, it can be said that the deformation around cracks is then mainly affected by humidity contents in the air.

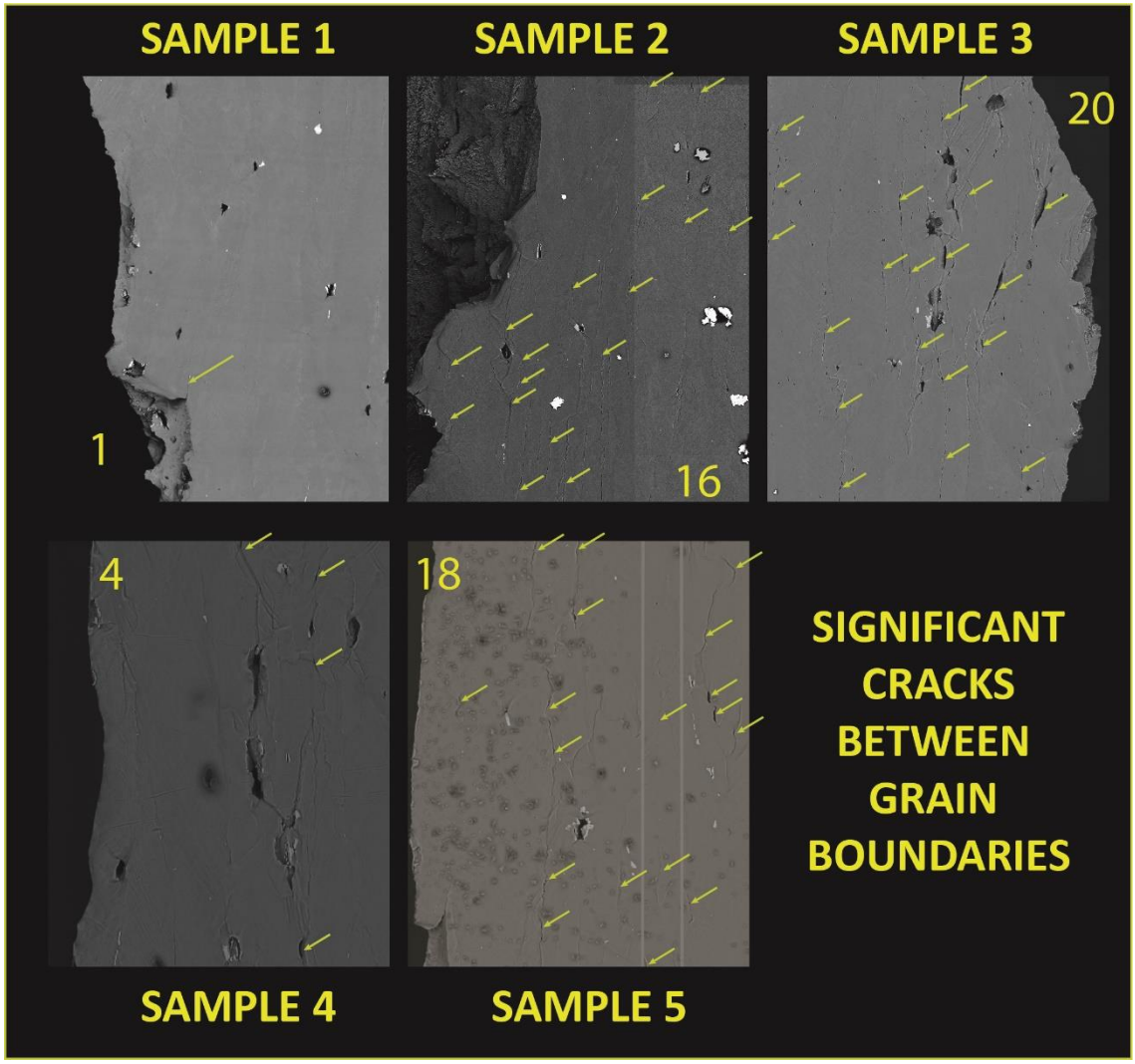

Figure 6-13. BSE-SEM images with an area of 500*600 um taken for all samples in the centre of the specimen closed to the fracture surface, in all samples yellow arrows indicate medium-cracks (separations between grain boundaries) for all samples tested at interrupted SSRT in the alloy AA7040-T7651.

6.2.2.4. Post Morten Analysis: Electro Backscattering Diffraction (EBSD)

Electron Backscattering diffraction maps of the polished surface were taken before and after tensile testing for samples 1 to 3 (same strain rate: $10^{-5}\ /s$ and different humidity levels). In this section, Inversed poled figures (IPF) in the z-direction, Schmid Factor in the easy slip system ({111} plane and $< \bar{1}10 >$ direction) and Taylor Factor will be analysed for the most significant voids. For each area analysed, EBSD data before and after fracture will be provided, cracks and voids are represented with white lines for better interpretation on the before-EBSD maps. Finally, all maps were generated with "Tango" software, the scale for Schmid and Taylor Factor can be found in table 6-4.

Table 6-4. Schmid and Taylor factor numerical scale for EBSD maps analysis in the present research.

Schmid Factor	Value	Taylor Factor	Value
Blue	0	Blue	2.4
Green	0.2	Green	2.8
Yellow	0.3	Yellow	3.2
Orange	0.4	Orange	3.4
Red	0.5	Red	3.6

Figure 6-14 displays the EBSD results for sample 1 (Vacuum), in which void 1 occurs at triple junctions due to the presence of particles, in the IPF map void formation occurs between recrystallised grains with different orientations and a non-recrystallised with a {111} plane orientation, the void occurs when there are 0.2 Schmid factor variations, and Taylor factor has a variation of 1, and it is observed that the crack is arrested in the top part of the void, maybe because the top grains are not favourably oriented. Then, void 2 grows between non-recrystallised grains without the apparent presence of particles, the IPF shows that grain separation happened between blue (easy slip - {111} plane) and green ({101} plane), the Schmid factor variations are lower than 0.1, and the Taylor factor has a variation of 0.8. Area 4 consist of 2 voids, the superior void is narrow and nucleates at IMPs, the IPF indicates that cracks nucleates between blue (easy slip - {111} plane) and green ({101} plane) recrystallised grains, the Schmid factor and Taylor factor are 0.2 and 0.8 respectively. On figure 6-15, void 5 occurs at particles with triple junctions between recrystallised and non-recrystallised grains, and it occurred at 555 um from the depth of damage and the changes in Schmid and Taylor Factor are 0.1 and 1 respectively. Finally, void 6 occurs at 485 um from the surface and has 214 um^2 area, and it occurs at a triple junction without any particles between recrystallised and non-recrystallised grains. It is interesting to notice that the change in Schmid Factor is just 0.1 while the Taylor factor variates in 0.4, which is a relatively small value compared with the other areas examined for sample 1.

For sample 2 (50%), six voids will be analyzed and can be found in figures 6-16 and 6-17; First, area 2 displays a string of voids with a similar area that will be analysed in 3 parts:

a) the superior void nucleates between recrystallised (RG) and non-recrystallised grains (NRG) without the presence of particles between non-easy slip planes the Schmid factor variation is 0.1 and the surprisingly the Taylor factor is only 0.2; b) the central voids nucleated at a triple junction with particles between RG and NRG the Schmid factor variation is 0.6; then c) the inferior void occurs without the presence of particles between NRG and RG when the Taylor factor is also 0.6. Areas 4, 12 y 13 have voids that growth at particles, triple junctions between RG and NRG between and non-easy slip planes, the Taylor factor variations range from 0.8 to 0.2. Area 10 consist of a void with cracks in the lower part along grain boundaries without the presence of particles at triple junctions, IPF reveals that the void nucleates between recrystallised grains, in which the separation occurs in {111} plane grains non-easy slip grains, the Schmid factor changes slightly, but the Taylor factor has a variation of 0.4 only. Finally, area 11 voids were initiated in areas with no particles closed in the surface between RG and NRG, the separation occurs between non-easy slip planes, Schmid and Taylor factor variations are 0.1 and 0.8 respectively.

Figures 6-18 and 6-19 display the EBSD results for sample 3 (90% RH), area 1 indicates various voids form without the presence of particles, which are closed to the fracture surface between NRG at the edge of easy and non-easy slip planes, where the Schmid and Taylor factor are 0.1 and 0.2 which are very small for the area acquired. Area two has the same characteristics as area 1; however, the Taylor factor has variations of 0.7. Area 3, 8 and 9 are at different depths from the fracture surface, and the voids nucleated at IMPs in triple junctions between recrystallised, and non-recrystallised grains in places where the easy slip {111} plane and non-easy slip planes are in contact, the Taylor factors changes are 0.6, 0.2, 0.4 respectively. Area 4 consist of two voids with different characteristics, first a) the superior void nucleates without particles between recrystallised grains, and b) the inferior void grows at IMPs in the middle of RG and NRG when the blue plane is closed to non-easy slip planes, both voids have the same Schmid and Taylor Factor changes. Finally, Area 7 points out a long, narrow void between recrystallised grains that is particular, as it is not present in samples tested at vacuum and also presents only 0.2 variations in the Taylor factor. All the data discussed in this section are summarized in table 6.5.

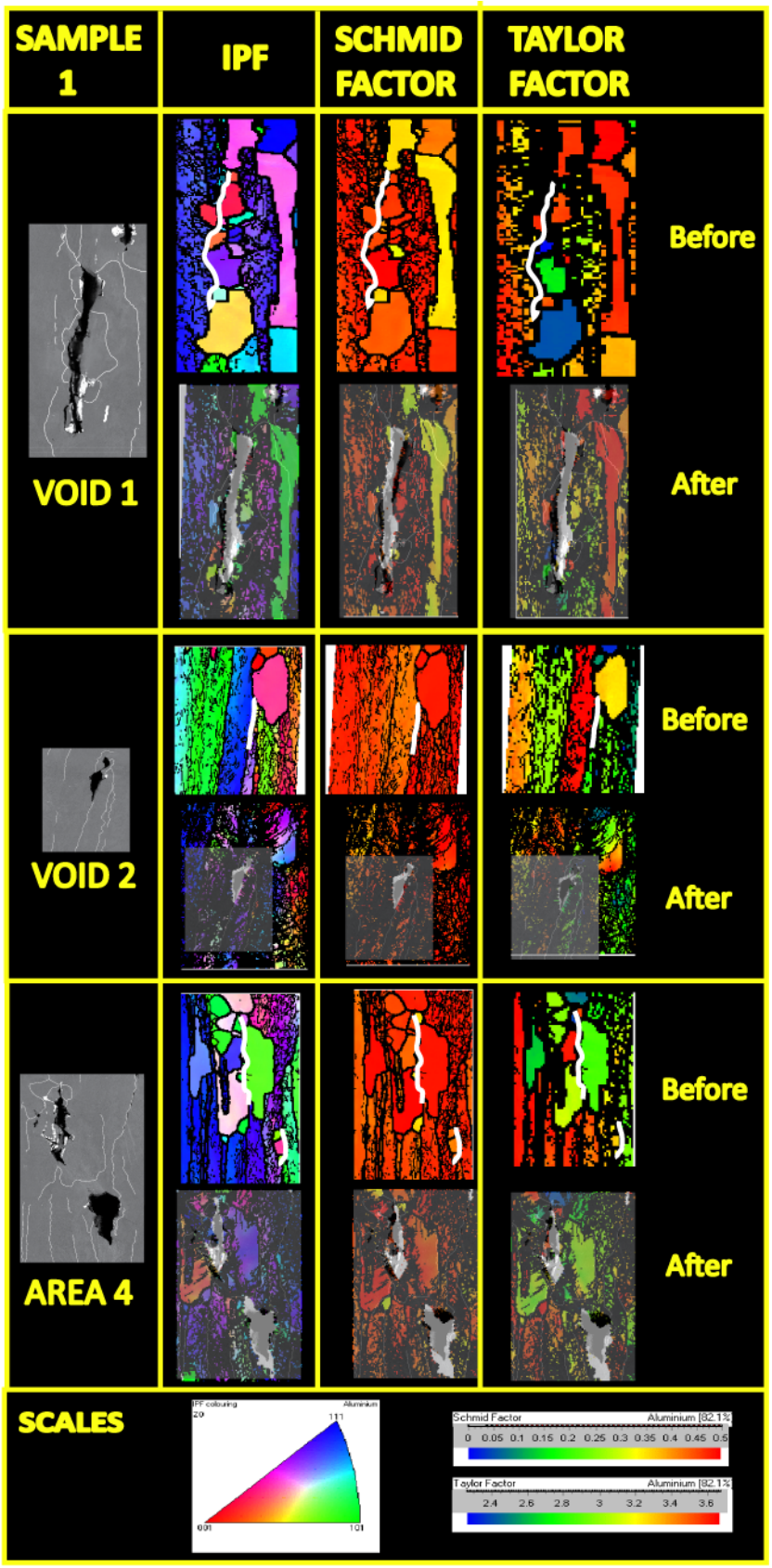

Figure 6-14. EBSD map results (IPF, Schmid and Taylor factor) for sample 1, acquired before and after interrupted SSRT tensile testing for areas of interest, on every area the original BSE-SEM image is detailed with the EBSD maps taken before fracture and the EBSD maps taken after the fracture in the lower part. The maps were processed using "Tango" Oxfords' software, voids and cracks are indicated in white lines in the EBSD before fracture maps. The scales are found at the bottom of the image – Part 1.

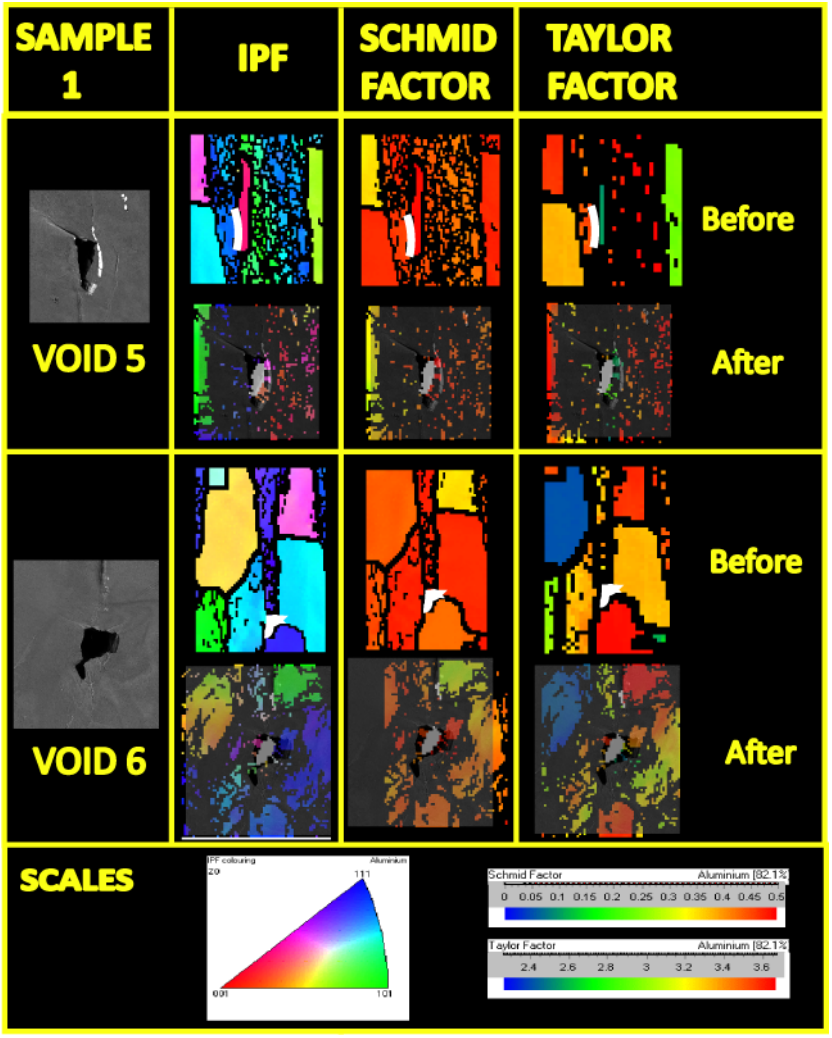

Figure 6-15. EBSD map results (IPF, Schmid and Taylor factor) for sample 1, acquired before and after interrupted SSRT tensile testing for areas of interest, on every area the original BSE-SEM image is detailed with the EBSD maps taken before fracture and the EBSD maps taken after the fracture in the lower part. The maps were processed using "Tango" Oxfords' software, voids and cracks are indicated in white lines in the EBSD before fracture maps. The scales are found at the bottom of the image – Part 2.

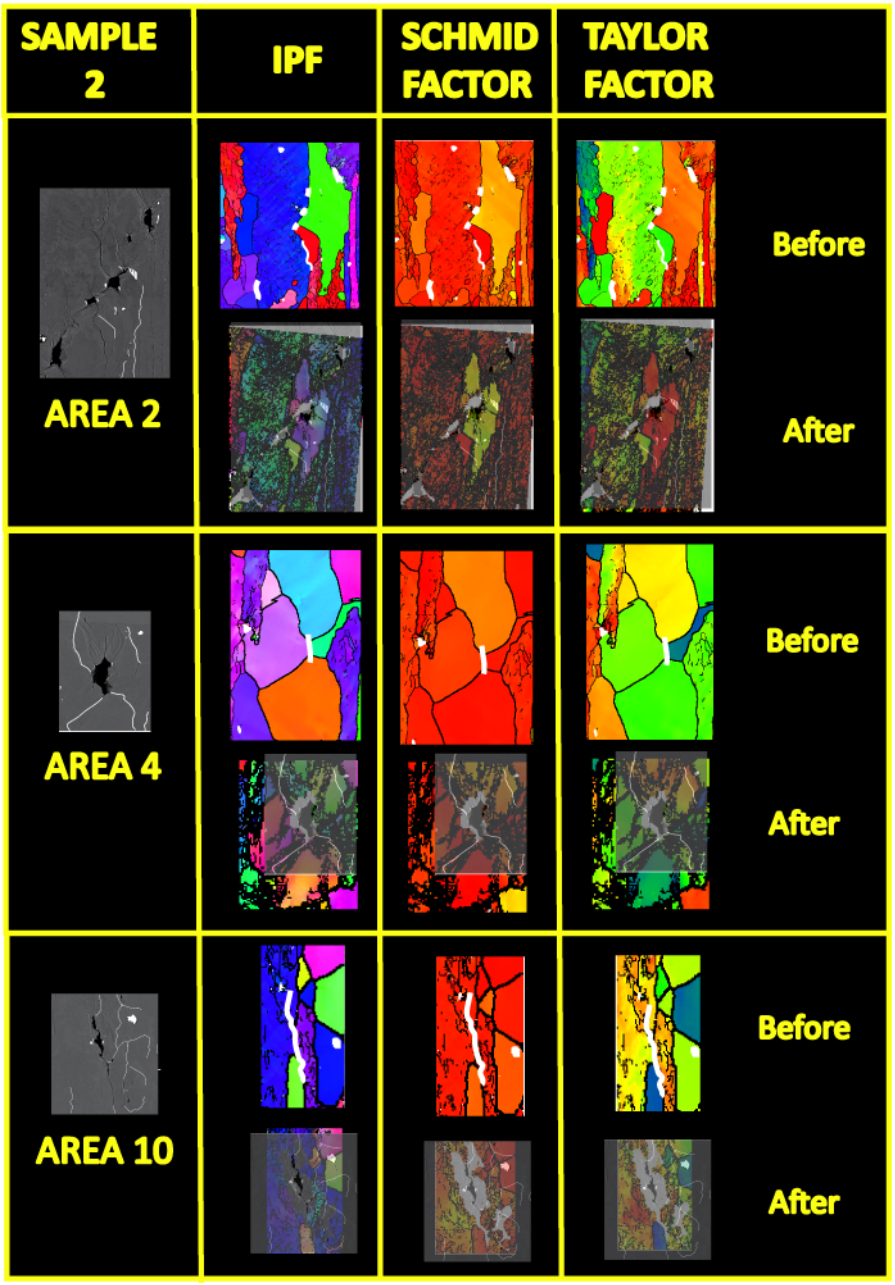

Figure 6-16. EBSD map results (IPF, Schmid and Taylor factor) for sample 2, acquired before and after interrupted SSRT tensile testing for areas of interest, on every area the original BSE-SEM image is detailed with the EBSD maps taken before fracture and the EBSD maps taken after the fracture in the lower part. The maps were processed using "Tango" Oxfords' software, voids and cracks are indicated in white lines in the EBSD before fracture maps. The scales are found at the bottom of the image – Part 1.

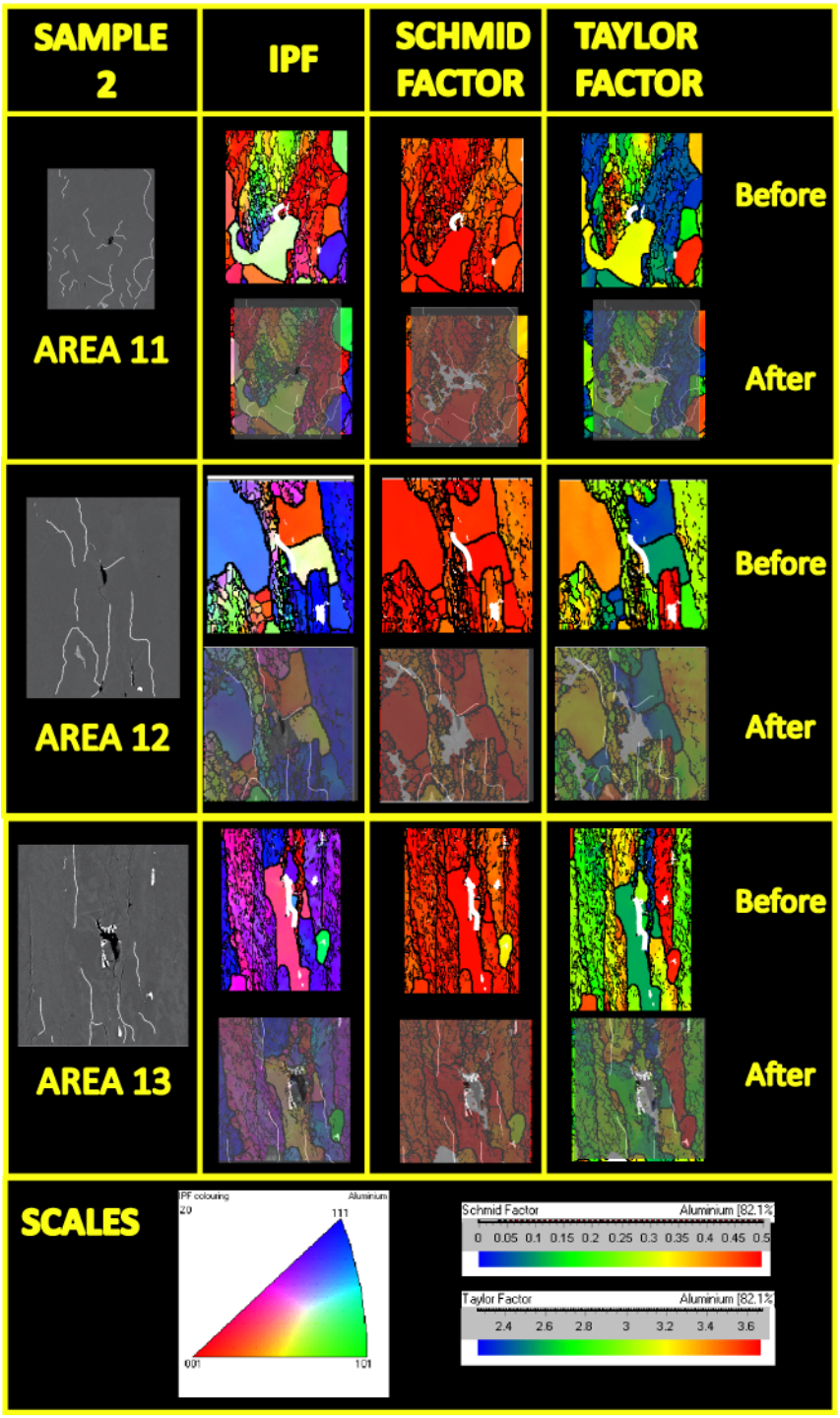

Figure 6-17. EBSD map results (IPF, Schmid and Taylor factor) for sample 2, acquired before and after interrupted SSRT tensile testing for areas of interest, on every area the original BSE-SEM image is detailed with the EBSD maps taken before fracture and the EBSD maps taken after the fracture in the lower part. The maps were processed using "Tango" Oxfords' software, voids and cracks are indicated in white lines in the EBSD before fracture maps. The scales are found at the bottom of the image – Part 2.

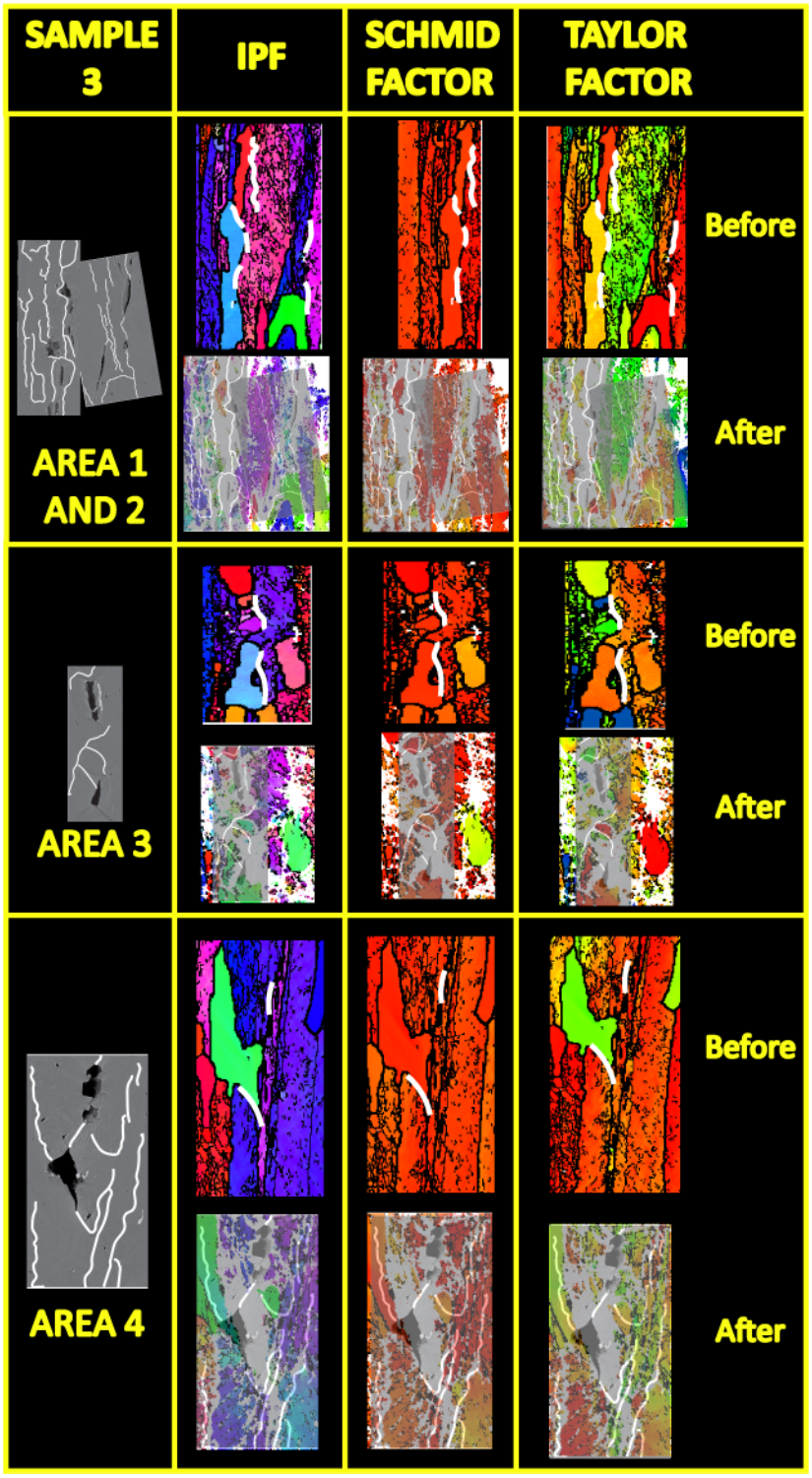

Figure 6-18. EBSD map results (IPF, Schmid and Taylor factor) for sample 3, acquired before and after interrupted SSRT tensile testing for areas of interest, on every area the original BSE-SEM image is detailed with the EBSD maps taken before fracture and the EBSD maps taken after the fracture in the lower part. The maps were processed using "Tango" Oxfords' software, voids and cracks are indicated in white lines in the EBSD before fracture maps. The scales are found at the bottom of the image – Part 1.

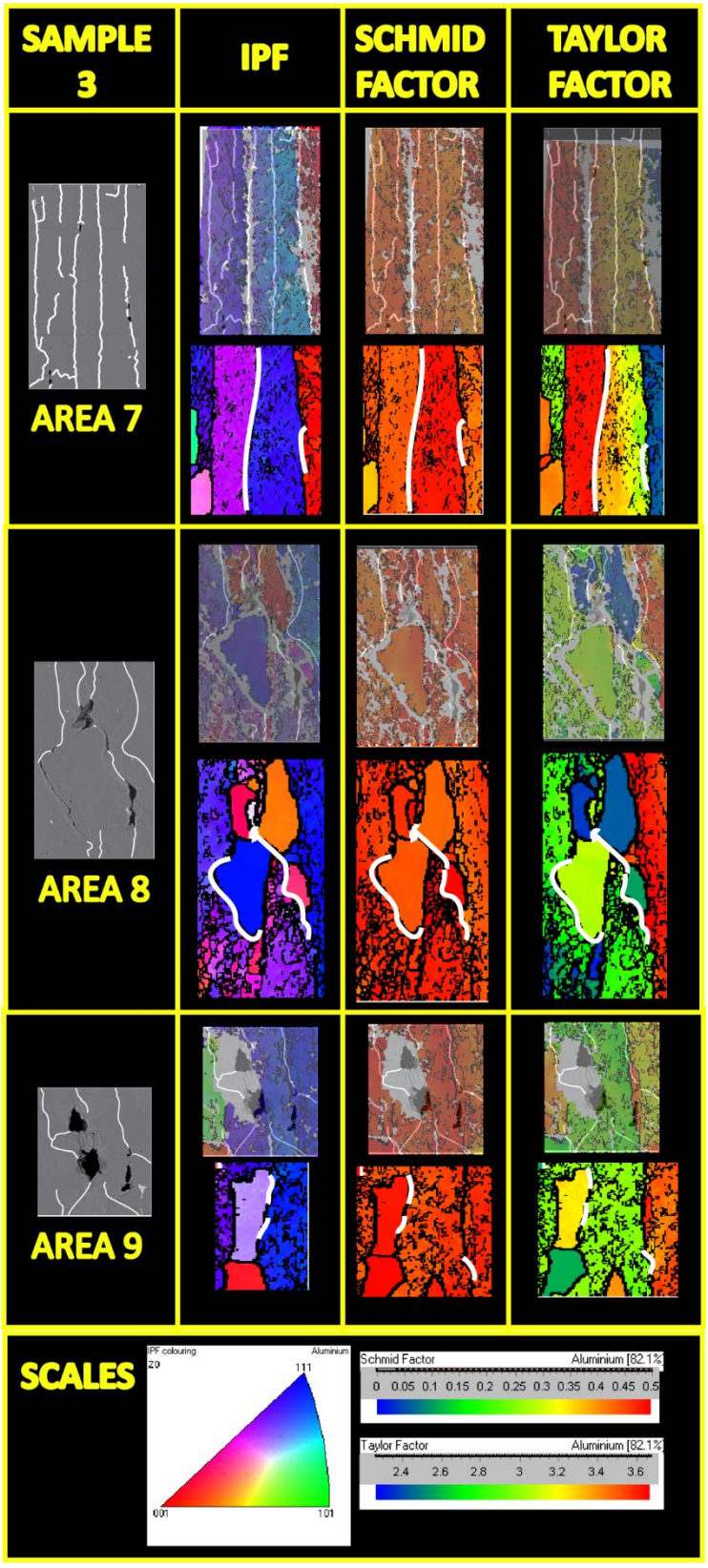

Figure 6-19. EBSD map results (IPF, Schmid and Taylor factor) for sample 3, acquired before and after interrupted SSRT tensile testing for areas of interest, on every area the original BSE-SEM image is detailed with the EBSD maps taken before fracture and the EBSD maps taken after the fracture in the lower part. The maps were processed using "Tango" Oxfords' software, voids and cracks are indicated in white lines in the EBSD before fracture maps. The scales are found at the bottom of the image – Part 2.

Table 6-5. Summary of EBSD map characteristics of voids in samples 1, 2 and 3 tensile tested at a strain rate of $10^{-5}\ /s$ at different humidity levels for the alloy AA7040-T7651, showing size, void location, Schmid and Taylor Factors.

L (um)	Distance	Sample	Void or Area	Size		P	TJ	IPF					Schmid Factor	
				W (um)	Area			RG	NRG	RG AND NRG	<111> and other	Other Planes	Easy slip system	Taylor Factor Change
15	850	2	11	11	126		x			x		x	0.1	0.8
21	485	1	6	17	214		x			x	x		0.1	0.4
21	555	1	5	9	131	x	x			x	x		0.1	1
24	1000	2	12	4	72	x	x			x	x		0.1	0.4
32	549	3	4 Inf	55	588	x	x			x	x		0.1	0.6
34	495	3	3 Inf	8	97	x	x			x		x	0.1	0.6
35	1507	3	8 Der	8	150	x	x			x		x	0.1	0.2
36	292	3	2 Cen	22	107		x			x		x	0	0.4
37	1315	3	9	25	411	x				x	x		0.1	0.4
42	495	3	3 Sup	10	205	x	x			x		x	0.1	1
43	818	3	7 Der	8	167			x			x		..1	0.4
46	700	2	4	23	676	x	x	x				x	0.1	0.8
46	1450	2	13	9	351	x	x			x		x	0.1	0.2
47	510	2	2 Sup.	15	600		x	x		x	x		0.1	0.2
49	549	3	4 Sup	16	349		x			x	x		0.1	0.6
51	496	2	2 Cen	23	547	x	x			x	x		0.2	0.6
56	428	2	2 Inf	20	624		x			x	x		0.1	0.6
61	175	3	1 Sup	13	608			x			x		0.1	0.2
61	750	2	10	11	284	x	x			x	x		0.1	0.4
73	1573	3	8 Izq	2	154					x	x		0.1	0.2
77	292	3	2 Sup	3	185		x			x		x	0.1	0.7
79	876	1	4	45	2220	x	x			x		x	0.2	0.8
80	140	3	1 Inf	5	432		x				x		0	0.8
89	557	1	2	27	1032	x	x				x		0.1	0.8
96	882	3	7 Izq	3	209			x			x		0.1	0.2
147	453	1	1	15	1692	x	x			x	x		0.2	1

RG = Recrystallized grains, **NRG =** Non-Recrystallized grains, **TJ =** Triple Junction, **W=**width, **H=** length, **P=** particle, **Sup =** superior, **Inf =** Inferior, **Cen=** Centre

In figure 6.20, three cases were selected based on the length of the voids to analyse their characteristics. For case 1, three voids with similar length nucleated at particles and triple junction, between recrystallised and non-recrystallised grains present a small Schmid factor variation; however, the Taylor factors are considerably different 1, 0.4 and 0.6. Case 2, analyzed three voids with similar lengths, the voids starts at triple junctions between recrystallised and non-recrystallised grains, again the variations in Taylor factor are 0.8, 0.4 and 0.2 respectively. Finally, case 3 analyzed only two areas in which; void 2 in sample 1 seems to be formed by the coalescence of voids and was nucleated at triple joints with a Taylor Factor of 0.8. Moreover, area 7 in sample 3 which is characterized by a "string of cracks join by voids", a feature that was not observed on other samples at lower humidity levels is formed in the middle of two non-recrystallised grains without any visible particle and with 0.2 change in the Taylor factor value.

It was observed that almost all voids occurred at triple junctions between recrystallised and non-recrystallised grains. Also, it was seen that there was a tendency for voids to occur between easy-slip planes (blue in IPF) and non-easy slip planes (other colours) for all samples. It seems like there is not a specific relationship between the distance from the fracture surface and the size (radio, length, width and area) of cracks and voids; this may mean that the microstructure characteristics mostly control the growth behaviour. However, it was unexpected that in vacuum, the majority of voids were produced at places with Taylor factors bigger than 0.6 while for samples tested at vacuum voids and cracks occurred even at Taylor factor variations of 0.2.

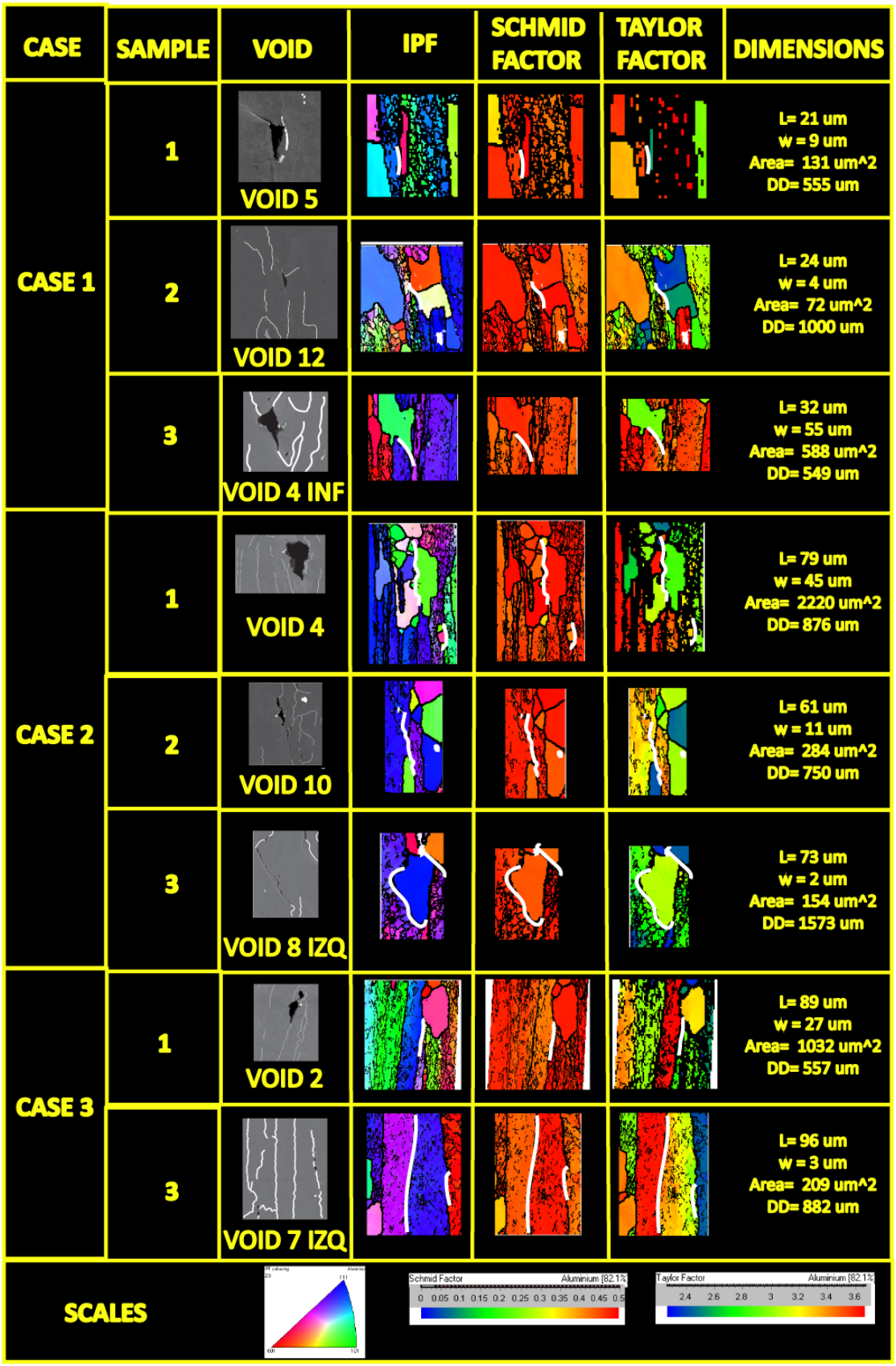

Figure 6-20. EBSD map results (IPF, Schmid and Taylor factor) acquired before interrupted SSRT tensile testing for three cases of interest, on every section the original BSE-SEM image after fracture is detailed with the EBSD maps taken before fracture. The maps were processed using "Tango" Oxfords' software, voids and cracks are indicated in white lines in the EBSD before fracture maps, with the respective dimensions on the right. The scales are found at the bottom of the image.

6.3. Discussion

The in-situ test for samples tested at dry air allowed the understanding of the material deformation until fracture without the effects of hydrogen, and it was observed that: no significant damage occurs before yielding, voids nucleates mainly at particles, voids that form earlier have more growth, cracks are formed only between neighbouring voids, and it seems that voids located in big clusters of particles do not grow as much as small particles. Moreover, most of the damage occurred after UTS closed to fracture; at this stage; some voids can grow rapidly by tearing and void coalescence. Finally, as almost all voids occurred at particles the void in zone 4(sample 4) is very curious, as it grows in the middle of two grains one reason might be that the void started at a particle under the surface or grains are not favorably oriented causing the imminent failure.

For the ex-situ tests, It is evident that first, the depth of damage increases as the humidity content increases and the strain rate decreases. For all samples the size and number of the voids seem to be independent of the distance to the fracture surface; all samples displays 2.5 times more cracks than voids; however, it is observed that the number of voids increased up to 40% when the humidity levels changes from 0 to 90%RH, also, the number of cracks increased slightly (6%) when the strain rate decreases and the humidity content increments. It is surprising to see that sample 3 has a bigger number of cracks and voids, but it contains a high number of small voids and cracks which gives a false idea of the average size and aspect ratio of these features. Sample 3 displays a feature called “string of cracks joined by voids”, which was formed by little voids at grain boundaries with cracks between then; this might indicate that humidity plays a very detrimental role. For instance, the “string of cracks joined by voids” can be seen in cases like area 7 (sample 3) were is observed that the feature is long and can affect the microstructure stability; moreover, these samples have larger voids, in a mayor quantity than sample 1, which is not easily seen when analysing the general data of the sample. It is interesting to notice that the quantity of humidity in the air plays an essential role when compared with exposition times, sample 5 is more affected by humidity than sample 2 however is not as affected as sample 3, even when the time of exposure was two times longer for samples 4 and 5.

For the testing conditions in the present study, the number of medium-cracks (separations between grains) at grain boundaries seems to be independent of the strain rate variations, and it is observed that when humidity increases the separation can be increased up to 95% from 0 to 90% RH, this might indicate that these increments depend on the humidity only.

Finally, in samples tested at vacuum voids occurred in most voids when the Taylor factor variation between grains is more than 0.6. However, when humidity is applied, something unexpected occurred a significant number of voids occurred even when for Taylor factor variations of 0.2, such behaviour is contradictory as voids occurred in places with big Taylor factor variations because grains have significant deformation incompatibility. Nevertheless, when comparing voids with the same characteristics (particles, length, triple junctions and orientations), these failures are difficult to explain and might be attributed to the humidity effects in the material as all the other possible variables are similar.

Chapter 7. Effects of Hydrogen Embrittlement in AA7040-T7651 in fractography.

7.1. Introduction

The present chapter aims to correlate the findings of chapters 5 and 7 to understand the total failure behaviour of the samples when exposed to different humidity levels and strain rates. For this, the fractography analysis will be taken into account looking for fracture surface differences and microstructure features(grain boundaries, particles). To conclude, an interpretation of the data presented is discussed.

7.2. Results and discussion.

All the tests presented in this chapter were performed in aluminium alloy 7040-T7651 samples in the as-received condition; surface preparation was done as explained in section 4.2.2, then interrupted slow strain rate testing was done as discussed in section 4.2.5., fracture surface imaging parameters are described in section 4.2.6

7.2.1. Fractography Analysis

The effects of Hydrogen embrittlement in aluminium 7xxx series have been widely studied through fracture surface analysis, in which HE is characterised by intergranular brittle features (shallow dimples, smooth and shiny surfaces). Figure 7-1 displays three fracture surface types present in some aluminium alloys when exposed to moist environments: In a) ductile features (fracture “type 3”) characterised by dimples are observed surrounded in green areas. The red arrows point areas with precipitates and brittle, high topographical features that in the present work will be known as fracture “type 2” considered a brittle fracture. In b) blue arrows point brittle smooth areas with bright surfaces and visible grain boundaries (fracture “type 1”), also fracture “type 2” (red arrows) is observed occurring at precipitate clusters, likewise tear ridges and appreciable height changes between grains are appreciated. Finally, the white arrows reveal cracks between grains. For the effects of future computations in the present research, fractures “type 1” and “type 2” will be referred as brittle areas and fracture “type 3” as ductile areas.

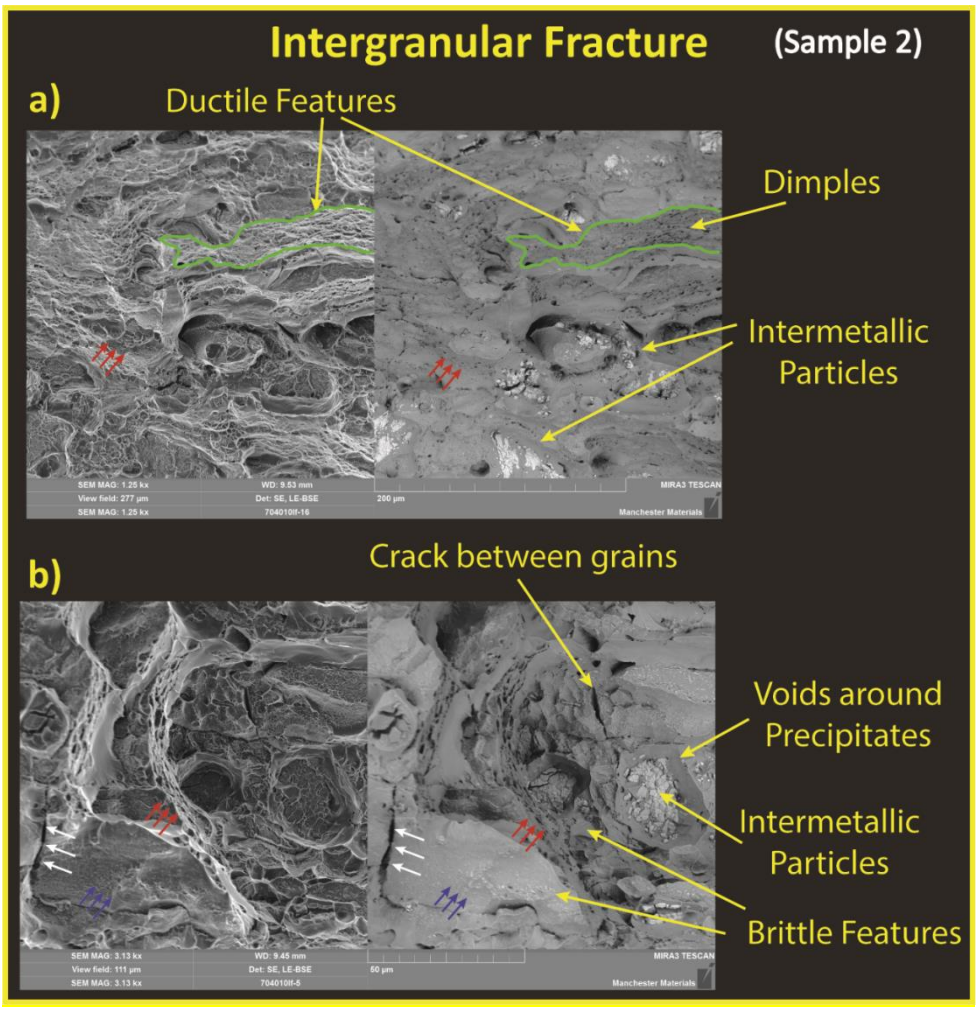

Figure 7-1. Fracture surface characteristics of AA7040-T7651 sample 2, after tensile testing in moist air in a) the green lines are surrounding the fracture "type 3" (ductile area) and b) (brittle areas) red arrows pointing fracture "type 2" and blue arrows showing fracture "type 1", cracks between grains are pointed in white arrows.

When materials suffer Hydrogen Embrittlement, there is a reduction in the cross-sectional area and the ductile area fraction; then, these parameters are essential to compare the susceptibility degree of the alloy AA7040-T7651 in moist environments. The area reduction was obtained for all the samples; first, the initial width and length of the specimens can be found in table 7-1. Next, ImageJ was used to i) set a scale and ii) delimit and measure the minimum area at the fracture surface (final area), as can be seen in figure 7-2, for sample 1. Finally, the area reduction (RA) was obtained using the equation Eq. 7-1, obtaining a value of 24.9%.

Table 7-1. Initial dimensions before testing for AA7040-T7651 samples.

Sample	Width (mm)	Length (mm)	Initial Area (mm^2)
1	2.95	0.99	2.92
2	2.9	1.12	3.25
3	2.87	1.15	3.3
4	2.87	1.02	2.93
5	2.94	1.05	3.09

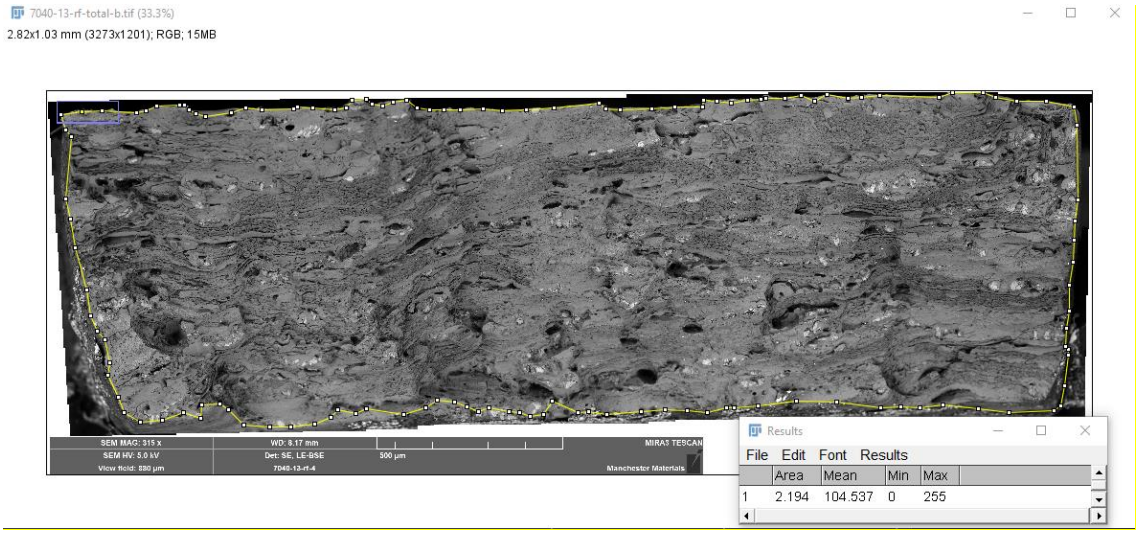

Figure 7-2. Illustration of cross-sectional area measurement for sample 1 after tensile testing using the software ImageJ.

$$RA = \frac{Initial\ Area - Final\ Area}{Initial\ Area} * 100\% \qquad \text{[Eq. 7-1]}$$

$$RA = \frac{Initial\ Area - Final\ Area}{Initial\ Area} * 100\%$$

$$RA = \frac{2.92 - 2.194}{2.92} * 100\% = 24.9\%$$

Next, to compute the fraction of brittle surfaces, “ImageJ” software was used to classify and determine the ductile and brittle areas. Figure 7-3 displays an example of the areas computation process. In which, a) three types of areas were assigned using the plugin

"Trainable Weka Segmentation": i) ductile areas (green) are characterised by dimpled surfaces, ii) brittle areas (red) are composed by fractures "type 1" and "type 2" and iii) voids (purple) are deep features on the surface that cannot be easily determined as brittle or ductile areas. Error is the calculation such as edges (on b) outside the sample can be classified as brittle or ductile areas, (on c) boundaries between ductile and fragile areas are not well computed and (on d) the presence of some impurities in the surface can be determined as ductile areas. The errors found represent a minimal area of the total surface and represent a maximum 6% error in the total computations. Then, (on e) a threshold is applied on the segmented image, some noise is removed for all areas and (on f) the final area computation is acquired. Is important to notice that voids are excluded from the calculation, and the formulas Eq. 7-2 and Eq. 7-3 were used to determine the ductile/fragile fractions.

$$Total\ Area = Ductile\ Area + Fragile\ Area \qquad \text{[Eq. 7-2]}$$

$$Ductile\ Area = \frac{Ductile\ Area}{Total\ Area} * 100\% \qquad \text{[Eq. 7-3]}$$

In table 7-2, it is observed that as the humidity levels increases, the ductile fraction decreases between samples tested at the same strain rate. When comparing samples with the same humidity levels and different strain rate; for instance, sample 2 (area reduction, 23.8%$\pm$ 2.8) and sample 5 (area reduction, 25.2%$\pm$ 2.8), it can be noticed that the reduction in area is similar for both samples tested at different strain rates, and the brittle fraction varies slightly between samples, this correlates with the information presented in figure 6-13, for samples tested at different strain rates, it was noticed that the same environment did not display significant changes, this also supports the theory that the material embrittlement is caused mainly by hydrogen effects, Sample 1 (brittle fraction, 34.2 $\pm$ 6%) and sample 4 (brittle fraction, 42.4 $\pm$ 6%)) followed the same behaviour indicate a slight increased in the brittle fraction when the strain rate decreases.

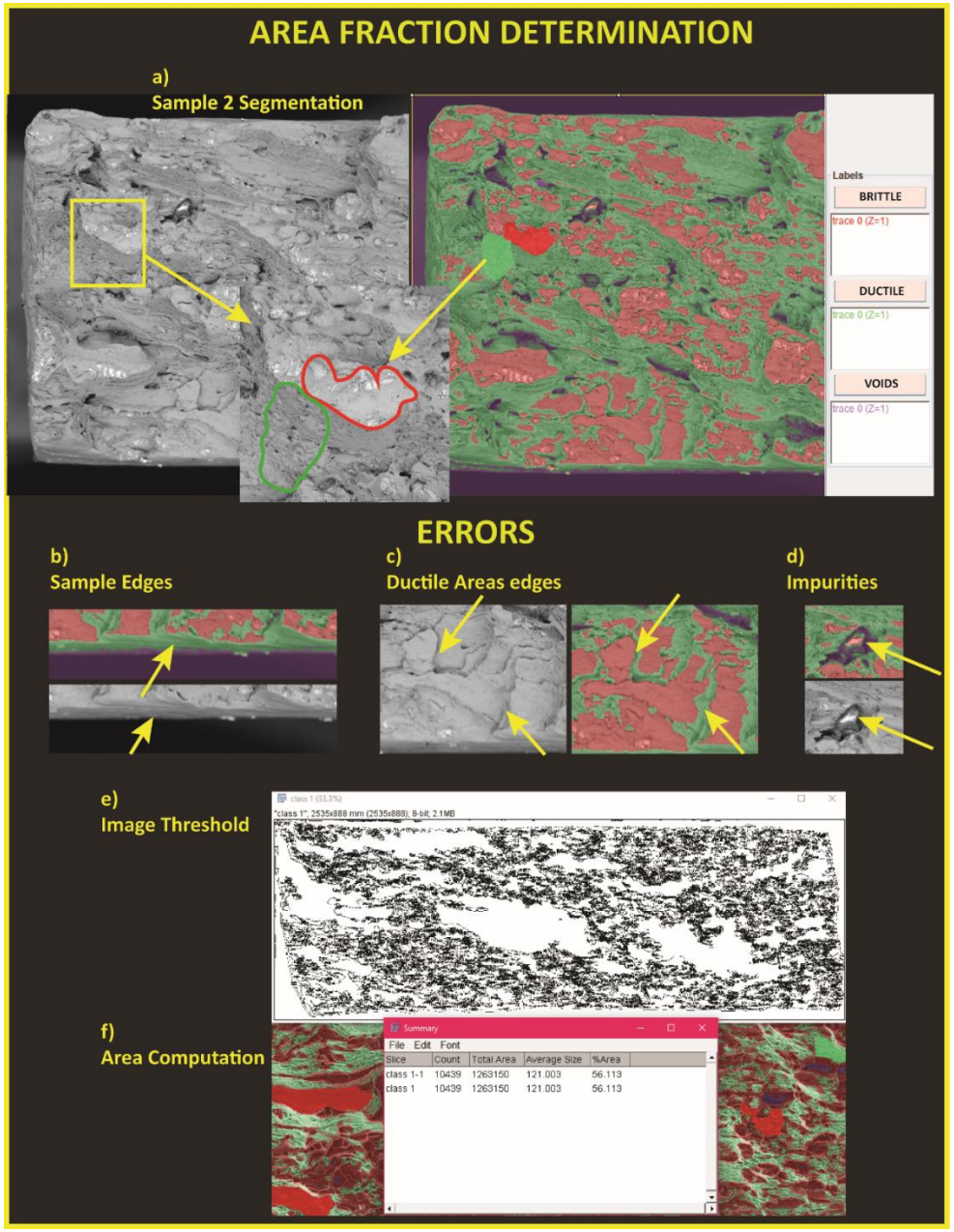

Figure 7-3. Ductile/Fragile fraction determination using ImageJ software to a) classify ductile (green) and fragile areas (red), segmentation errors at b) sample edges, c) ductile-fragile intersections and d) impurities present on the surface, to finally e) apply an image threshold and f) determine the areas.

Table 7-2. Area reduction and brittle/ductile fractions on fracture surfaces for AA7040-T7651 samples tested under different conditions.

	Sample 1	Sample 2	Sample 3	Sample 4	Sample 5
Initial Area (mm^2)	2.92	3.25	3.30	2.93	3.09
Final Area (mm^2)	2.19	2.48	2.59	2.07	2.31
Area Reduction (%)	24.9± 2.8	23.8± 2.8	21.6± 2.8	29.3± 2.8	25.2± 2.8
Brittle Fraction (%)	34.2 ± 6	62 ± 6	78.6 ± 6	42.4 ± 6	64 ± 6
Ductile Fraction (%)	65.8 ± 6	38 ± 6	21.4 ± 6	57.6 ± 6	36 ± 6

Figure 7-4 shows the fracture surface of sample 1 tested at vacuum (dry air), in which a) the SE image displays an intergranular fracture, grain topography, large isolated voids and dimples along the whole surface, on b) the edges were analyzed looking for any superficial defects, no possible initiation sites were found, it is believed that voids initiated inside the sample in voids and propagate inside-out leaving a dimpled surface. On c) some places of interest are shown in detail; zone 1 shows large voids in particles surrounded by dimples, some tear ridges are observed attributed to the propagation of fracture; zone 2 points out a grain that seems to have a flat and smooth tomography on zone 3 it is observed that these voids surfaces are formed by the presence of precipitates at the grain boundaries. Finally, in d) a lateral view of the fracture indicates the sample cross-sectional area is reduced and also that the fracture is almost flat.

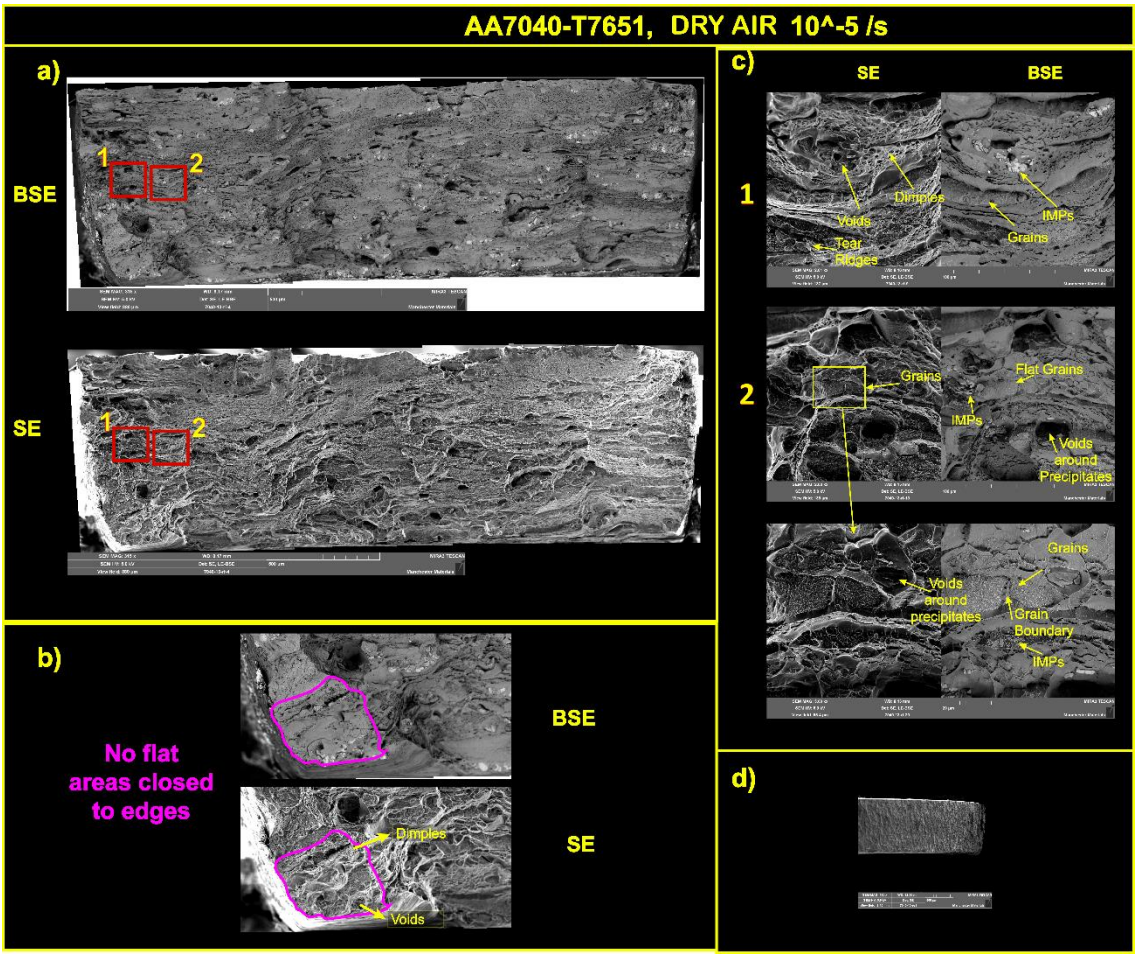

Figure 7-4. Sample 1 fracture surface SEM images AA7040-T7651 alloy showing a) dimpled surface and large voids along the fracture, b) no initiation sites closed to edges, c) areas of interest displaying fracture features characteristics and d) lateral fracture view.

Figure 7-5 presents the fracture surface of sample 4 also tested at vacuum (dry air), in which a) the SE image displays an intergranular fracture, with grain topography, large isolated voids and dimples along the whole surface, contrary to sample 1 this surface displays more deformation and different topographies along the whole surface. On b) the edges were analyzed looking for any superficial defects, no possible initiation sites were found, but the surface is clearly intergranular with the presents of IMPs clusters. On c) two places of interest are shown in detail; zone 1 closed to the edges shows high topography between grains, grains seem to have flat surfaces with particle clusters on top, moreover, the surface points voids and dimples, and zone 2 focus on a single void, it is clear that the voids nucleated before the fracture and is surrounded by a featureless area, then dimples are formed around all voids, some flat grains are observed. Finally, in d) a lateral view of the fracture indicates an area reduction; however, it is clear that there is more deformation at the fracture surface when compared to sample 1, this might be explained because sample 4 had more time to deform before fracture.

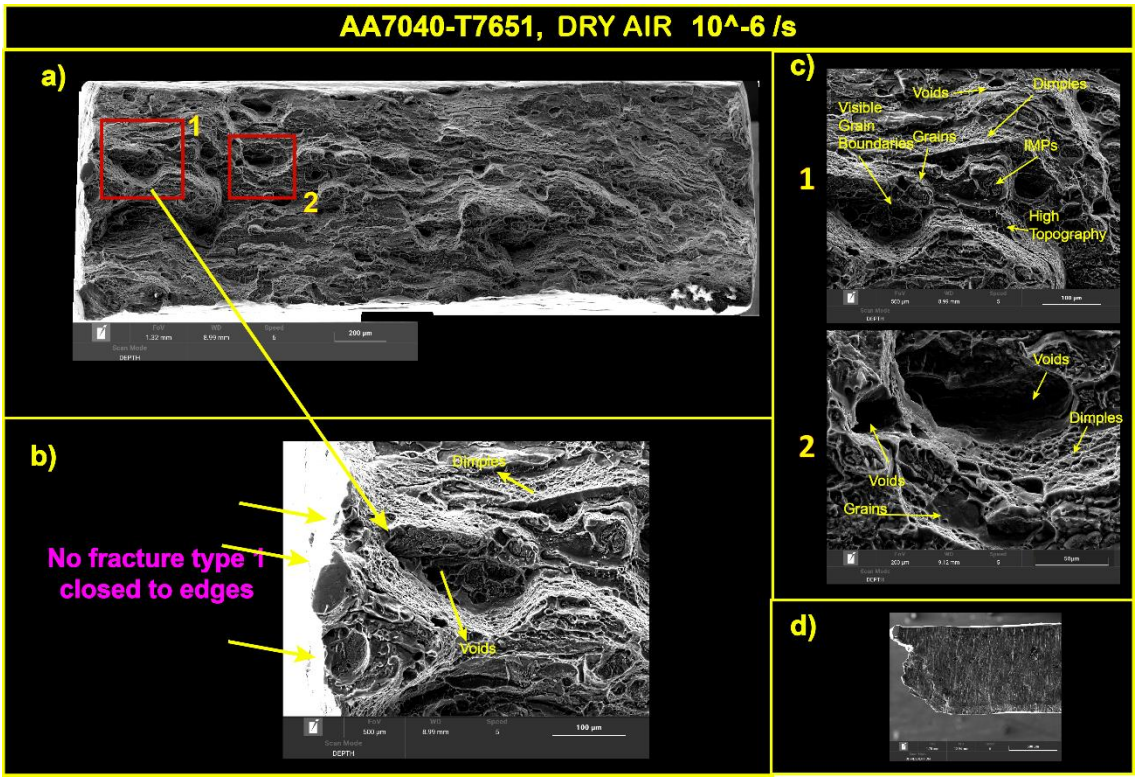

Figure 7-5. Sample 4 fracture surface SEM images of AA7040-T7651 alloy showing a) big dimples along the fracture surface and large voids, b) no initiation sites closed to edges, c) areas of interest displaying fracture features characteristics and d) lateral fracture view.

Figure 7-6 presents the fracture surface of sample 2 tested at 50%RH and a strain rate of 10^{-5} /s, in which a) the SE image displays an intergranular fracture, which contrary to samples 1 and 4 present a less dimpled surface, It must be noticed that flat, smooth areas at the edges of the specimen have been highlighted by purple lines and will be studied further as this features were not observed in samples 1 and 4. On b) the flat surfaces "Fracture Type 1" display a smooth, bright surface in which grain boundaries are easily observed, Surprisingly these surfaces are only found on edges of the samples in which possible initiation sites were found. The initiation sites are surrounded in yellow for both SE and BSE images, and they were later correlated with the polished fracture surface, in which, it was observed that separations of grain boundaries on the surface were the responsible for this featureless fracture (zone i and iv); in other initiation sites, precipitates are noticed (zone iii), and it was also found that this might be caused by voids nucleated at precipitates which are located at grain boundaries separations. Afterwards, the fracture propagates into neighbouring grains (zone ii) seems like tearing of the material between the grains without the presence of any microvoids. At some point the fracture mode changes into a "fracture type 2" characterised by a high topographical brittle surface with the presence of precipitates on top of grains, Finally "fracture type 3" would indicate the places in which the material grains tear up at fracture.

On c) three places of interest are shown in detail, zone 1 displays a "fracture type 2" with high topography between grains, grain boundaries are easily identified, and also the presence of significant clusters of particles are observed. Zones 2 and 3, also show voids closed to "fracture type 2" surfaces, characterised by the presence of particle cluster, high topography and dimples. Finally, in d) the lateral fracture view shows that the fracture occurred at a 45-degree angle, which is contradictory with the observations for samples tested at vacuum, however, this might happen as fracture start in the initiation sites and then start tearing up into the material with little time for deformation, which is in accordance with the literature. (Cottrell, 1958) [91]

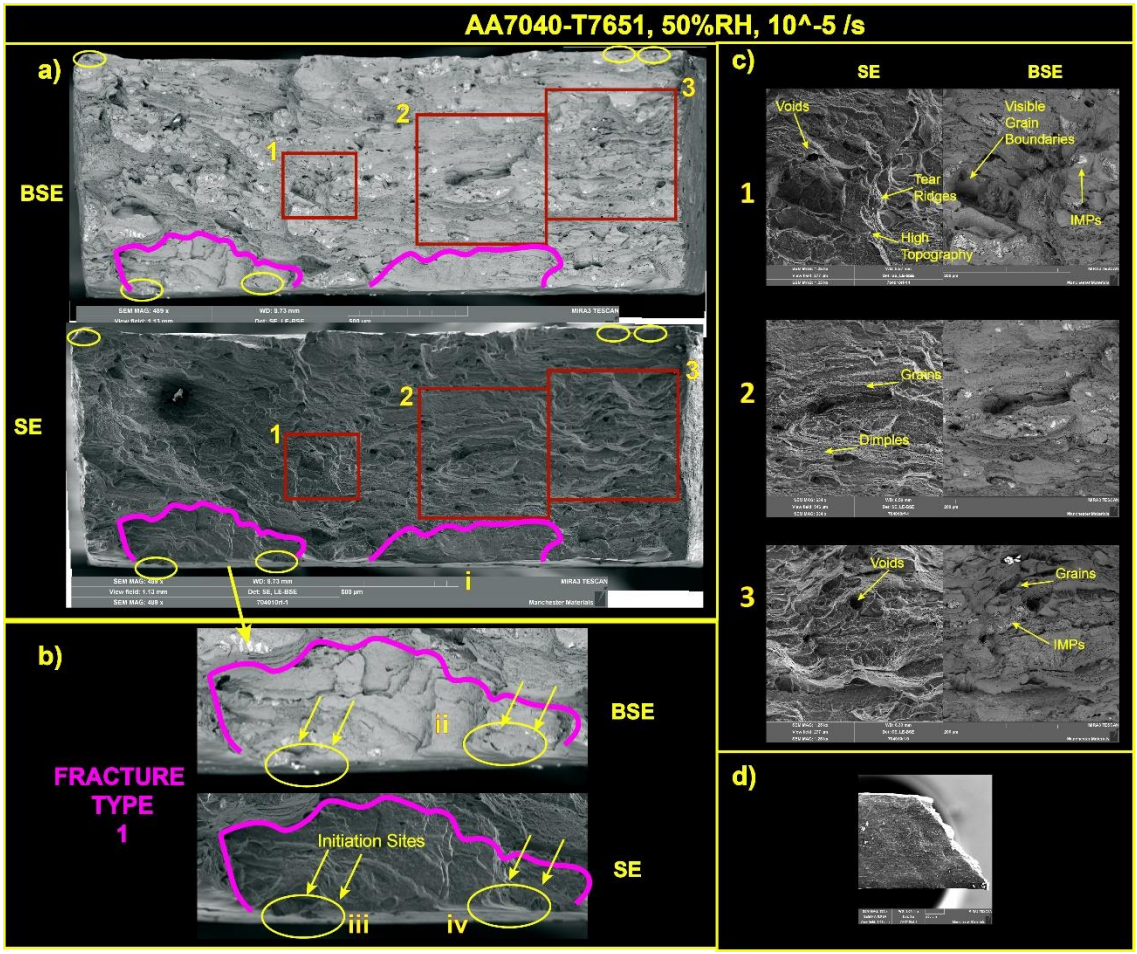

Figure 7-6. Sample 2 fracture surface SEM images AA7040-T7651 alloy showing a) an overview of the fracture surface displaying intergranular fracture, b) Fracture Area "Type 1" pointing possible initiation sites, c) areas of interest displaying fracture features characteristics and d) lateral fracture view.

Figures 7-7 of the fracture surface for sample 3 tested at 90%RH and a strain rate of 10^{-5} /s, in which a) the SE image displays that flat, smooth areas at the edges of the specimen highlighted by purple lines. On b) the flat surfaces "Fracture Type 1" with smooth, bright surfaces in which the grain boundaries easily identified display in yellow circles what it seems like possible initiation sites; it is vital to notice that sample 3 has more "fracture type 1 area" than sample 2. The "fracture type 1" was correlated with the polished surface, and it was determined that it was generated at grain boundaries separations, the fracture also develops along voids nucleated at particles that were located at grain boundaries separations; then, as observed for sample 2 the fracture propagates by tearing into the neighbouring grains without the apparent presence of microvoids, and at some point, the fracture changes into the "fracture type 2".

On c) fractures “type 2 and 3” are identified, and finally, in d) the lateral fracture view shows again that the fracture surface developed in a 45-degree angle as expected. The same fracture types were observed for sample 5 tested at 50%RH at a strain rate of $10^{-6}\ /s$, the fracture “Type 1” for samples 2 and 5 are in minor quantities than the observed for sample 3, sample 5 also displays fractures “Type 2 and 3” with a lateral fracture view in a 45-degree angle, the results for sample 5 can be found on figure 7-8.

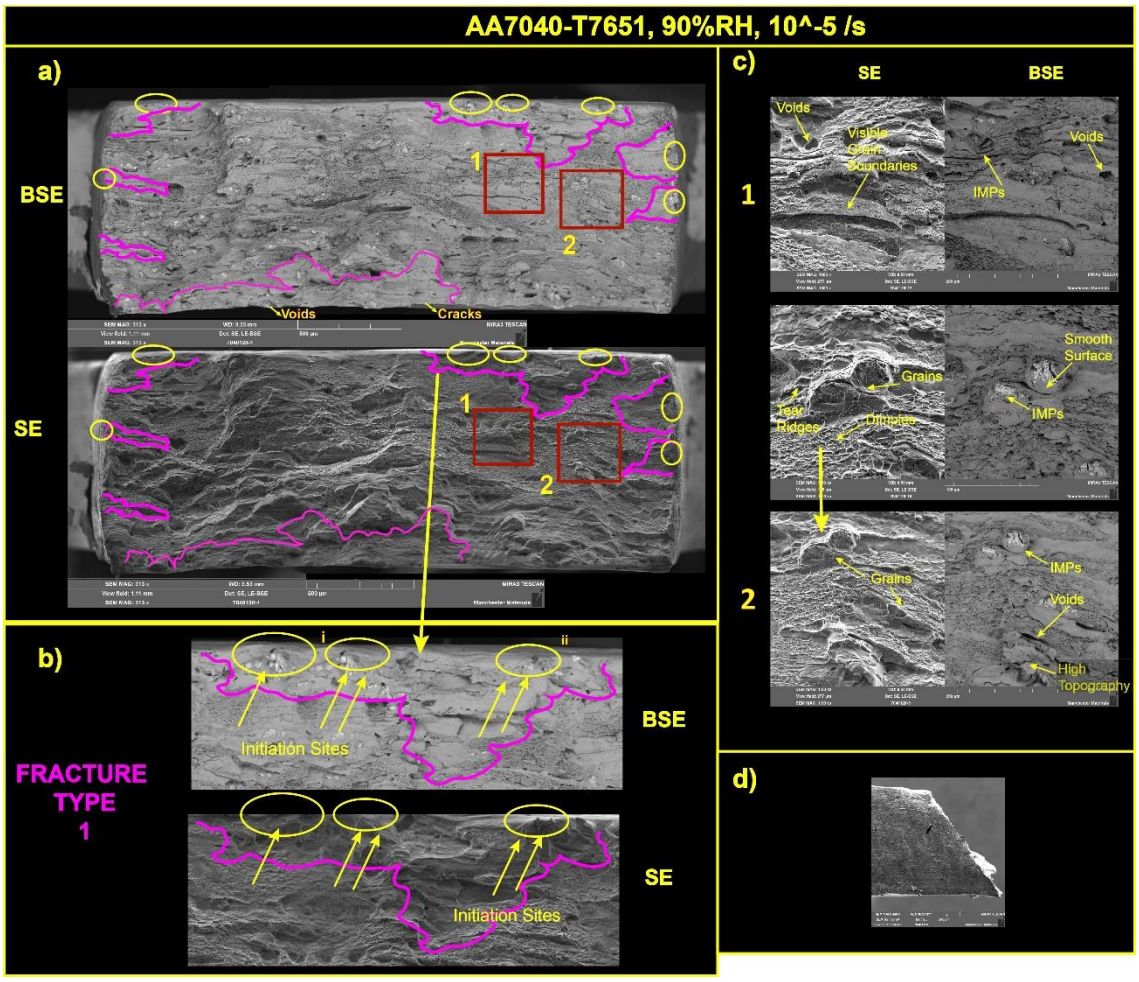

Figure 7-7. Sample 3 fracture surface SEM images AA7040-T7651 alloy showing a) an overview of the fracture surface displaying intergranular fracture and fracture “Type 1” areas surrounded in purple, b) Fracture Area “Type 1” pointing possible initiation sites, c) areas of interest displaying fracture features characteristics and d) lateral fracture view.

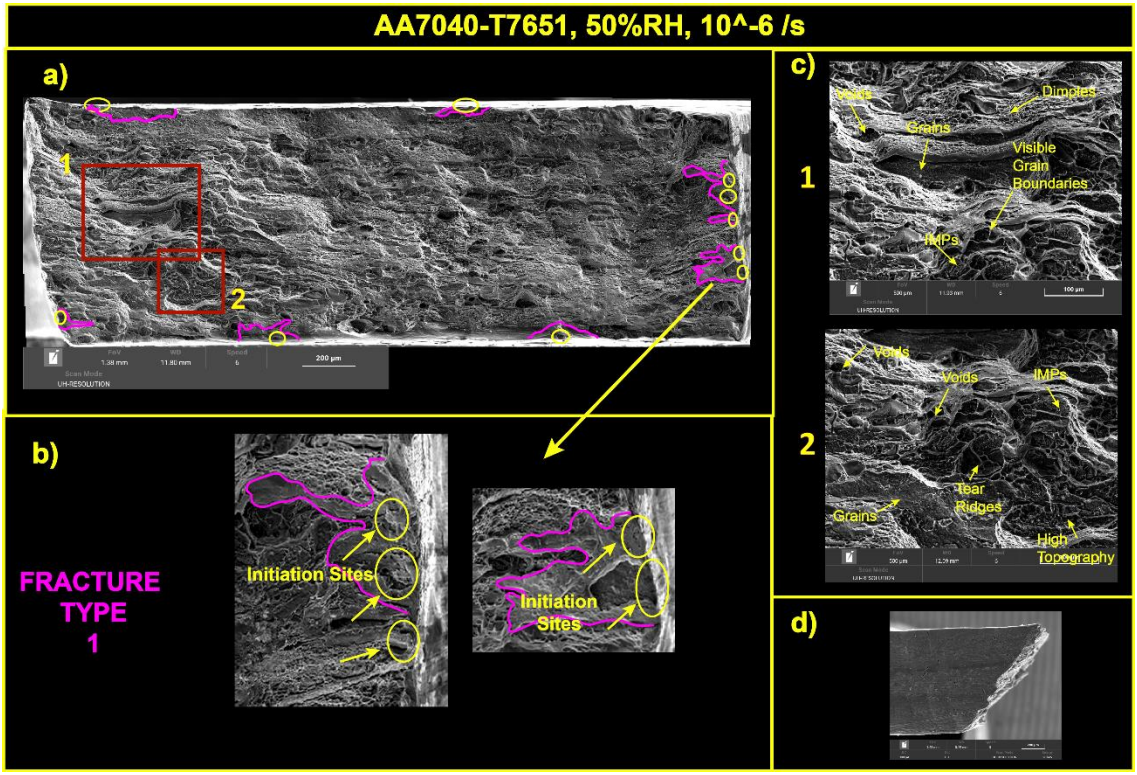

Figure 7-8. Sample 5 fracture surface SEM images AA7040-T7651 alloy showing a) an overview of the fracture surface displaying intergranular fracture and fracture "type 1" areas surrounded in purple, b) Fracture Area "Type 1" pointing possible initiation sites, c) areas of interest displaying fracture surface "Type 2" and d) lateral fracture view.

7.3. Discussion

The effects of hydrogen embrittlement are identified and quantified for all samples tested at different parameters; it was observed that samples tested at dry air display large voids and dimpled surfaces. On the other hand, samples 2, 3 and 4 show the possible initiation sites on the edges of the material, in which a smooth, almost featureless fracture surface known as "fracture Type 1", which at some point develops into a brittle "fracture type 2" which is characterised by the presence of IMPs and high topography showing flat grains and finally change into a "fracture Type 3" composed of dimples. It should be noticed that the sample 3 seems to have a more significant fraction of "fracture type 1" surface when compared with samples 2 and 4. Finally, it is identified that as humidity level increases there is a decrease in the area reduction which might indicate that the material is becoming brittle, this information correlates with the increase in brittle fraction as humidity increases.

Chapter 8. General Discussion, Conclusions and Future Work.

8.1. General Discussion

It is well known that high strength aluminium alloys are susceptible to hydrogen embrittlement in moist air. Many mechanisms have been proposed to explain how atomic hydrogen induces premature failure of materials, generating macroscopic intergranular flat-facets in the fracture surface. However, as existing research has been done mostly based on fracture surface studies, and there is scarce evidence of the atomic hydrogen effects in the failure process development; the hydrogen embrittlement mechanisms are still under debate.

This research aims to investigate the relationship between atomic hydrogen and the microstructure variations when aluminium alloys 7xxx series are loaded in moist and dry air to determine the hydrogen embrittlement mechanisms responsible for early failures. The present study analysed a set of interrupted slow strain rate tensile tests (SSRT) in different environments (0%RH, 50%RH and 90%RH) and two strain rate speeds (10^{-5} and 10^{-6} /s) for the aluminium alloy AA7040-T7651 with high Zn content.

The 7040-T7651 alloy samples were grinded without the used of water, and the polished OPS step reduced the contact with water to 10 minutes. Then, cleaning between steps were performed with ethanol ultrasonic baths, the specimens were immediately dry out, and then kept on a dessicator at all times before the tests. Samples were tested at a sufficient slow strain rate to avoid the initiation of Intergranular Type-1 EIC, which means that hydrogen embrittlement effects involve other types of fracture mechanisms different than the tipically associated with stress corrosion cracking (SCC), it is possible that the mechanism involves plastic deformation and it could be similar to creep processes.

Based on the comparison between strain rate and humidity concentrations, we have seen that there are significant differences in microstructural features (voids and cracks) characteristics. The number of voids observed in humid air was up to 43% more than the observed in dry air. Surprisingly this was not reflected in a change in the total elongation display in the stress-strain curves when humidity increases from 0 to 90%.

This result can be explained because the experimental tests conditions were severe and did not allow a large reduction in plastic strain. For instance, Gupta et al. (2016) [92] compared the effects of hydrogen in the alloy 7075 at a strain rate of 10^{-6} /s reporting a 69% reduction in elongation. Gupta results are equivalent with the findings obtained in the present research if the samples would have been tested in an equivalent under-aged environment.

In-situ tests were performed in samples tested in dry air under vacuum conditions. It was observed that void formation was appreciable when the specimens reach the maximum load of 466 and 495 MPa for the strain rates 10^{-5} and 10^{-6} /s respectively. Most of the voids generated in the surface are nucleated at second phase particles and few voids nucleated in areas without the presence of visible particles. Crack nucleation was observed at grain boundaries joining pre-existing voids; however, no medium cracks (separation between grain boundaries) were generated. Most of the damage (void growth) occurs rapidly after UTS, closed to the fracture point. The fracture process is the product of the rapid coalescence of voids and tearing of grains. Finally, the fracture surface is characterised by a dimpled intergranular fracture. When the fracture surface is analysed, a characteristic intergranular fracture is recognised, in which three features are observed. First, areas formed by little dimples with radios ranging from 1.8 to 7 um, which maybe be produced by hydrogen micropores are observed. Big voids characterised by the presence of constituent particles surrounded by flat surfaces caused by the matrix/particle separation; and relatively flat surfaces surrounded by tear ridges caused by the final tearing of the material.

These findings are supported by Toda et al. (2014) [93] who found that aluminium alloys casting processes produced and excessive intake of hydrogen, which is partitioned as molecular hydrogen gas and then concentrated at micropores. The tests were realised in high hydrogen and low hydrogen AA2024 aluminium alloy. The development of the fracture surface during interrupted tensile tests was studied by tomographic imaging. It was observed that: i) damage occurs at particle fractures or micropore growth; ii) Localised deformation begins when the maximum load is reached (240 MPa), iii) most of the damage is accumulated before the just before the final fracture and iv)

micropores growth in the loading direction. It is noteworthy to consider that only a few micropores coalesced and are responsible for the final fracture surface. Furthermore, in the fracture surface, micropores are observed as dimples surrounded by flat surfaces related to final tearing (Toda et al., 2009) [94], which is consistent with the findings of the present research.

Toda et al. (2014) [93] observed that when hydrogen increases in the AA2024 alloy, there is a 9% increased in the elongation during tensile tests. This last tendency is contradictory with the reported atomic hydrogen effects in the mechanical response of aluminium alloys. Base on the finding in the present research, it is strongly believed that the hydrogen present in aluminium alloys micropores contributes to the formation of the ductile fracture. This can be evident when the fracture surfaces of samples tested in dry air present dimples up to 7 um while samples tested in humid air present a reduction in the dimpled surface and a maximum size of 6 um. Then, we believed that in samples tested in dry air, molecular hydrogen has time to growth and coalescence forming the characterised dimpled surface for ductile fractures; however, when the samples are tested in humid air, atomic and molecular hydrogen may compete during the development of the fracture. Moreover, atomic hydrogen may be faster, allowing the scape of molecular hydrogen from the samples as some cracks and voids open up before molecular hydrogen can produce dimpled growth.

Only one tensile test was performed for each condition, it is still not clear if the results obtained were caused by the relaxation periods and the time holds during the tests. Then, testing using continuous strain without any holds will allow the comparison of the mechanical properties tests with the interrupted SSRT tests, and to determine if the holds had a major effect on crack initiation and growth behaviour. Furthermore, tests need to be done for each sample in the same conditions to verify repetibility of the data.

After interrupted tensile tests, BSE-SEM images were acquired for the polished surface of all specimens. Voids and cracks were segmented using the plugin “Trainable Weka segmentation” of “ImageJ” software, it is important to notice that only voids and cracks

with an area larger than 25 um^2 were considered in the quantitative analysis of the present project, to discard the possible effects of noise. Also, a parameter known in the present research as "total depth of damage" from the surface is defined as the maximum distance at which the minimum area of individual voids is 50 um^2. The features (voids and cracks) shape was analysed by assuming that particles were round, to compute the size (radio um) and the aspect ratio.

It is observed that when the humidity increases from 0 to 90%RH at the same strain rate. The maximum "total depth of damage" from the surface (2757 um) was obtained, this means an increase up to 47% in the "total depth of damage". Furthermore, the total number of voids and cracks increases by 43 and 36 % respectively. Surprisingly, samples tested at the same environment (50%RH) and decreasing strain rate (10^{-5} to 10^{-6} /s) display a similar total number of voids. These findings suggest that the variation in voids nucleation might be only affected by changes in the humidity concentrations. These findings are contrary to that of Maire et al. (2019) [95] who studied the nucleation of voids in the AISI316L steel for hydrogen charged and non-charged specimens. The mechanical properties were reduced by 33%. However, the variation in the total number of voids is minimal; a possible explanation for this inconsistent result might be that the AISI316L steel has few inclusions, which are considered preferential nucleation sites.

As previously explained, the data from the polished surfaces were classified into voids and cracks. Then, for the present analysis, only voids and cracks with an area larger than 25 um^2 were considered to discard possible noise; with this in mind, the total number of voids for the alloys tested in dry air, and high humidity is 103 and 180 voids respectively. The average size of voids for both samples is 2 um. Then, only considering the voids with a radio larger than 2 um; the number of voids for dry air and high humidity tests is 79 and 122, which means an increased up to 35%. Now, only considering the number of voids smaller than 2 um for dry air and high humidity tests is 24 and 58, which is a 58% addition. Two main things are observed; The nucleation of voids is representative for all void sizes when the humidity level increases and it is clear that the increment in the number of voids smaller than 2 um is playing an important role in the weakening of the aluminium alloy. This last finding might be explained because a feature

known in the present project as “string of cracks joined by voids” found only in samples tested at humid air consist of small voids joined by cracks along grain boundaries, which are organised in a way that the feature can reach lengths up to 350 um having a detrimental effect, Furthermore cracks display the same tendency as voids.

When comparing the aspect ratio of the voids and cracks with an area larger than 25 um^2, it was found that when humidity increases from 0 to 90% RH voids and cracks became a 30 and 13 % sharper respectively, and as expected cracks are sharper than voids by a 40%. These findings are consistent with Maire et al. (2019) [95] who compute the aspect ratio of voids in two charged hydrogen steels, with different susceptibility to hydrogen effects. The results were that voids in the most susceptible alloy changed from round into a needle shape in the loading direction. It was believed that this changed in void shaped is responsible for the reduction in ductility observed in the mechanical response. In contrast, the mechanical test in the present research did not display considerable ductile reduction; however, there is a clear addition in the number and elongation of voids along grain boundaries occurring when hydrogen levels increases. Then, this lack of reduction in the plastic and total strain rate might be explained by the interrupted nature of the tests.

There is a tendency for aluminium alloys tested in humid air to develop considerable deformation (cracks, voids, and slips) along grain boundaries (Lynch, 2012) [45]. This is supported by Gupta et al. (2016) [92] who found cracks along grain boundaries in hydrogen charged the AA7075 aluminium alloy which were absent in non-charged specimens. Also, Holroyd et al. (2017) [72] described hydrogen accumulation effects on the nucleation of voids at second phase particle interfaces and the void-coalescence process responsible for the intergranular fracture path. In the present study, deformation and damaged (cracks, voids and slips) in samples tested at the same strain rate, but different humidity levels are characterised by an increase up to 20 times in the number of medium-cracks (separations at grain boundaries) along grain boundaries. When comparing samples at the same environment but different strain rate little differences were found. A possible explanation for this might be that only hydrogen plays an essential role in the susceptibility of grain boundaries, and it is possible that

atomic hydrogen might be concentrating at grain boundaries, second phase particles, crack tips and zones of high hydrostatic stresses.

For all samples, it was observed that most voids nucleated preferentially at precipitates and/or triple junctions between recrystallised and non-recrystallised grains. For this reason, it is surprising that samples tested at vacuum display the majority of voids only when Taylor factor variations are higher than 0.6; however, samples tested in humid air presents the majority of voids for small Taylor number variations that were as low as 0.2. This outcome is contradictory to that of Bieler et al. (2002) [62] who found that voids occurred preferentially between grains with contrasting orientations. These observations may support the hypothesis that atomic hydrogen weakens the atomic bonds (Lynch, 2011) [15] promoting the separation of grain boundaries at lower stresses.

The analysis of the fracture surface shows that in effect, as expected when humidity increases, there is an addition in the brittle fraction area, and also the area reduction decreases. Only in samples tested in humid environments, three fracture type surfaces are displayed, in which “fracture type 1” is a smooth, bright and featureless area located close to the edges of the samples in which some initiation sites are observed, “fracture type 1” propagates through tearing of the samples without the presence of microvoids. At some point, it is transformed into “fracture type 2” which is characterised by a high topographical surface between grains, in which grain boundaries are clearly observed. They are strongly related with clusters of intermetallic particles, to finally transformed into the “fracture type 3” which is a ductile intergranular fracture characterise by voids and dimples, this finding was also reported by Holroyd et al. (2017) [72] When correlating the initiation sites with the polished surface it is observed that this flat features in “fracture type 1” started in cracks along grain boundaries which eventually open up or voids located at grain boundary separations, this may explain the earlier failure of the material as this defects acts as notches that act as stress concentrators decreasing the resistance of materials to failure. (Speidel and Hyatt, 1972) [3]

In summary, without hydrogen under vacuum conditions, the failure is produced by the growth and coalescence of voids at second phase particles and hydrogen micropores. On the other hand, in hydrogen (moist air), we see some additional effects, there is an increase in the number of cracks, separation of grains and voids as humidity levels increases; this might suggest that hydrogen is concentrating preferentially in the mention areas and implicates that the material's failure might occur as follows:

i) First, fracture initiation (void and crack growth) occurs on the material surface at medium cracks (grain boundaries separation); this is characterised by a 90-degree angle to the loading direction, smooth, flat surface that propagates by tearing without the presence of microvoids. (Fracture type 1)

ii) As most damage (crack and void growth) only occurs after UTS, there is enough time for hydrogen to concentrate in zones of high hydrostatic stresses in front of crack tips and then diffused to IMPs clusters and grain boundaries located in the material's interior.

iii) At this stage "fracture type 1" is transformed into "fracture type 2" which is characterised by high topography between grains, displaying flat surfaces with intermetallic particles clusters.

iv) Finally, the areas in which hydrogen could not diffuse (due to lack of time or low hydrogen concentrations) are separated rapidly, forming the dimpled surface that characterised "Fracture type 3".

Practical aspects of the tests method meant that whilst we make these observations, this is not apparent in the mechanical performance recorded because of the interrupted nature; but there is a clear difference based on the observations that are taking place in the polished surface and the inside of the material.

Based on the last observations, I proposed the following sequence for the development of the fracture in humid air environments:

These findings support that hydrogen plays an essential role in the deformation and earlier failure of the specimen, hydrogen embrittlement occurs by a hybrid mechanism

in which hydrogen is transported at higher velocities to the grain boundaries and crack tips through the movement of dislocations (HELP); hydrogen then is able to diffuse ahead of cracks to zones of high hydrostatic stresses, this might be supported because there is more separation in grain boundaries as humidity increases. Next, hydrogen promotes the decohesion (weakening) of the interatomic bonds between grain boundaries, causing a featureless surface, which explains the presence of “fractures type 1” which then propagates to the material interior and changes into the “fracture type 2” as the result of hydrogen diffusing ahead of crack tips concentrating at grain boundaries and cluster of intermetallic particles.

8.1. Conclusions

For the aluminium alloy 7040-T7651 under the testing conditions used it is concluded that:

1. The degree of embrittlement for aluminium alloys tested in humid air environments is strongly dependent on the humidity concentrations and exposure times.
2. The number of voids and cracks increase up to 43 and 36% respectively by the effects of humidity concentration increments for samples tested at the same strain rate.
3. As humidity level increases, voids and cracks become 30 and 13% sharper respectively changing from blunt into an elongated shape.
4. As the strain rate decreases, when comparing samples 2 and 5 tested in lab air; it is observed that variations are scarce in the number and aspect ratio of voids: 2 and 5% respectively.
5. In lab air tensile tests, when comparing the strain rate decreases (10^{-5} to 10^{-6} /s), the total number of cracks varies only 4%, and the aspect ratio remains similar at 8.15.
6. Humidity concentration increments play a more detrimental effect when compared to exposition times; this is based on the bullet points 3 to 7 previously reviewed.
7. A feature called in the present study as “string of cracks joined by voids” is observed only at high humidity levels (90%RH) and lab air (50%RH) conditions.
8. The feature “string of cracks joined by voids”, is formed by cracks and voids of small sizes join together along grain boundaries acquiring detrimental lengths up to 300 um.
9. The feature “string of cracks joined by voids” is not observed in dry air conditions independently of the strain rate velocity of experiments.
10. In samples tested at the same strain rate and different humidity levels, the number of medium-cracks (separations between grain boundaries) increases up to 20 times when humidity raises from o to 90%.

11. In samples tested at the same humidity compositions but different strain rate, only a slight change in the number of medium-cracks (separation between grain boundaries) is observed.
12. The increased in the number of medium-cracks (separation between grain boundaries) up to 20 times when humidity level increases from 0 to 90%RH is attributed to HELP mechanism, as more deformation was observed closed to voids and grain boundaries, which indicates that hydrogen moves faster through dislocations into grain boundaries.
13. It is strongly believed that HEDE mechanism allows the nucleation of voids and the separation of grain boundaries, even for Taylor factor variations as small as 0.2, because decohesion weakens the interatomic bonds, explaining why the failure occurred in conditions at which materials tested in normal conditions (dry air) do not fracture.
14. Increases in humidity concentrations and exposition times cause a reduction in the final cross-sectional area up to 14%.
15. Increases in humidity concentrations and exposition times cause an increment in brittle fraction areas up to 56%.
16. “Fracture Type 1” only occurs in humid air environments and displays intergranular, flat, featureless facets in 90 a degree angle to the loading direction, caused by the decohesion of interatomic bonds as hydrogen concentrates in grain boundaries.
17. HELP is the mechanism responsible for the rapid accumulation of hydrogen at grain boundaries and crack tips through the movement of dislocations.
18. The material’s failure occurs in humid air environments as the result of a Hybrid Hydrogen Embrittlement mechanism, in which HELP mechanism plays the leading role, as it should transport atomic hydrogen to grain boundaries to weaken the interatomic bonds and then propagate the fracture to the material’s interior.

These findings are correct for the testing conditions on the present research and it should be acknowledged that different results would be obtain if conditions changed, for example, different tempers and\or under mechanical conditions where under longer environmental exposure times at stresses below the alloy yield stress.

8.3. Future Work

1. It is recommended that as the stress-strain curves were not completely understood, the in-situ tests could be repeated; first without relaxations and then controlling that all samples follow the same relaxation periods to understand the effects of such relaxations in the earlier failure of the material.
2. A similar set of tests might be repeated to another set of aluminium alloy 7xxx series, preferentially using a material known for having better resistance against Hydrogen Embrittlement than Aluminium alloys 7040-T7651, to correlate which changes in the microstructure allow a better resistance to atomic hydrogen effects.
3. The same set of test can be performed in samples with pre-existing notches to have a better understanding of the crack propagation mechanisms when a preferential site for hydrogen diffusion exists.
4. Sequential polishing steps might be fundamental to understand how cracks develop under the surface and the differences in the propagation between samples tested at vacuum and humid air.
5. More tests need to be done for each environment in the present project to determine/verify if the differences in the tensile tests results can be simply attributed to experimental scatter.
6. More tests need to be done to create a base-line tensile test data without the loading interruptions introduced by image acquisition, to complement the analysis of the present data.
7. In the present research testing generally involved 'one-off' tests. It is then, critical to replicate the tests to establish reproducibility.
8. Equivalent testing can be performed for the alloy 7040 when it is under and\or peak aged temper for comparison with the data in the present research.
9. Testing can be done for samples that are pre- exposed to distilled water or humid air for extended periods ahead of straining to enable the initiation of intergranular Type-1 EIC.
10. Further work is needed to determine if the use of EDM during tensile test specimen had any influence on Hydrogen Embrittlement crack initiation.

References

(1) Wanhill, R. J.H., R. T. Byrnes, and C. L. Smith. (2011). Stress corrosion cracking (SCC) in aerospace vehicles. In *Stress corrosion cracking: Theory and practice*, by R. J.H. Wanhill, R. T. Byrnes and C. L. Smith.

(2) Sprowls, D. O., & Brown, R. H. (1969). Fundamental aspects of stress corrosion cracking. NACE, Houston, 466.

(3) Speidel, M. O., & Hyatt, M. V. (1972). Stress-corrosion cracking of high-strength aluminum alloys. In Advances in corrosion science and technology (pp. 115-335). Springer, Boston, MA.

(4) Gruhl, W. (1984). Stress corrosion cracking of high strength aluminum alloys. Zeitschrift fuer Metallkunde, 75, 819-826.

(5) Montrain L and Swann P. R. (1974). Proceeding of the International Conference on Hydrogen in Metals. Seven Springs, 1973 edited by I. M. Bernstein and A. W. Thompson (A.S.M., Metals Park Ohio). p. 575.

(6) Gangloff, Richard P. (2003). Hydrogen Assisted Cracking of High Strength Alloys. In Comprehensive Structural Integrity, edited by I Milne, R O Ritchie, and B Karihaloo, 6 : 31-101. New York, NY: Elsevier Science.

(7) Scamans, G. M. (1978). Hydrogen bubbles in embrittled Al-Zn-Mg alloys. Journal of Materials Science, 13(1), 27-36.

(8) Knight S.P. : Ph.D. Thesis, Monash University, Melbourne, 2008

(9) Knight, S. P., Birbilis, N., Muddle, B. C., Trueman, A. R., & Lynch, S. P. (2010). Correlations between intergranular stress corrosion cracking, grain-boundary microchemistry, and grain-boundary electrochemistry for Al–Zn–Mg–Cu alloys. Corrosion Science, 52(12), 4073-4080.

(10) Rao, A. U., Vasu, V., Govindaraju, M., & Srinadh, K. S. (2016). Stress corrosion cracking behaviour of 7xxx aluminum alloys: A literature review. Transactions of Nonferrous Metals Society of China, 26(6), 1447-1471.

(11) Holroyd, N. J. H. (1990). Environment-induced cracking of high-strength aluminum alloys. Environment-induced cracking of metals, NACE, Houston, 311-345.

(12) Albrecht, J., Bernstein, I. M., & Thompson, A. W. (1982). Evidence for dislocation transport of hydrogen in aluminum. Metallurgical Transactions A, 13(5), 811-820.

(13) Nguyen , D., Thompson, A. W., & Bernstein, I. M. (1987). Microstructural effects on hydrogen embrittlement in a high purity 7075 aluminum alloys. Acta Metallurgica, 35(10), 2417-2425.

(14) Speidel, M. O. (1971). Current understanding of stress corrosion crack growth in aluminum alloys. Paper from" The Theory of Stress Corrosion Cracking in Alloys". 1971. NATO, Brussels, Belgium. 289-344.

(15) Lynch, S. (2011). Hydrogen embrittlement (HE) phenomena and mechanisms. In S. Lynch, Stress corrosion cracking: Theory and practice (pp. 90-130). Elsevier Ltd

(16) Beachem, C. D. (1972). A new model for hydrogen-assisted cracking (hydrogen “embrittlement”). Metallurgical and Materials Transactions B, 3(2), 441-455.

(17) Birnbaum, H. K., Robertson, I. M., Sofronis, P., & Teter, D. (1996). Mechanisms of hydrogen related fracture--a review. In Second International Conference on Corrosion-Deformation Interactions. CDI'96 (pp. 172-195)

(18) Polmear, I., StJohn, D., Nie, J. F., & Qian, M. (2017). Light alloys: metallurgy of the light metals. Butterworth-Heinemann.

(19) Speidel, M. O. (1975). Stress corrosion cracking of aluminum alloys. Metallurgical Transactions A, 6(4), 631.

(20) Staley, J. T., & Liu, J. (1997). Aluminum alloys for aerostructures. Advanced materials & processes, 152(4), 17-20.
(21) Starke Jr, E. A., & Staley, J. T. (2011). Application of modern aluminium alloys to aircraft. In Fundamentals of aluminium metallurgy (pp. 747-783). Woodhead Publishing.
(22) Vargel, C. (2004). Corrosion of aluminium. Elsevier.
(23) Li, J. F., Peng, Z. W., Li, C. X., Jia, Z. Q., Chen, W. J., & Zheng, Z. Q. (2008). Mechanical properties, corrosion behaviors and microstructures of 7075 aluminium alloy with various aging treatments. Transactions of Nonferrous Metals Society of China, 18(4), 755-762.
(24) ZANG, J. X., ZHANG, K., & DAI, S. L. (2012). Precipitation behavior and properties of a new high strength Al-Zn-Mg-Cu alloy. Transactions of Nonferrous Metals Society of China, 22(11), 2638-2644.
(25) Li, X. Z., Hansen, V., Gjønnes, J., & Wallenberg, L. R. (1999). HREM study and structure modeling of the η′ phase, the hardening precipitates in commercial Al–Zn–Mg alloys. Acta materialia, 47(9), 2651-2659.
(26) Rometsch, P. A., Zhang, Y., & Knight, S. (2014). Heat treatment of 7xxx series aluminium alloys—Some recent developments. Transactions of Nonferrous Metals Society of China, 24(7), 2003-2017.
(27) Kaufman, J. G. (2000). Introduction to aluminum alloys and tempers. ASM International.
(28) Huang, K., Marthinsen, K., Zhao, Q., & Logé, R. E. (2018). The double-edge effect of second-phase particles on the recrystallization behaviour and associated mechanical properties of metallic materials. Progress in Materials Science, 92, 284-359.
(29) Liu, G. Q., Zhang, G. J., Ding, X. D., Sun, J., & Chen, K. H. (2003). Dependence of fracture toughness on multiscale second phase particles in high strength Al alloys. Materials science and technology, 19(7), 887-896.
(30) Conserva, M., Di Russo, E., & Caloni, O. (1971). Comparison of the influence of chromium and zirconium on the quench sensitivity of Al-Zn-Mg-Cu alloys. Metallurgical Transactions, 2(4), 1227-1232.
(31) Thompson, D. S., Subramanya, B. S., & Levy, S. A. (1971). Quench rate effects in al-zn-mg-cu alloys. Metallurgical Transactions, 2(4), 1149-1160.
(32) Guinier, A. (1938). Structure of age-hardened aluminium-copper alloys. Nature, 142(3595), 569-570.
(33) Sato, T. (2006). Nanostructure Control for High-Strength and High-Ductility Aluminium Alloys. Nanomaterials: Elsevier, 315-34
(34) Sha, G., & Cerezo, A. (2004). Early-stage precipitation in Al–Zn–Mg–Cu alloy (7050). Acta Materialia, 52(15), 4503-4516.
(35) Vasudevan, A. K., & Doherty, R. D. (1987). Grain boundary ductile fracture in precipitation hardened aluminum alloys. Acta metallurgica, 35(6), 1193-1219.
(36) Crooks, R. E., Kenik, E. A., & Starke Jr, E. A. (1983). HVEM in situ deformation of Al-Li-X alloys. Scripta metallurgica, 17(5), 643-648.
(37) Doig, P., Flewitt, P. E. J., & Edington, J. W. (1977). The stress corrosion susceptibility of 7075 Al-Zn-Mg-Cu alloys tempered from T6 to an overaged T7X. Corrosion, 33(6), 217-221.
(38) Ramgopal, T., Gouma, P. I., & Frankel, G. S. (2002). Role of grain-boundary precipitates and solute-depleted zone on the intergranular corrosion of aluminum alloy 7150. Corrosion, 58(8), 687-697.

(39) Goswami, R., Lynch, S., Holroyd, N. H., Knight, S. P., & Holtz, R. L. (2013). Evolution of grain boundary precipitates in Al 7075 upon aging and correlation with stress corrosion cracking behavior. Metallurgical and Materials Transactions A, 44(3), 1268-1278.
(40) Lynch, S. P. (1988). Environmentally assisted cracking: overview of evidence for an adsorption-induced localised-slip process. Acta Metallurgica, 36(10), 2639-2661.
(41) Lynch, S. P. (1986). A fractographic study of hydrogen-assisted cracking and liquid-metal embrittlement in nickel. Journal of Materials science, 21(2), 692-704.
(42) Lynch, S. P. (1982). Mechanisms of environmentally assisted cracking in Al-Zn-Mg single crystals. Corrosion Science, 22(10), 925-937.
(43) Johnson, H. H. (1973). Hydrogen gas embrittlement (No. COO-3166-8). Cornell Univ., Ithaca, NY (USA).
(44) Scamans, G. M., & GM, S. (1982). Stress Corrosion Cracking of Aluminium Alloys by Hydrogen Embrittlement.
(45) Lynch, S. P. (2012). Metallographic and fractographic techniques for characterising and understanding hydrogen-assisted cracking of metals. In Gaseous hydrogen embrittlement of materials in energy technologies (pp. 274-346). Woodhead Publishing.
(46) Robertson, I. M., Sofronis, P., Nagao, A., Martin, M. L., Wang, S., Gross, D. W., & Nygren, K. E. (2015). Hydrogen embrittlement understood. Metallurgical and Materials Transactions A, 46(6), 2323-2341.
(47) Albrecht, J., Thompson, A. W., & Bernstein, I. M. (1979). The role of microstructure in hydrogen-assisted fracture of 7075 aluminum. Metallurgical Transactions A, 10(11), 1759-1766
(48) Thompson, A. W., & Bernstein, I. M. (1980). The role of metallurgical variables in hydrogen-assisted environmental fracture. In Advances in corrosion science and technology (pp. 53-175). Springer, Boston, MA.
(49) Ciaraldi, S. W., Nelson, R. A., Yske, R. A., & Pugh, E. N. (1981). Studies of Hydrogen Embrittlement and Stress-Corrosion Cracking in Aluminum-Zinc-Magnesium Alloy. Proceedings of Conf. Hydrogen Effects in Metals (pp. 437-447). Warrendale, USA
(50) Troiano, A. R. (1960). The role of hydrogen and other interstitials in the mechanical behavior of metals. trans. ASM, 52, 54-80.
(51) Scully, J. R., Young Jr, G. A., & Smith, S. W. (2012). Hydrogen embrittlement of aluminum and aluminum-based alloys. In Gaseous hydrogen embrittlement of materials in energy technologies (pp. 707-768). Woodhead Publishing.
(52) Vehoff, H., & Rothe, W. (1986). Gaseous hydrogen embrittlement in FeSi-and Ni-single crystals. In Perspectives in Hydrogen in Metals (pp. 647-659). Pergamon.
(53) Roylance, D. (2001). Introduction to fracture mechanics.
(54) Scattergood, R. O., & Bacon, D. J. (1975). The Orowan mechanism in anisotropic crystals. Philosophical Magazine, 31(1), 179-198.
(55) Smallman, R. E. (2016). Modern physical metallurgy. Elsevier.
(56) Broek, D. (1974). Some contributions of electron fractography to the theory of fracture. International Metallurgical Reviews, 19(1), 135-182.
(57) Jackson, A. G. (2012). Handbook of Crystallography: For electron microscopists and others. Springer Science & Business Media.
(58) Hughes, D. A., & Hansen, N. (1997). High angle boundaries formed by grain subdivision mechanisms. Acta materialia, 45(9), 3871-3886.

(59) Orozco-Caballero, A., Lunt, D., Robson, J. D., & da Fonseca, J. Q. (2017). How magnesium accommodates local deformation incompatibility: a high-resolution digital image correlation study. Acta Materialia, 133, 367-379.
(60) Lebensohn, R. A., & Tomé, C. N. (1993). A self-consistent anisotropic approach for the simulation of plastic deformation and texture development of polycrystals: application to zirconium alloys. Acta metallurgica et materialia, 41(9), 2611-2624.
(61) Kocks, U. F., Tomé, C. N., & Wenk, H. R. (1998). Texture and anisotropy: preferred orientations in polycrystals and their effect on materials properties. Cambridge university press.
(62) Bieler, T. R., & Semiatin, S. L. (2002). The origins of heterogeneous deformation during primary hot working of Ti–6Al–4V. International Journal of Plasticity, 18(9), 1165-1189.
(63) Schmid, E., & Boas, W. (1950). Plasticity of crystals.
(64) Hosford, W. F. (2010). Mechanical behavior of materials. Cambridge University press.
(65) UNSW. (2020, 02 20). Online Tutorials. Retrieved from http://www.materials.unsw.edu.au/tutorials/online-tutorials/fatigue-failure
(66) Pineau, A., Benzerga, A. A., & Pardoen, T. (2016). Failure of metals I: Brittle and ductile fracture. Acta Materialia, 107, 424-483.
(67) Liebowitz, H. (Ed.). (2018). Fracture of Metals: An Advanced Treatise. Elsevier.
(68) Brooks, C. R., & McGill, B. L. (1994). The application of scanning electron microscopy to fractography. Materials characterization, 33(3), 195-243.
(69) Vehoff, H., & Rothe, W. (1986). Gaseous hydrogen embrittlement in FeSi-and Ni-single crystals. In Perspectives in Hydrogen in Metals (pp. 647-659). Pergamon.
(70) Kuramoto, S., Itoh, G., & Kanno, M. (1996). Intergranular fracture in some precipitation-hardened aluminum alloys at low temperatures. Metallurgical and Materials Transactions A, 27(10), 3081-3088.
(71) Bieler, T. R., Eisenlohr, P., Zhang, C., Phukan, H. J., & Crimp, M. A. (2014). Grain boundaries and interfaces in slip transfer. Current Opinion in Solid State and Materials Science, 18(4), 212-226.
(72) Holroyd, N. J. H., Burnett, T. L., Seifi, M., & Lewandowski, J. J. (2017). Improved understanding of environment-induced cracking (EIC) of sensitized 5XXX series aluminium alloys. Materials Science and Engineering: A, 682, 613-621.
(73) Bhuiyan, M. S., Tada, Y., Toda, H., Hang, S., Uesugi, K., Takeuchi, A., ... & Watanabe, Y. (2016). Influences of hydrogen on deformation and fracture behaviors of high Zn 7XXX aluminum alloys. International Journal of Fracture, 200(1-2), 13-29.
(74) De Francisco, U., Larrosa, N. O., & Peel, M. J. (2020). Hydrogen environmentally assisted cracking during static loading of AA7075 and AA7449. Materials Science and Engineering: A, 772, 138662.
(75) Leiva-García, R., García-Antón, J., & Muñoz-Portero, M. J. (2011). Application of confocal laser scanning microscopy to the in-situ and ex-situ study of corrosion processes. de Laser Scanning, Theory and Applications. InTech, Wang CC, 431-448.
(76) Fellers, T. J., & Davidson, M. W. (2020, 03 8). Confocal Microscopy. Retrieved from OLYMPUS: https://www.olympus-lifescience.com/en/microscope-resource/primer/techniques/confocal/confocalintro/
(77) Egerton, R. F. (2005). Physical principles of electron microscopy (Vol. 56). New York: Springer.

(78) Microscopy Australia, “My scope training.” [Online]. Available: https://myscope.training/index.html#/SEMlevel_3_1.
(79) J. I. Goldstein, D. E. Newbury, J. R. Michael, N. W. M. Ritchie, J. H. J. Scott, and D. C. Joy, “SEM Microscopy and X-Ray Microanalysis,” pp. VII–XIV, 2018.
(80) Schwartz, A. J., Kumar, M., Adams, B. L., & Field, D. P. (Eds.). (2009). Electron backscatter diffraction in materials science (Vol. 2, p. 403). New York: Springer.
(81) Engler, O., & Randle, V. (2009). Introduction to texture analysis: macrotexture, microtexture, and orientation mapping. CRC press.
(82) Oxford Instruments. (2019, 07 29). *EBSD Explained*. Retrieved from https://nano.oxinst.com/products/ebsd/.
(83) Alloys, W. A. (2015). International Alloy Designations and Chemical Composition Limits for Wrought Aluminum and.
(84) Dumont, D., Deschamps, A., Brechet, Y., Sigli, C., & Ehrström, J. C. (2004). Characterisation of precipitation microstructures in aluminium alloys 7040 and 7050 and their relationship to mechanical behaviour. Materials Science and Technology, 20(5), 567-576.
(85) Rajurkar, K. P., Sundaram, M. M., & Malshe, A. P. (2013). Review of electrochemical and electrodischarge machining. Procedia Cirp, 6, 13-26.
(86) HENRY ROYCE INSTITUTE. (2020, 02, 17). TESCAN AND NEWTEC INSITU TESTING (TANIST). Retrieved from https://www.royce.ac.uk/equipment-and-facilities/tescan-and-newtec-in-situ-testing-tanist/.
(87) Evans, J. T., & Parkins, R. N. (1976). Creep induced by load cycling in a C-Mn steel. Acta Metallurgica, 24(6), 511-515.
(88) Choudhry, M. A., & Ashraf, M. (2007). Effect of heat treatment and stress relaxation in 7075 aluminum alloy. *Journal of alloys and compounds*, *437*(1-2), 113-116.
(89) Lee, D., & Hart, E. W. (1971). Stress relaxation and mechanical behavior of metals. Metallurgical Transactions, 2(4), 1245-1248
(90) Preibisch, S., Saalfeld, S., & Tomancak, P. (2009). Globally optimal stitching of tiled 3D microscopic image acquisitions. Bioinformatics, 25(11), 1463-1465.
(91) Cottrell, A. H. (1958). Theory of brittle fracture in steel and similar metals. Trans. Met. Soc. AIME, 212.
(92) Gupta, C., Toda, H., Fujioka, T., Kobayashi, M., Hoshino, H., Uesugi, K., ... & Suzuki, Y. (2016). Quantitative tomography of hydrogen precharged and uncharged Al-Zn-Mg-Cu alloy after tensile fracture. Materials Science and Engineering: A, 670, 300-313.
(93) Toda, H., Oogo, H., Horikawa, K., Uesugi, K., Takeuchi, A., Suzuki, Y., ... & Kobayashi, M. (2014). The true origin of ductile fracture in aluminum alloys. Metallurgical and Materials Transactions A, 45(2), 765-776.
(94) Toda, H., Oogo, H., Uesugi, K., & Kobayashi, M. (2009). Roles of pre-existing hydrogen micropores on ductile fracture. Materials transactions, 50(9), 2285-2290.
(95) Maire, E., Grabon, S., Adrien, J., Lorenzino, P., Asanuma, Y., Takakuwa, O., & Matsunaga, H. (2019). Role of Hydrogen-Charging on Nucleation and Growth of Ductile Damage in Austenitic Stainless Steels. Materials, 12(9), 1426.

Appendix

Appendix Chapter 6

Post-Mortem Analysis: SEM Images Humid Air Environments

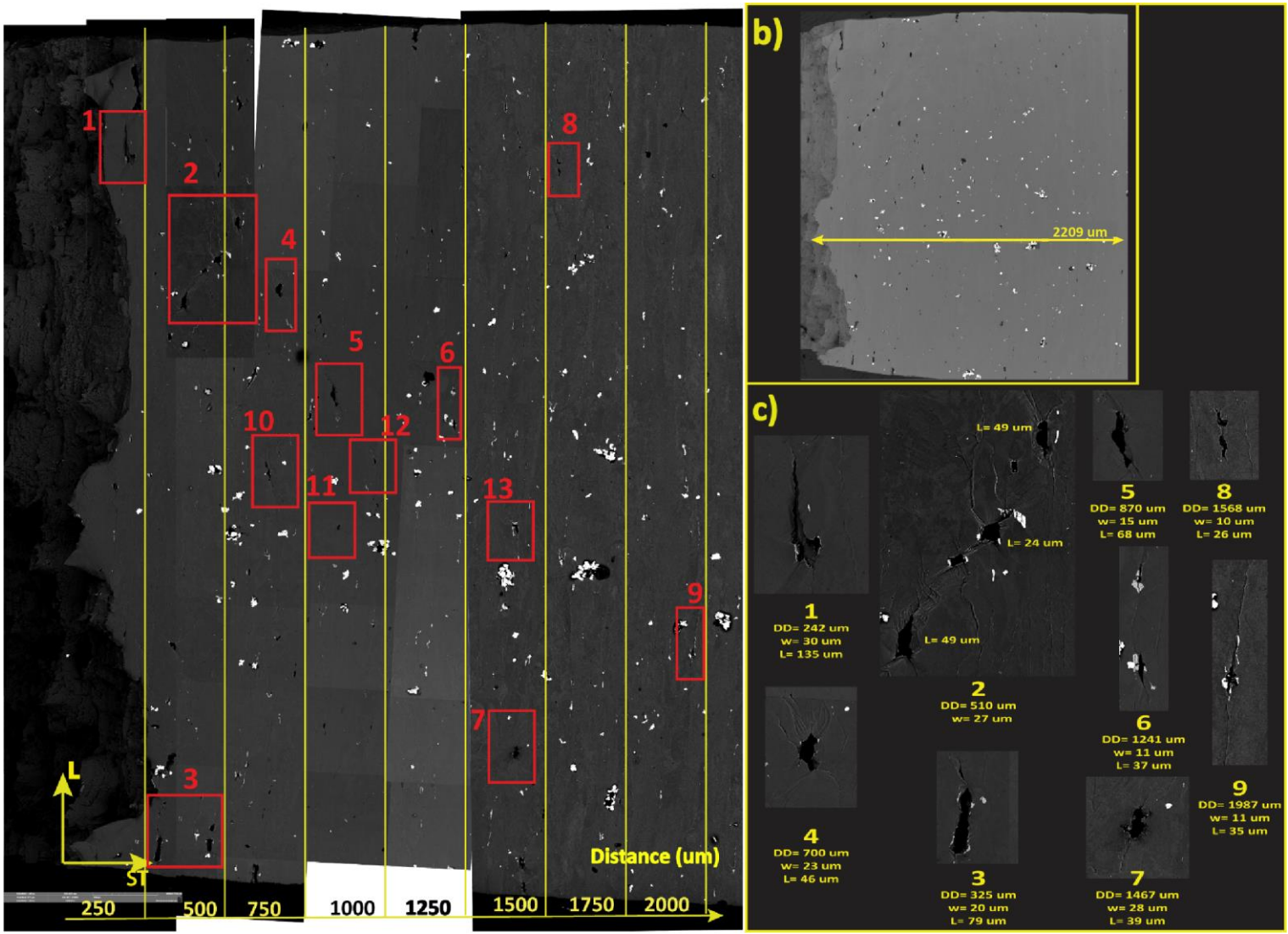

Figure A6-1. BSE-SEM images of AA7040-T7651 sample 2 tested at 50%RH and 10^{-5} $/s$ strain rate. It can be observed: a) an overview of the polished surface at different distances from total DD, b) an overview of the surface showing a total depth of damage of 2209 um, and c) characteristic damaged features at different depths displaying DD, width and length characteristics.

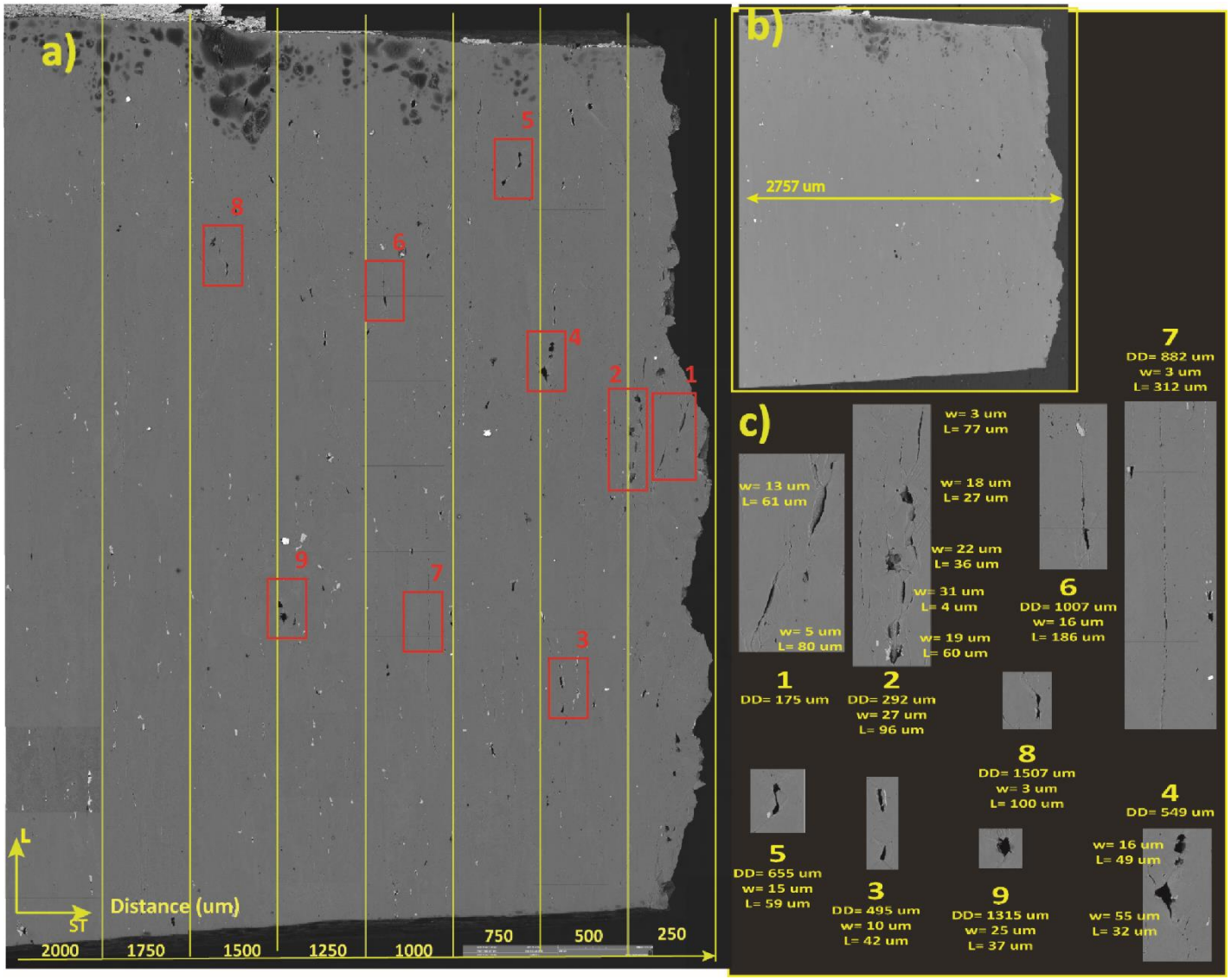

Figure A6-2. BSE-SEM images of AA7040-T7651 sample 3 tested at 90%RH and 10^{-5} $/s$ strain rate. It can be observed: a) an overview of the polished surface at different distances from total DD, b) an overview of the surface showing a total depth of damage of 2757 um, and c) characteristic damaged features at different depths displaying DD, width and length characteristics.

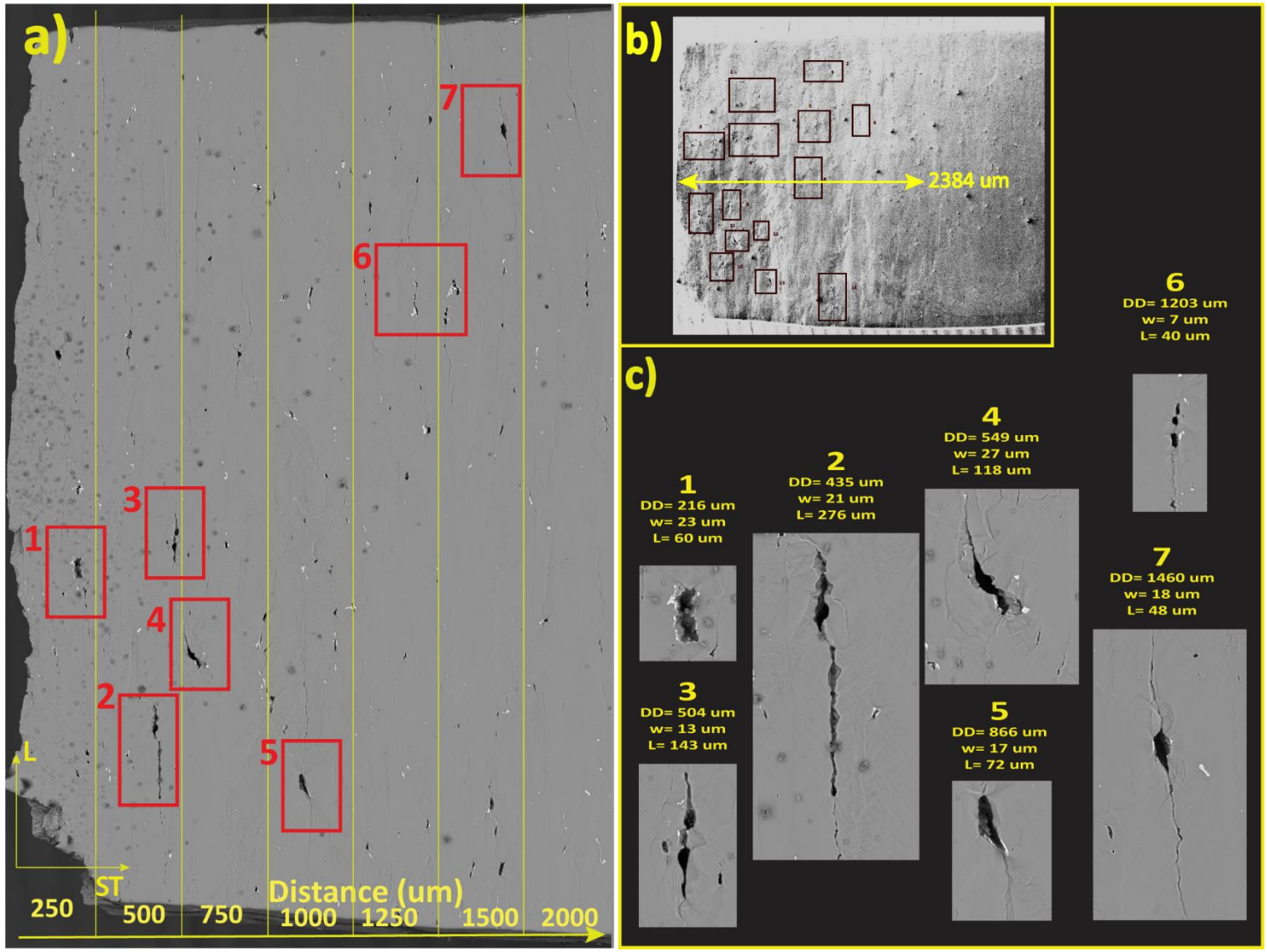

Figure A6-3. BSE-SEM images of AA7040-T7651 sample 5 tested at 90%RH and $10^{-6}\ /s$ strain rate. It can be observed: a) an overview of the polished surface at different distances from total DD, b) an overview of the surface showing a total depth of damage of 2384 um, and c) characteristic damaged features at different depths displaying DD, width and length characteristics.

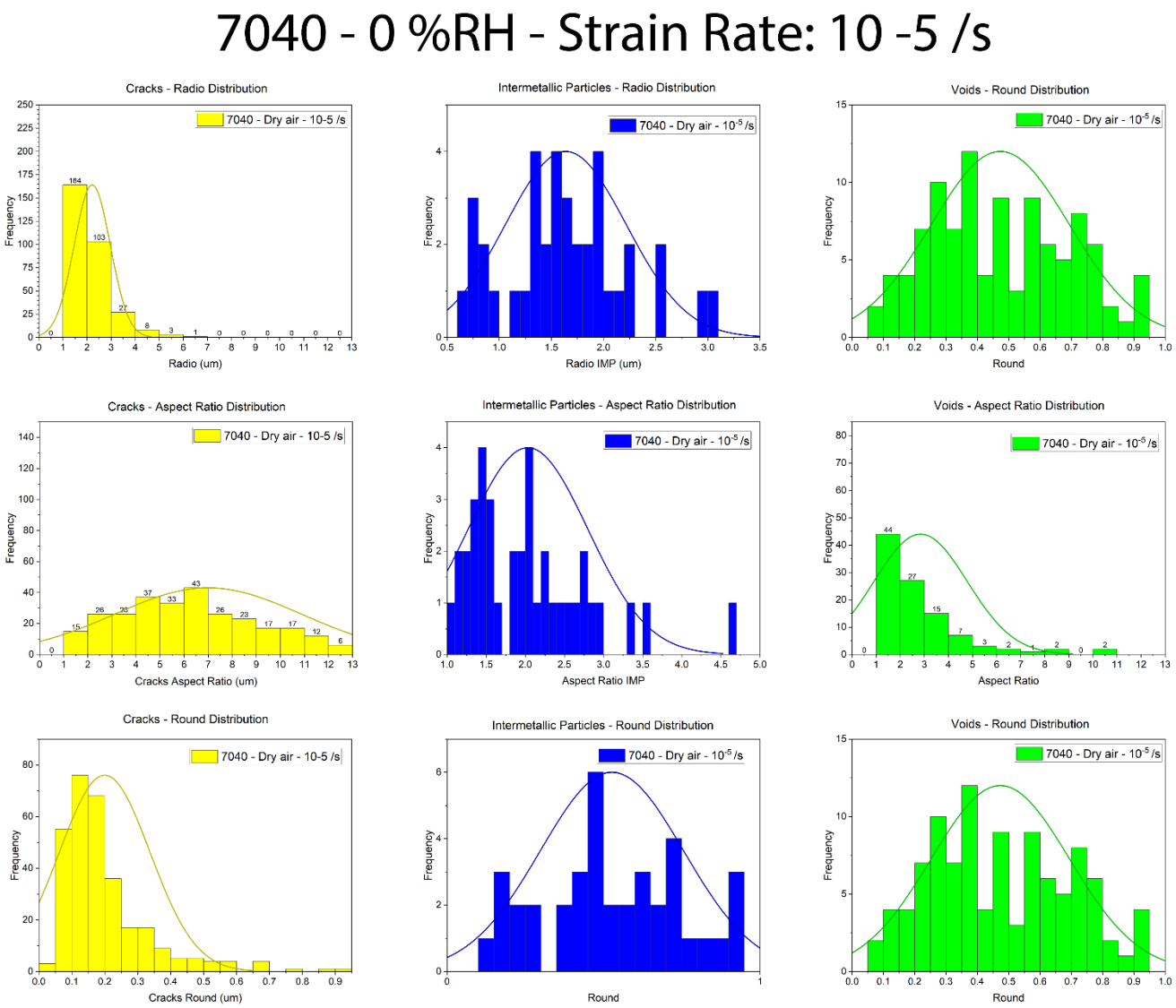

Figure A6-4. Statistical Analysis of sample 1 for cracks, voids and IMPs, the information was obtained with "ImageJ" software, for each feature Aspect Ratio, Radio and Size are studied.

Table A6-1. Microstructural features (voids, IMPs and cracks) characteristics every 250 um, in the polished surface of AA7040-T7651 for sample 1, tested at a strain rate of 10^{-5} /s and 0%RH, the characteristic studied are roundness, radio and aspect ratio at different depths of damage from the surface.

7040 Dry Air Strain Rate: 10^{-5} /s		25		50		75		100		Total		ST. DEV.
		#	Size	#	Size	#	Size	#	Size	#	Size	
Voids	Round	24	0.5687	21	0.4748	21	0.42	37	0.4417	103	0.48	0.22
	Radio (um)		2.7068		3.9318		3.505		3.2626		3.35	2.22
	AR		2.043		2.8834		3.501		2.9719		2.85	1.94
IMPs	Round	14	0.4959	16	0.5624	11	0.608	18	0.4744	59	0.54	0.17
	Radio (um)		1.189		1.9162		1.953		1.751		1.70	0.55
	AR		2.2697		2.0001		1.744		2.3223		2.08	0.74
Cracks	Round	78	0.2209	51	0.1803	77	0.182	100	0.2076	306	0.20	0.14
	Radio (um)		1.9804		2.2362		2.307		2.3267		2.21	0.75
	AR		6.2637		8.0508		7.511		6.6408		7.12	3.87

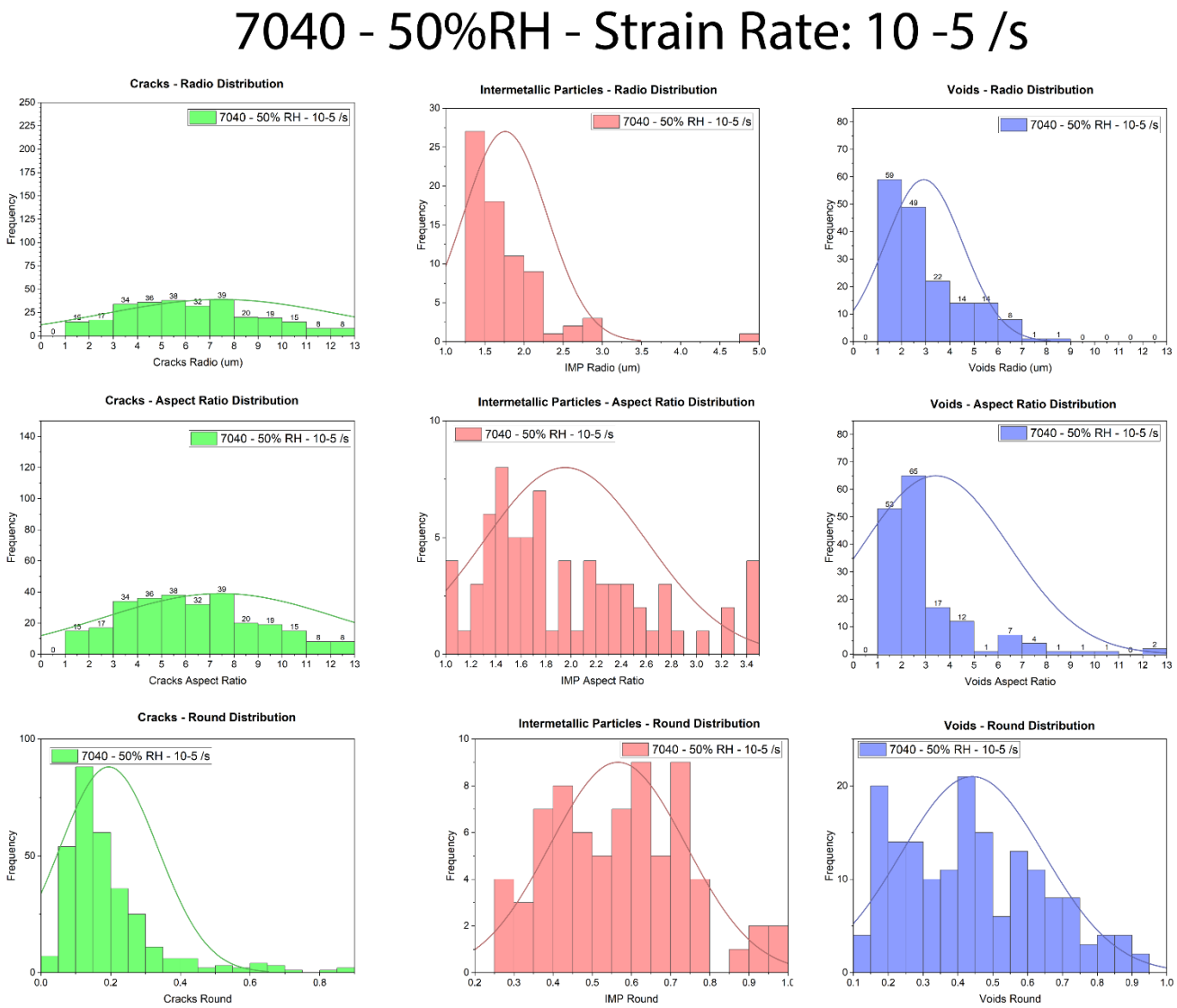

Figure A6-5. Statistical Analysis of sample 2 for cracks, voids and IMPs, the information was obtained with "ImageJ" software, for each feature Aspect Ratio, Radio and Size are studied.

Table A6-2. Microstructural features (voids, IMPs and cracks) characteristics every 250 um, in the polished surface of AA7040-T7651 for sample 2, tested at a strain rate of 10^{-5} /s and 50%RH, the characteristic studied are roundness, radio and aspect ratio at different depths of damage from the surface.

7040 50% RH Strain Rate: 10^{-5} /s		25		50		75		100		125		150		Total		ST. DEV.
		#	Size	#	Size	#	Size	#	Size	#	Size	#	Size	#	Size	
Voids	**Round**	22	0.3689	30	0.5661	35	0.474	25	0.4003	22	0.347	34	0.4366	168	0.43	0.20
	Radio (um)		3.5658		5.7584		3.508		2.3495		2.23		2.7036		3.35	3.05
	AR		3.3393		2.1785		2.478		3.1042		3.903		3.0055		3.00	1.61
IMPs	**Round**	8	0.7055	14	0.6192	13	0.551	7	0.623	15	0.5	15	0.4926	72	0.58	0.17
	Radio (um)		2.2812		1.7079		1.925		1.5489		1.782		1.4652		1.79	0.53
	AR		1.52		1.7303		1.959		1.788		2.192		2.2282		1.90	0.65
Cracks	**Round**	57	0.2228	97	0.1809	125	0.2	3	0.2177	13	0.107	16	0.2071	311	0.19	0.14
	Radio (um)		2.1726		2.6039		2.195		2.0915		2.583		1.99		2.27	0.81
	AR		5.7512		8.1489		7.068		6.7543		14.63		6.7753		8.19	4.86

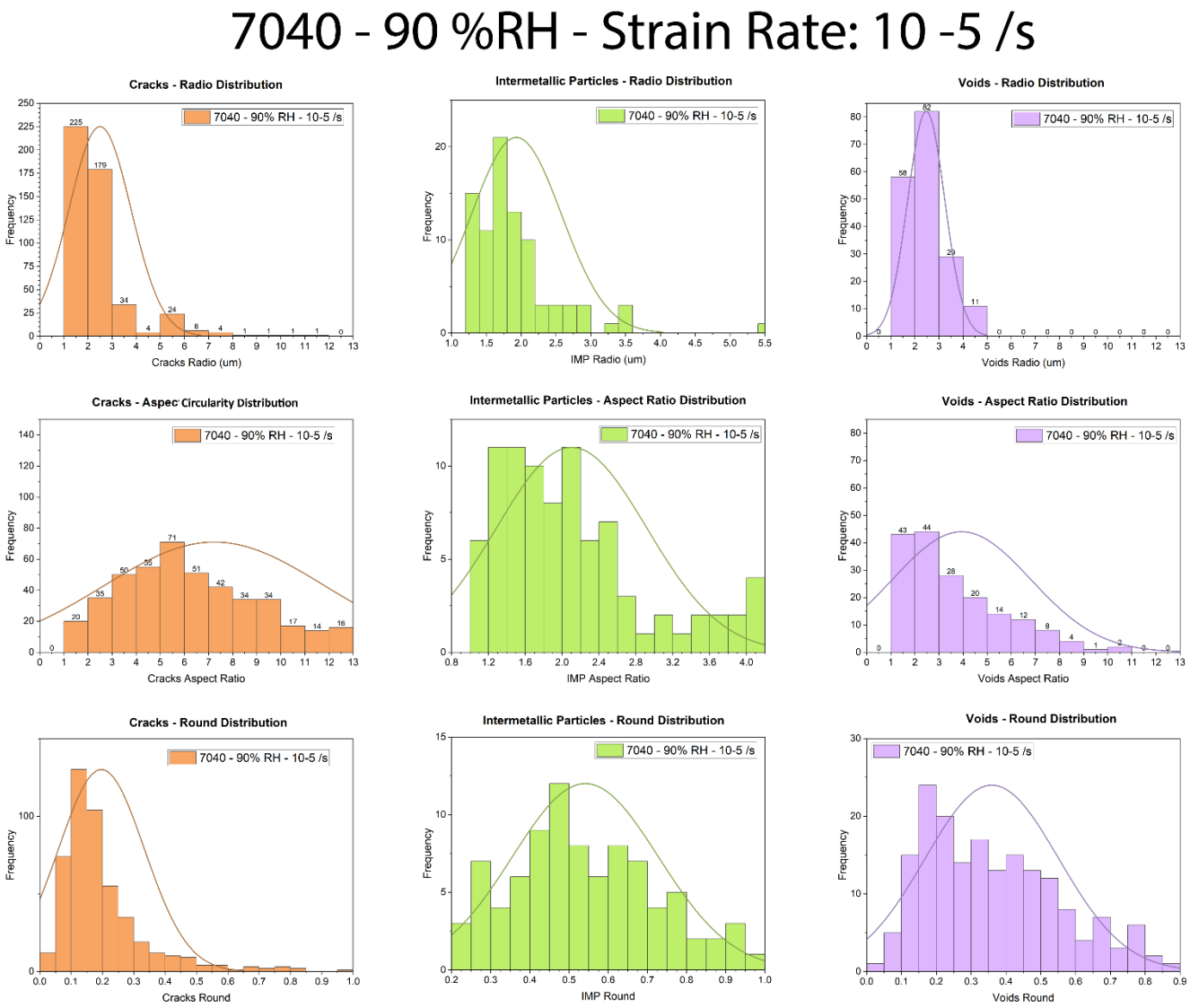

Figure A6-6. Statistical Analysis of sample 3 for cracks, voids and IMPs, the information was obtained with "ImageJ" software, for each feature Aspect Ratio, Radio and Size are studied.

Table A6-3. Microstructural features (voids, IMPs and cracks) characteristics every 250 um, in the polished surface of AA7040-T7651 for sample 3, tested at a strain rate of 10^{-5} /s and 90%RH, the characteristic studied are roundness, radio and aspect ratio at different depths of damage from the surface.

7040 90% RH Strain Rate: 10^{-5} /s		25		50		75		100		125		150		Total		ST. DEV.
		#	Size	#	Size	#	Size	#	Size	#	Size	#	Size	#	Size	
Voids	**Round**	52	0.3346	40	0.3411	28	0.396	19	0.3141	26	0.359	15	0.3211	180	0.344	0.19
	Radio (um)		2.4479		2.4363		2.31		2.4682		2.549		2.4431		2.442	0.77
	AR		4.4958		4.4388		3.437		4.1164		3.362		4.6675		4.086	2.86
IMPs	**Round**	12	0.4961	10	0.4689	24	0.527	21	0.5706	10	0.574	10	0.5521	87	0.531	0.19
	Radio (um)		1.8425		1.8103		1.894		1.9614		1.843		2.2629		1.936	0.65
	AR		2.3594		2.2968		2.258		1.9093		2.076		1.9697		2.145	0.82
Cracks	**Round**	80	0.2	104	0.2035	101	0.214	89	0.1992	37	0.175	69	0.1672	480	0.193	0.14
	Radio (um)		2.0441		2.2264		2.156		2.2608		6.282		2.212		2.863	1.29
	AR		7.4663		7.0979		6.281		7.5383		8.015		7.8161		7.369	4.56

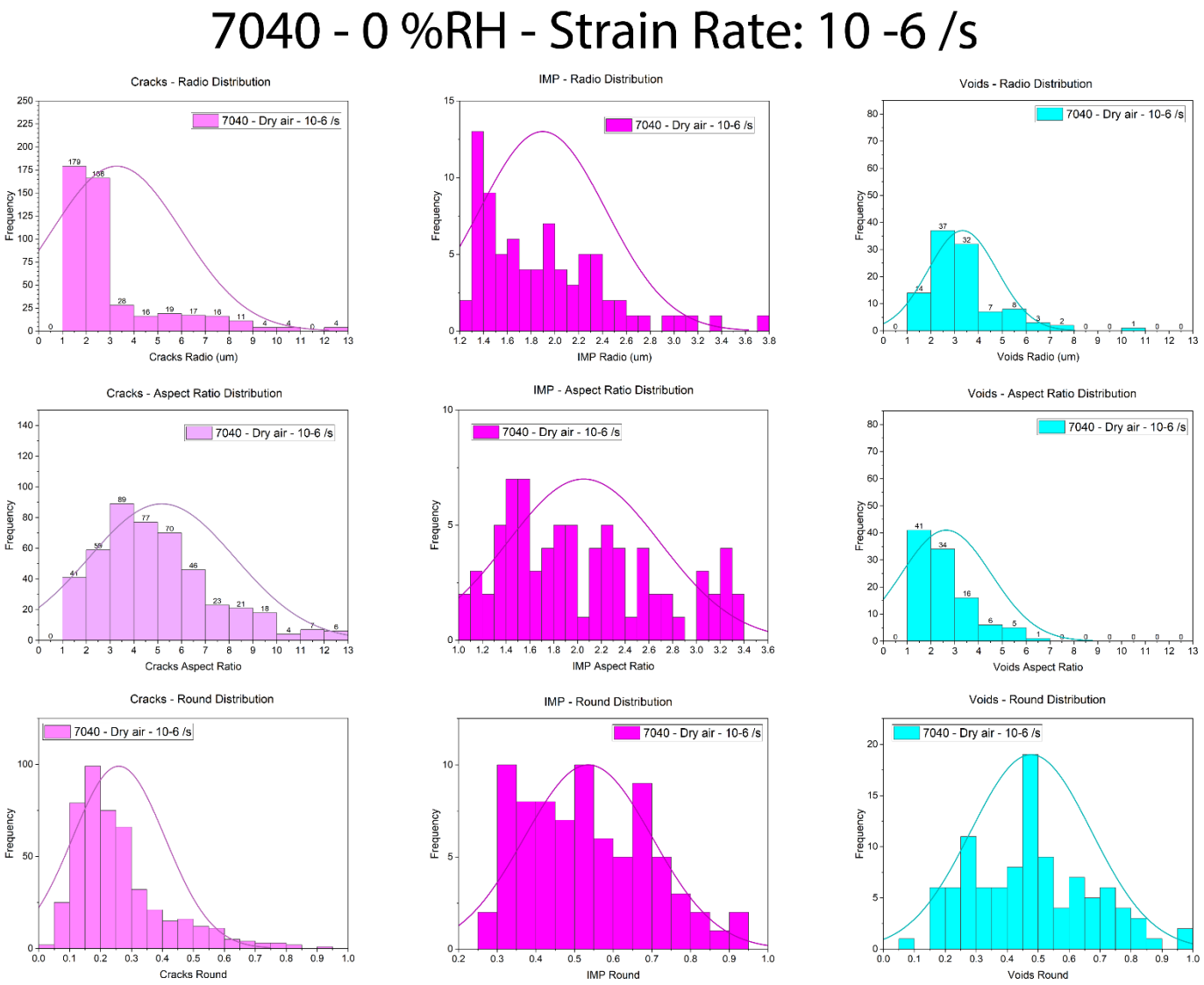

Figure A6-7. Statistical Analysis of sample 4 for cracks, voids and IMPs, the information was obtained with "ImageJ" software, for each feature Aspect Ratio, Radio and Size are studied.

Table A6-4. Microstructural features (voids, IMPs and cracks) characteristics every 250 um, in the polished surface of AA7040-T7651 for sample 4, tested at a strain rate of 10^{-6} /s and 0%RH, the characteristic studied are roundness, radio and aspect ratio at different depths of damage from the surface.

7040 Dry Air Strain Rate: 10^{-6} /s		25		50		75		100		125		150		Total		ST. DEV.
		#	Size	#	Size	#	Size	#	Size	#	Size	#	Size	#	Size	
Voids	**Round**	12	0.3543	32	0.523	20	0.504	15	0.4635	13	0.478	12	0.4495	104	0.46	0.19
	Radio (um)		2.5067		3.7739		3.548		3.0758		3.08		3.1763		3.19	1.45
	AR		3.2723		2.2953		2.98		2.6947		2.56		2.3808		2.70	1.89
IMPs	**Round**	6	0.554	13	0.591	16	0.551	18	0.4998	12	0.523	11	0.5139	76	0.54	0.17
	Radio (um)		1.6667		2.308		1.477		1.5196		2.09		2.4695		1.9	0.64
	AR		1.935		1.8368		2.029		2.2626		2.031		2.0865		2.03	0.53
Cracks	**Round**	37	0.1958	89	0.2993	125	0.23	85	0.2176	77	0.354	58	0.2359	471	0.26	0.15
	Radio (um)		2.2104		2.8549		2.106		2.0722		8.408		2.1297		3.30	2.74
	AR		7.2172		4.5293		5.363		5.6137		3.809		5.6698		5.37	3.06

7040 - 50 %RH - Strain Rate: 10 -6 /s

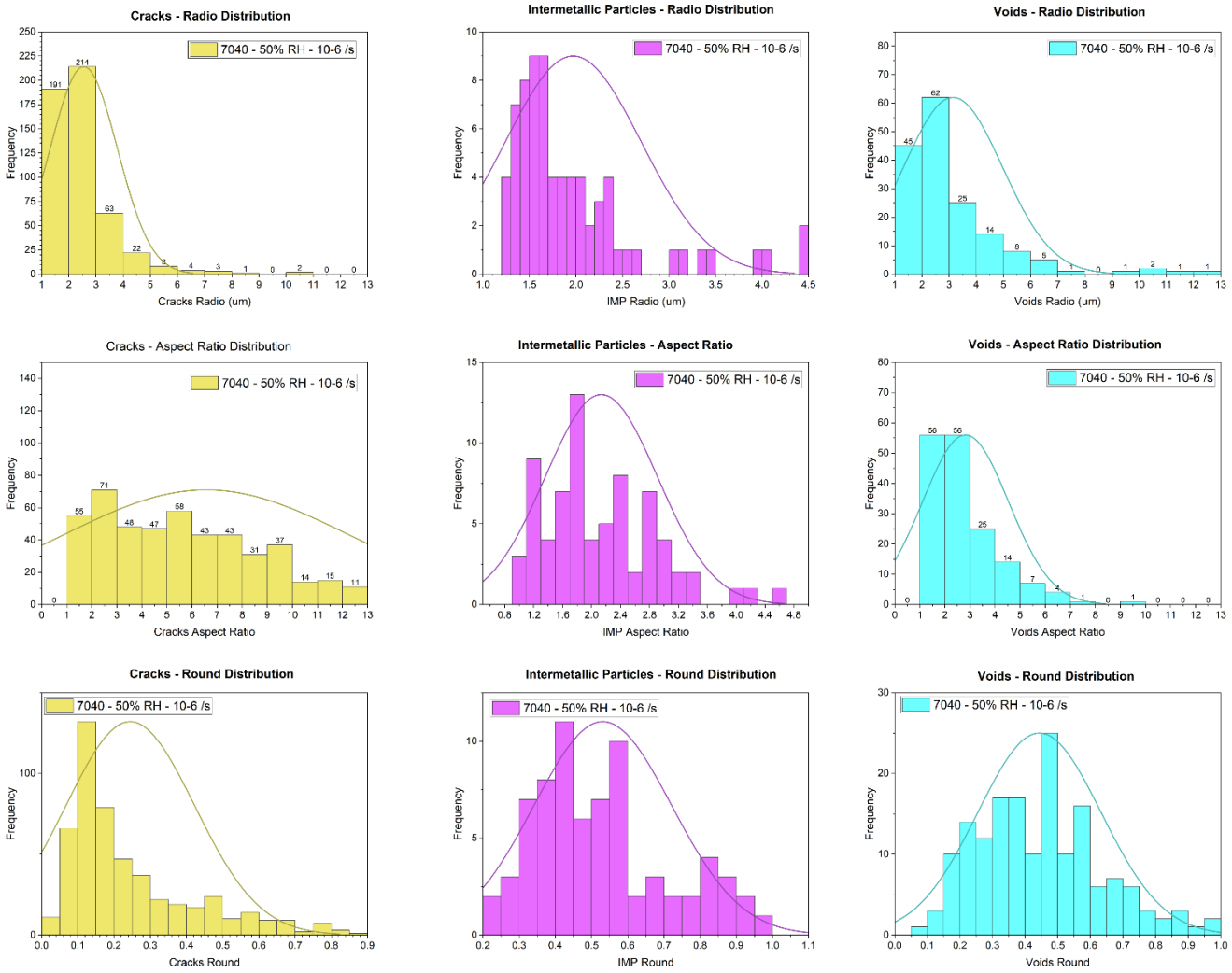

Figure A6-8. Statistical Analysis of sample 5 for cracks, voids and IMPs, the information was obtained with "ImageJ" software, for each feature Aspect Ratio, Radio and Size are studied.

Table A6-5. Microstructural features (voids, IMPs and cracks) characteristics every 250 um, in the polished surface of AA7040-T7651 for sample 5, tested at a strain rate of 10^{-6} /s and 0%RH, the characteristic studied are roundness, radio and aspect ratio at different depths of damage from the surface.

7040 50% RH Strain Rate: 10^{-6} /s		25		50		75		100		125		150		Total		ST. DEV.
		#	Size	#	Size	#	Size	#	Size	#	Size	#	Size	#	Size	
Voids	**Round**	31	0.5376	23	0.3817	8	0.219	41	0.4658	31	0.439	31	0.431	165	0.41	0.19
	Radio (um)		2.7902		3.7855		3.071		3.1214		2.878		3.3419		3.16	1.82
	AR		2.3217		3.4967		5.252		2.471		2.589		2.8905		3.17	1.72
IMPs	**Round**	7	0.5043	17	0.5666	13	0.667	13	0.4181	12	0.516	11	0.4817	73	0.53	0.19
	Radio (um)		1.5826		2.2427		2.238		1.8592		1.904		1.6826		1.92	0.73
	AR		2.2629		1.9429		1.795		2.5705		2.087		2.2946		2.16	0.78
Cracks	**Round**	95	0.3754	141	0.256	87	0.235	50	0.1465	48	0.148	88	0.2038	509	0.23	0.18
	Radio (um)		3.2416		2.4339		2.766		1.9954		2.152		2.3134		2.48	1.24
	AR		3.709		6.4724		12.98		8.314		10.33		7.0027		8.13	5.71